Phase Behaviour of Core-Softened Particles

James Magee

Doctor of Philosophy

University of Edinburgh

2003

Abstract

Over the last three decades, there has been extensive research interest in the behaviour of systems of particles interacting via core-softened potentials. This class of simple interparticle potential was originally developed to model metals such as Cesium, Cerium and Thorium, which undergo "core collapse" - that is, an abrupt diminution of core radius with increasing pressure. This phenomenon is thought to give rise to interesting solid state phase behaviour, including isostructural phase transitions. In recent years, these potentials have also been used to model the behaviour of tetrahedrally-bonded molecular liquids, including H_2O and SiO_2, with particular reference to the liquid state anomalies seen in these systems, widely believed to be linked to the possibility of liquid-liquid phase transitions.

In this thesis, we have made an extended study of a particular core-softened system in two dimensions (originally studied in Sadr-Lahijany *et al*, Physical Review Letters 81, p.4895 [1]). Whereas most studies have only examined single facets of the phase behaviour for a given model, we have systematically studied both liquid and solid state phase behaviour, using a combination of analytic and state of the art simulation methods. Our aim has been to gain a greater understanding of the key features behind the unusual phase behaviour associated with core-softened systems.

After an introduction, we review previous work on the phase behaviour of core-softened systems, in which we see that these apparently "simple" potentials can give rise to a range of unusual and exotic behaviours. We then briefly study the behaviour of a simple one-dimensional core-softened model. This demonstrates liquid state anomalies and a zero temperature transition point, as well as illuminating the dangers of generalising between potentials and across dimensionality.

We then move onto the two dimensional system. We study the solid state using a combination of the harmonic approximation, Lattice Switch Monte Carlo (a recently developed simulation technique which allows Monte Carlo moves between structures), and Gibbs-Duhem integration. We find two triangular lattice phases, separated by a region of stable square lattice phase at intermediate pressure; we also find evidence for an isostructural transition (with possible critical point) between the triangular phases at densities metastable with respect to the square lattice phase. To study the liquid state, we use Lennard-Jones Devonshire cell theory and extensive Monte Carlo simulation. We reevaluate the cell theory model, and find strong evidence that Lennard-Jones and Devonshire's original results were misinterpreted, as were the cell theory results for the system at hand [1]. Our liquid state simulation results confirm the presence of reentrant melting and liquid-state anomalies in the system. We find that, contrary to previous suggestions, these anomalies do not originate from a liquid-liquid transition, but instead from a continuous or near-continuous melting transition, a phenomenon only possible in two dimensions.

Declaration

This thesis has been composed by myself and it has not been submitted in any previous application for a degree. The work reported within was executed by me, unless otherwise stated. Elements of this work appear in references [2] and [3].

April 2003

Dedication

To Ange, with all my love.

To my parents, who answered my questions.

And to the continuing memory of Carl Sagan, for his fantastic television series "Cosmos", without which I'd have tried to be a paleontologist instead.

Acknowledgements

Thanks to Nigel Wilding and Alastair Bruce, for helping me to see it through. Also, to Graeme Ackland, Stewart Reed, and Andrew Jackson for useful discussions. And to Simon Bates for gainful employment.

Further, thanks to the Whole Sick Crew (Haze, Ed, Ben and Emerson) for enduring friendship and what passes for sanity in these parts. To all the old Bristol mob (may the Christmas meals keep coming round), and to Sandy, Jay, Shelley, Nine, Neil etc. for making the far north bearable.

And, finally, I'd like to acknowledge my EPSRC studentship.

Contents

Chapter 1

Introduction

We begin this thesis with a broad brush and necessarily brief discussion of some of the theory and ideas underlying condensed matter physics. We will first give an overview of the theory of statistical mechanics, and how it may be applied to the idea of phase transitions in matter. Then, we will turn to descriptions of those physical states of matter that we seek to represent within this framework. This chapter will introduce many of the concepts that we shall return to in the course of this work.

The rest of this thesis is structured as follows. In chapter 2, we discuss some unusual behaviours observed in experiment for some systems, and review work done on "core-softened" interparticle potentials which, it has been suggested, can duplicate these behaviours. Our aim is to study a particular instance of a core-softened potential, and examine how, or indeed whether, it exhibits these behaviours. Following this, in chapter 3, we use an exactly solvable one-dimensional system to show these behaviours in detail. We then move to our specific two dimensional model. In chapter 4, we take a first approximation to our system's solid-state phase behaviour, using the harmonic approximation method. In chapter 5, we use the Lennard-Jones Devonshire cell model to approximate the liquid state phase behaviour. Finally, we turn to the powerful method of Monte Carlo simulation to examine the full phase behaviour of our chosen model; chapter 6 discusses the Monte Carlo methods we use and we present the results from our simulations in chapter 7. We wrap up by drawing together our results and presenting our conclusions in chapter 8.

1.1 Statistical Mechanics and Phase Transitions

Statistical mechanics is the bridge between our ideas on the basic interactions governing the microscopic movements of particles, and the behaviour of macroscopic bodies made up of these particles. This bulk macroscopic behaviour must be determined by these microscopic dynamics, but even in a classical framework, finding the trajectories of all these particles would involve solving of the order of 10^{23} coupled differential equations, and even if this were feasible, the results would be exceedingly non-linear and microscopically chaotic.

Statistical mechanics gives us a probabilistic approach, without considering of the microscopic dynamics of the system. It gives a statistical description of systems, talking about average bulk properties and fluctuations of the system. This is done by considering every possible configuration the system could take, and assigning a probability to each based on macroscopic criteria. This simplifies our problem a little; rather than solving 10^{23} differential equations to track particle trajectories, we now only need to integrate over 10^{23} different variables to find all possible particle configurations. Whilst doing this exactly is unfeasible for all but the simplest systems, there are tricks and approximations we can make to get useful results, greatly helped by the power of modern digital computers. Several such methods are presented in the later chapters of this work; here, we present a brief overview of the underlying theory. Fuller descriptions can be found in references [4] and [5].

1.1.1 Statistical Mechanics

At the heart of this body of theory is the Boltzmann distribution; if we take a system of N particles, where volume V is fixed, and which can exchange energy, E, with a heat bath at temperature T, then the probability of observing the system in a *microstate* (that is, a particular microscopic arrangement of that system) denoted by $\mathbf{\Gamma}$ is given by:

$$p(\mathbf{\Gamma}) = \frac{1}{Z} e^{-\frac{1}{kT}E(\mathbf{\Gamma})} \tag{1.1}$$

where k is the Boltzmann constant, and Z, known as the *partition function,* is a normalisation constant given by:

$$Z = \sum_{\mathbf{\Gamma}} e^{-\frac{1}{kT}E(\mathbf{\Gamma})} \tag{1.2}$$

This assumes that microstates $\mathbf{\Gamma}$ and energy E are discrete; generalisation to continuum systems is simple (see appendix A).

Given this distribution, we can calculate the average observed value for any property of our system; for arbitrary property $\mathcal{A}$, this is given by:

$$\langle \mathcal{A} \rangle = \frac{1}{Z} \sum_{\mathbf{\Gamma}} \mathcal{A}(\mathbf{\Gamma}) e^{-\beta E(\mathbf{\Gamma})} \tag{1.3}$$

where we have introduced the *inverse temperature,* $\beta = 1/kT$, as a notational convenience.

If $\mathcal{A}$ is an extensive variable (that is, it is proportional to N), it can be shown that provided $\langle \mathcal{A} \rangle$ is well defined, fluctuations in $\langle \mathcal{A} \rangle$ will scale with N as $\sim 1/\sqrt{N}$. This means that, for macroscopic systems (very large N), $p(\mathcal{A})$ will be very sharply peaked. In the limit of an infinite system, $p(\mathcal{A})$ will be so sharp as to pick out a single, definite value of $\mathcal{A}$ for the system at a given state point (in this case, constant NVT, the canonical ensemble) . In this *thermodynamic limit,* the properties of the system become definite.

Rather than summing across every possible microstate, $\mathbf{\Gamma}$, it is often useful to phrase equations 1.1 through 1.3 using the *density of states,* $\Omega(E)$. This function is a count of the number of microstates $\mathbf{\Gamma}$ which have energy E; more formally:

$$\Omega(E) = \sum_{\mathbf{\Gamma}} \delta\left(E - E(\mathbf{\Gamma})\right) \tag{1.4}$$

This is equivalent to the concept in quantum mechanics of the *degeneracy* of a state. Now, let us write the probability of observing the system with energy E, that is $p(E)$, in terms of the density of states:

$$p(E) = \frac{1}{Z}\Omega(E) e^{-\beta E} \tag{1.5}$$

We consider the logarithm of the unnormalised probability distribution, $Zp(E)$:

$$\begin{aligned} -\tfrac{1}{\beta}\ln\left(Zp(E)\right) &= -\tfrac{1}{\beta}\ln\left(\Omega(E)e^{-\beta E}\right) \\ &= E - kT\ln\left(\Omega(E)\right) \end{aligned} \tag{1.6}$$

From this, we define the *entropy*, S, of the system:

$$S = k\ln\left(\Omega(E)\right) \tag{1.7}$$

Entropy is a measure of the amount of $\mathbf{\Gamma}$-space the system can explore. It is often described as a measure of disorder - the more microstates a system can explore, the less it is possible to say anything definite about its structure. Using equation 1.7, we can write equation 1.6 as the Helmholtz free energy:

$$\begin{aligned} A &= -\tfrac{1}{\beta}\ln\left(Zp(E)\right) \\ &= E - TS \end{aligned} \tag{1.8}$$

This quantity will be minimised when the probability $p(E)$ is maximised. We see that the behaviour of the system is governed by an interplay between energy minimisation and entropy maximisation, moderated by temperature. At low temperatures, the system will preferentially minimise energy, even if it means being restricted to a very small set of microstates. At high temperatures, entropy maximisation dominates, and the system will move between a large number of microstates, over a wide range of possible energy values.

Macroscopic thermodynamic properties can be calculated from the first derivatives of the free energy with respect to the constraints; for example, in the NVT constrained system, we can calculate entropy S and pressure P from:

$$S = -\left.\tfrac{\partial A}{\partial T}\right|_V \tag{1.9}$$

$$P = -\left.\tfrac{\partial A}{\partial V}\right|_T \tag{1.10}$$

Response functions (also known as susceptibilities, from the terminology for magnetic systems) are calculated by second derivatives of the free energy, for example the constant-pressure specific heat, C_P, and the isothermal compressibility, K_T:

$$\begin{aligned} C_P &\equiv T \left.\frac{\partial S}{\partial T}\right|_{V,P} \\ &= -T \left.\frac{\partial^2 A}{\partial T^2}\right|_{V,P} \end{aligned} \tag{1.11}$$

$$\begin{aligned} K_T &\equiv -\frac{1}{V} \left.\frac{\partial V}{\partial P}\right|_{T} \\ &= \frac{1}{V} \left(\left.\frac{\partial^2 A}{\partial V^2}\right|_{T} \right)^{-1} \end{aligned} \tag{1.12}$$

These response functions can be used to measure fluctuations within the system [6], for instance, compressibility K_T measures fluctuations in volume, whilst constant-pressure specific heat C_P measures fluctuations in entropy.

For it to be possible for a particular macroscopic variable to refer to a possible free energy minimum, that is, to be an equilibrium value, certain conditions on the free energy at that point must hold. These *stability criteria* refer to the *convexity properties* (that is, the sign of the second derivative) of the free energy at that point. Stability implies that infinitesimal fluctuations will neither decrease entropy (if the fluctuations are at fixed E and V), nor increase free energy (at fixed T); as such, the stability criteria for the compressibility and constant-pressure specific heat are:

$$\begin{aligned} K_T &\geq 0 \\ C_P &\geq 0 \end{aligned} \tag{1.13}$$

Comparison with equations 1.11 and 1.12 tell us that the Helmholtz free energy must be *concave* with respect to temperature ($\frac{\partial^2 A}{\delta T^2} < 0$) and *convex* with respect to volume ($\frac{\partial^2 A}{\partial V^2} > 0$) in order to be stable.

It is possible to write equivalent expressions for all of the above upon relaxing the conditions of either constant volume (for which we must state an applied pressure P) or constant particle number (for which we must state the chemical potential μ of the system). Equivalent probability distributions and free energy expressions can be written for these *open ensembles* - see appendix A. Free energies for these open ensembles are referred to as Gibbs free energies, denoted G.

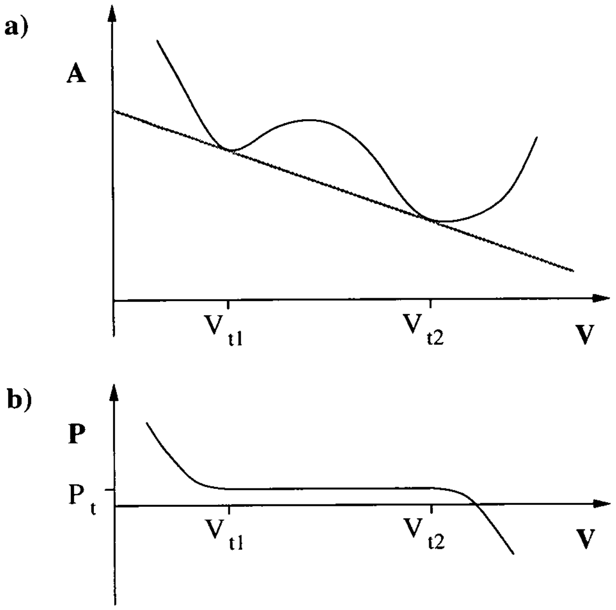

Figure 1.1: a) A schematic Helmholtz free energy curve with respect to volume; this curve has two minima, and will exhibit phase coexistence. The thick grey line shows a "common tangent construction" - this is the lowest line tangential to both minima. Its gradient is minus the coexistence pressure, and it intercepts the free energy curve at the coexistence volumes V_{t1} and V_{t2}.
b) Pressure against volume for this system. Between the coexistence volumes, there is a discontinuity in volume with respect to pressure.

1.1.2 Phases and Phase Transitions

We now consider a system with the Helmholtz free energy curve $A(V)$ at given T shown in figure 1.1 a. We see that here we have two free energy minima. Let us consider the behaviour of the system at constant temperature as we raise the constrained volume from V_1. As we increase volume up to V_{t1}, pressure will gradually decrease (see equation 1.10), and the mesoscopic arrangement of the system will remain homogeneous (that is, the bulk density of different regions will be the same). However, when we move above V_{t1}, but below V_{t2}, the system can lower its free energy by becoming heterogeneous - by splitting itself with some parts having specific volume v_{t1} and others having specific volume v_{t2}, whilst retaining total constrained volume $V_{t1} < V < V_{t2}$. From equation 1.10, we can say that to do this, the pressures at these two volumes must be equal, $P(V_{t1}) = P(V_{t2}) = P_t$ otherwise the system could lose free energy by moving to one volume or the other[1]. Since the pressure must be equal, we can find the coexisting volumes by making a *common tangent construction* as shown in figure 1.1. This effectively splits the system into two subsystems, each having fixed NPT rather than NVT. Each subsystem must therefore have equal Gibbs free energy G.

Moving between V_{t1} and V_{t2}, we stay at constant pressure with increasing volume, with the system split between two coexisting specific volumes; this is a *phase coexistence* between the microscopic structures (phases) represented by the two Helmholtz free energy minima. Above V_{t2}, it is no longer preferable for the system to split, and we return to normal behaviour.

Now consider the behaviour, not at constrained volume, but at constrained pressure. This is shown in figure 1.1 b. We see a discontinuity in volume with respect to pressure at P_t. At exactly the transition temperature, P_t, the system will be exactly split between the coexisting phases. Such a discontinuity in a first derivative of the free energy with respect to an applied field is known as a *first order phase transition.*

Finally, we consider the behaviour as we vary temperature T. Figure 1.2 a shows $A(V)$ curves at a variety of temperatures. Figure 1.2 b is a *phase diagram* showing the volume-temperature behaviour; the shaded area shows constrained volumes at which coexistence will occur, and the thick line shows the volumes of the coexisting phases at that temperature. Figure 1.2 c shows the behaviour in temperature-pressure space, with the thick line showing the locus of the

---

[1] Similarly, the chemical potential $\mu = \left.\frac{\partial A}{\partial N}\right|_{T,V}$ must be equal for the two coexisting volumes.

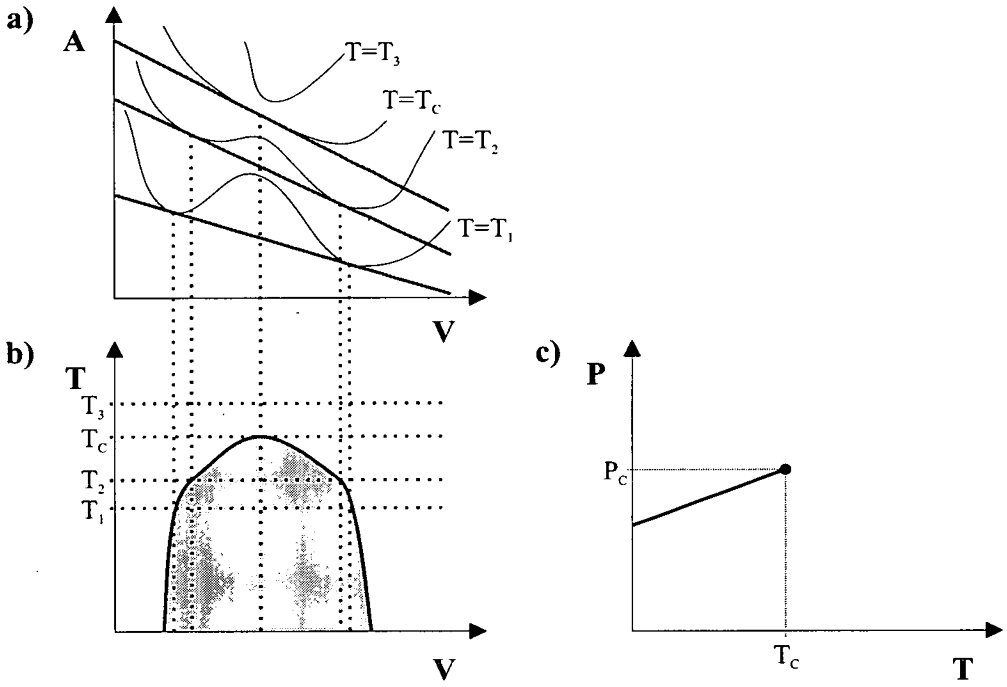

Figure 1.2: a) Helmholtz free energy curves with respect to volume at four temperatures, $T_1 < T_2 < T_C < T_3$. Where there is a phase transition, the thick grey line indicates the common tangent construction. Descending dotted lines indicate coexistence volumes.
b) Phase diagram in volume-temperature space for the system with free energy curves as shown in figure 1.2 a. The thick black line indicates the envelope of coexisting volumes; the shaded area shows volumes where phase coexistence will occur. Horizontal dotted lines indicate the temperatures for which free energies are plotted in figure 1.2 a, descending dotted lines indicate the coexistence volumes from those free energies.
c) Phase diagram in pressure-temperature space for the system with free energy curves as shown in figure 1.2 a. The black line indicates the locus of pressures at which phase coexistence will occur. The dot at $P = P_C$ and $T = T_C$ shows the "critical point", where the line of first-order transition comes to an end at a point of continuous transition.

transition. Exactly at temperature T_C and pressure P_C, the coexisting phases have the *same* volume; at this *critical point*, rather than seeing a discontinuity in volume, we see a singularity in the isothermal compressibility. Singularities or discontinuities in second derivatives of the free energy are known as *continuous* or *second order* phase transitions. Above the critical temperature, T_C, there is no longer a phase transition.

The response function singularities at second order transitions are associated with infinite fluctuations and diverging correlation lengths. These are, of course, impossible to realise in a finite system; the cutoff imposed by finite size makes it impossible to tell the difference between a true continuous transition and a first-order transition in which the order parameter shift is simply smaller than the resolution of the experiment, a "weak" first order transition. As such, it is not possible to prove a transition line to be unequivocally second order by direct experimental observation.

Even strongly first order transitions can raise problems. The physical rearrangement of particles necessary to pass between free energy wells may be difficult for the system, and unlikely to occur over the timescale of observation. A good example of this is diamond - at room temperature and pressure, the thermodynamically stable structure of carbon is graphite, however, the contents of De Beers warehouses are unlikely to become valuable only to pencil manufacturers any time soon. The intermediate states between diamond and graphite have very high a free energy, and therefore a very low probability of occurring. This phenomenon (observation of a system in a local rather than a global free energy minimum) is called *metastability*. Metastable phases may persist above (superheating) or below (supercooling) transition temperatures, as appropriate, though they may have short lifetimes until a large enough fluctuation takes them into the stable phase. The final limit of metastability is the *spinodal*, the order parameter value (and associated temperature and pressure limits) beyond which the free energy curve for that phase breaches stability conditions. The textbook by Debenedetti [7] covers many details of metastability, particularly with regard to the liquid state.

1.2 States of Matter

So far we have discussed phases as different structures, without mentioning what those structures might be. We will now talk about the phase diagram of a "typical" system, in which

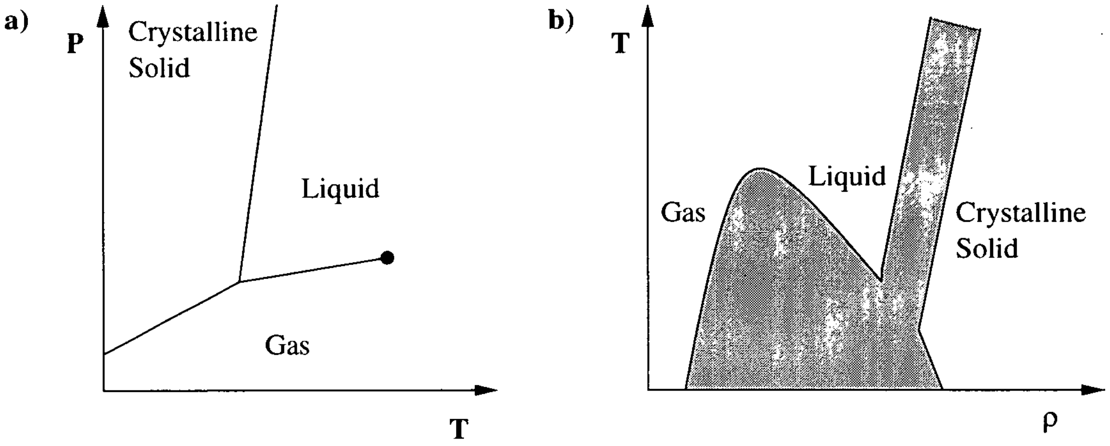

Figure 1.3: Standard pedagogical phase diagram, based on that of Argon.
a) Temperature-pressure projection.
b) Volume-temperature projection.

particles are approximately spherical and only of a single type. We will not talk about mixtures, polymers, or liquid crystals; nor will we venture into electronic or quantum effects, such as those which may give rise to plasmas, superconductors, Bose-Einstein condensates, and so forth. We restrict ourselves entirely to the classical regime and those states of matter we meet day to day.

The "standard" pedagogic phase diagram for such a system is shown in figure 1.3. We see three familiar phases; gas, liquid, and solid. We will discuss each of these classes of structure in turn. The reader is referred to reference [8] and references below for more information.

1.2.1 Fluid States

The characteristic of a fluid state is flow; macroscopically, fluids have neither rigidity nor fixed shape. Both gas and liquid phases have a fluid structure. Everyday examples are air, water, milk, and treacle. Microscopically, this structure is defined by a lack of long range structure, or equivalently, by stating that average properties are *invariant* under any combination of translation and rotation transformations. This implies a very high degree of symmetry.

Long range ordering of particles (or lack thereof) is best illustrated with the *radial distribution function* $g(r)$. This function gives the correlation between particle positions, that is, the probability of finding two particles in the system separated by distance. r, relative to the

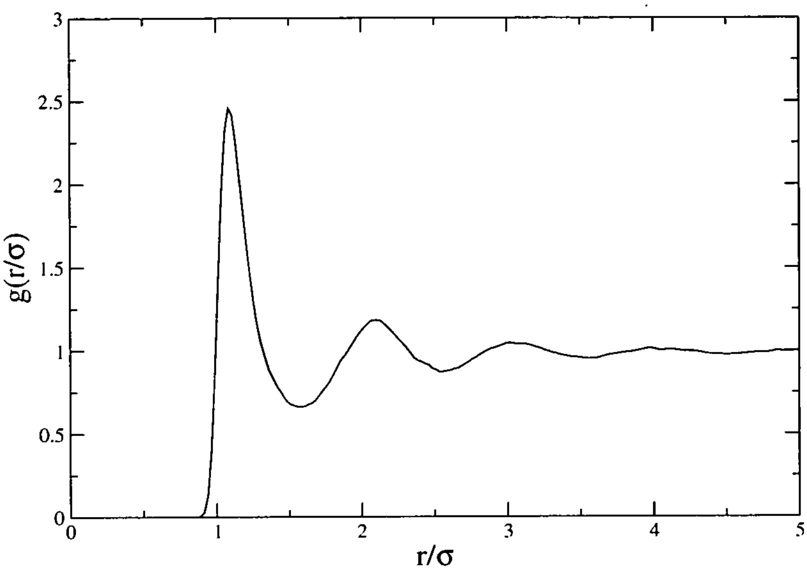

Figure 1.4: Radial distribution function $g(r)$ data for a Lennard-Jones fluid.

probability for a completely uniform distribution. In three dimensions it is given by:

$$g(r) = \rho^{-2} \left\langle \sum_{i} \sum_{j \neq i} \delta \left(r - |\mathbf{r}_i - \mathbf{r}_j| \right) \right\rangle \tag{1.14}$$

An example for a Lennard-Jones fluid is shown in figure 1.4. We see a strong peak at the nearest neighbour distance. At low separation, the correlations are dominated by the repulsive forces. As we move to larger separations, we see progressively smaller and wider peaks at further neighbour shells, as the disorder of the liquid averages out the short-range correlations. The heights of these peaks should exhibit an exponential decay to unity, the value for a completely uniform particle distribution. The fluid phase is also isotropic; the equivalent angular distribution function will also fall off to unity in an exponential decay.

The fluid phase represents a large area of the microstate phase space; as such, fluids have high entropies, and are favoured at high temperature. They have large values for response functions such as compressibility and expansivity.

The first order gas-liquid transition is caused by attractive interactions within the fluid, thus competition between high density, low energy liquid configurations, favoured at low temperature, and low density, high entropy gas configurations, favoured at high temperature. At sufficiently high temperature, this competition disappears, as the entropy comes to dominate the free energy; the transition line terminates at a critical point. Without attractive interactions

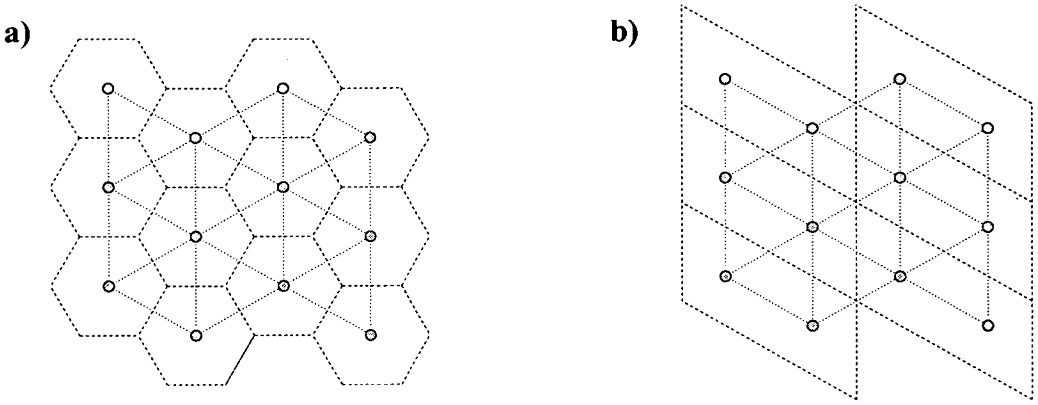

Figure 1.5: Triangular lattice constructed using two different unit cells and bases. Circles show positions of particles, dashed lines show outlines of unit cells, dotted lines join nearest-neighbour particles.
a) Triangular lattice constructed using a hexagonal unit cell with the basis as a single particle at the centre of that cell.
b) Triangular lattice constructed using parallelogram unit cell with two-particle basis.

(for instance, in hard sphere systems), the competition is absent, as is the transition.

1.2.2 Solid States

The solid state is characterised by rigidity; a solid has a fixed shape, and does not flow. Some have full long-range order; these crystalline, or lattice structures are composed of regular arrangements of particles repeated across space. The peculiar hexatic phase, which can only exist in two dimensions, has long-range bond orientational order, but no translational order. Other states, known as glasses, are microscopically arranged like fluids, that is, with no long-range order at all; opinion is divided as to whether they form a strictly thermodynamically separate state.

Crystals

Crystals are solid phases with long-range order and restricted symmetries. They are usually hard yet brittle. Good day-to-day examples are sugar, table salt and quartz, as well as pure metals. The physics of these structures are described extensively in reference [9].

A perfect crystal is made up of a periodic array of particles, such as the triangular crystal shown in figure 1.5 a. This structure is made up of two parts. The first part is the *unit cell.* This is a volume of space, shaped such that it can be repeated (preserving orientation) to fill space. The unit cell contains a number of particles; the set of particle positions relative to the centre of the cell is called the *basis*. By filling space with the repeated unit cell containing the basis, we gain a crystal structure; figure 1.5 a shows a unit cell (the dashed hexagon) and basis (a single particle in the centre of that hexagon) used to construct a triangular lattice. Choice of unit cell and basis does not uniquely define a crystal structure; figure 1.5 b shows an alternate unit cell (a parallelogram) and a two-particle basis used to construct the same structure as figure 1.5 a.

Equivalent sites within each unit cell are joined by *lattice vectors*, $\mathbf{R}$. In d dimensions, lattice vectors are any linear combination of a set of d *primitive lattice vectors* $\mathbf{a}_1, \ldots, \mathbf{a}_d$, such that:

$$\mathbf{R} = l_1\mathbf{a}_1 + l_2\mathbf{a}_2 + \ldots + l_d\mathbf{a}_d \tag{1.15}$$

where l_i are integers, and the primitive lattice vectors cannot all lie in the same plane. Once again, these primitive lattice vectors are not uniquely specified for a given lattice. The positions of particles are invariant upon any combination of translations of the entire crystal through a lattice vector (long range translational order). Similarly, the positions of particles are invariant over a limited set of possible rotations of the entire crystal (long range orientational order).

We refer to the positions of particles in this "perfect crystal" as *lattice sites*; this is not strictly accurate crystallographic terminology, but is a useful and commonly used shorthand. In a "real" ($T > 0$) crystal, particles will make excursions from their lattice sites; however, each particle will be associated with a single lattice site, which will be its average position in time or ensemble. Similarly, in a real crystal structure, there will be *defects*, that is, points where the lattice symmetry is not perfect.

The radial distribution function for a crystal will show sets of strong peaks at each neighbour shell distance. For a perfect crystal, these peaks would be δ-functions, but are widened in real systems by thermal fluctuations in position. Between these peaks, the radial distribution function approaches zero. The height of the peaks should fall off algebraically with increasing separation, r.

Strictly speaking, crystal structures like this only exist in three and higher dimensions. Below three dimensions, and at non-zero T, mean-square deviation from expected particle separations increases monotonically with increasing particle separation [10, 11]. In one dimension, this effect is so severe (with the mean square deviation increasing as the square of distance) that only the fluid state can be stable, with thermal motion literally shaking any periodic structure to pieces. In two dimensions, things are less clear cut; mean square deviation increases with the logarithm of separation. Whilst this forbids long-range translational order in the true infinite system size limit, the decay of long range order may be so weak "as to allow two-dimensional systems of less than astronomic size to display crystalline order" [11]. Further, whilst infinite two dimensional systems may have only quasi-long range *translational* order, true long range *orientational* order may persist [11].

Hexatics

The unusual hexatic phase can only exist in two dimensions, as a consequence of the peculiar melting behaviour of two dimensional crystals. This matter was originally investigated by Kosterlitz and Thouless [12], who followed suggestions that melting in two dimensions was mediated by the presence of dislocation defects, that is, defects in the translational order of the crystal. They proposed that, for a two dimensional crystal at low temperatures, dislocations with opposite direction occur in close-bound pairs, but that above a certain temperature, they may disassociate, causing melting. Extension of this theory by Halperin and Nelson [13], suggests that the second order dislocation-pair disassociation transition is not sufficient to take the system to a fully isotropic liquid, but instead to a *hexatic* phase, where, whilst there is no translational order ($g(r)$ peak height decaying exponentially), long-range bond orientational order remains. At higher temperature still, disclination defect pairs (pairs of defects in the bond orientational order) within the hexatic become unbound through a second continuous transition, forming a true liquid. It should be noted that it is possible for disclination and dislocation pairs to become unbound together, to give traditional first-order melting directly from crystal to liquid.

Whether this continuous melting scenario "really" occurs for two-dimensional systems is still a matter of some controversy [14]. However, the Kosterlitz-Thouless-Halperin-Nelson (KTHN) theory is still the closest to a rigorous theory of melting that condensed matter physics can offer.

Glasses

Glasses (or amorphs) are solid (that is, rigid) structures without any long-range ordering - the generally-encountered example is window glass, amorphous SiO_2. They can be formed by cooling a liquid far below the melting transition in a manner that suppresses crystallisation; the typical method is very rapid cooling, or "quenching". At low enough temperatures, the liquid becomes structurally arrested; particles explore the configuration space extremely slowly with respect to the timescale of observation (tens of seconds in supercooled water experiments [7], upwards of hundreds of years for panes of glass). This is reflected in a rapid and continuous increase in viscosity, to the point of rigidity. The resulting structure will be metastable with respect to a crystalline phase, but the structural arrest prevents crystallisation.

Opinion is divided upon whether glasses are truly a separate phase from liquids, separated by a second-order "vitrification" transition, or if instead the transition is strictly a matter of kinetics and broken ergodicity. These two competing viewpoints are outside the scope of this work - a good primer can be found in reference [7].

Chapter 2

Background and Review

In this chapter, we will first discuss certain unusual phase behaviours - liquid state anomalies, fluid-fluid transitions and isostructural solid transitions - and give examples experimentally observed in real systems. Then we shall present a class of simple model potential ("core-softened" potentials), and review the literature surrounding these potentials. Through this, we hope to convince the reader that the varying classes of unusual phase behaviour we have discussed can all be shown by simple systems interacting via such core-softened potentials. Finally, we will summarise how the study of such systems may help us, both in our understanding of unusual experimental phenomena, and more widely in our understanding of phase behaviour in general, and state those facets of the matter which we will be examining in the rest of this thesis.

2.1 Anomalous Phase Behaviour

2.1.1 Liquid State Anomalies

That most ubiquitous of substances, water, exhibits several unusual behaviours in its liquid state, which continue to draw research and speculation to the present day. Most notable (and, indeed, known to most school children) is the anomalous behaviour of the density of water as a function of temperature. Where a substance can normally be expected to contract on cooling, liquid water exhibits a *density maximum* at around 4°C (that is, 277K); below this temperature, water actually expands upon cooling. This continues right up until freezing occurs, when water freezes into ice (or, more properly, ice $\mathrm{I_h}$), a solid phase which is peculiarly *less* dense than the

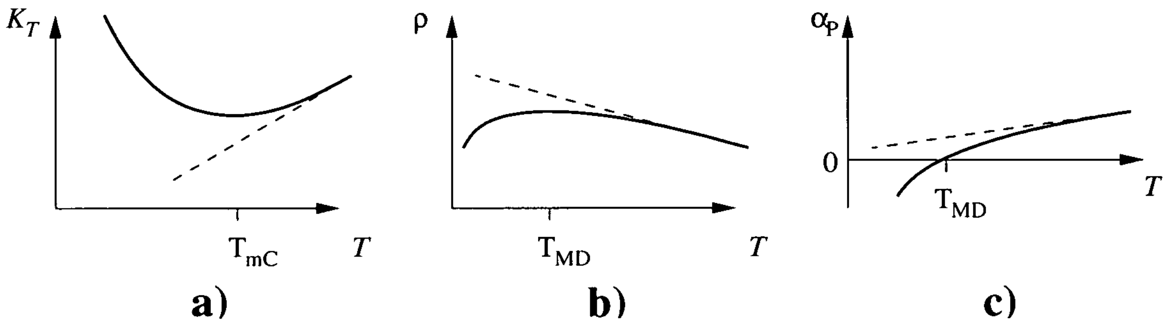

Figure 2.1: Schematic representations of liquid state compressibility and density anomalies. Solid lines show the behaviour of an anomalous liquid such as water - dashed lines show typical liquid behaviour.
a) Behaviour of isothermal compressibility, K_T with temperature. The dashed line shows K_T for a typical liquid decreasing monotonically with decreasing temperature. The compressibility of liquid water shows a minimum at $T_{mC} = 319$K, below which it increases upon further cooling.
b) Behaviour of the density, ρ, with temperature. In a normal liquid, density will increase monotonically upon cooling. Water shows a density maximum, with density falling upon cooling below a temperature $T_{MD} = 277$K.
c) The density maximum can also be seen in the behaviour of the thermal expansion coefficient, $\alpha_P = \frac{1}{V} \frac{\partial V}{\partial T}\big|_P$, with temperature. For a normal liquid, α_P will decrease on cooling, but remain positive. Since water has a density maximum, α_P passes through zero at the anomaly temperature T_{MD}, and becomes negative.

liquid phase. Hence, ice floats on water. Less familiar, though equally strange, are the anomalies seen in the response functions of water; a minimum is seen in the isothermal compressibility, K_T, around 46°C, 319K. Anomalous extrema are also seen in several other of water's response functions, including the constant-pressure specific heat, C_P, and the speed of sound through water - see figures 2.1 and 2.2.

Such anomalies occur for several other structurally similar substances, including Si, Ge, SiO_2 and GeO_2. What is most striking about water, however, is the increase in anomalous behaviour upon supercooling. The anomalous effects become ever greater as metastable liquid water is cooled; indeed, extrapolation of experimental results suggests that K_T and C_P exhibit a power-law singularity at a temperature around 228K (−45°C) [15]. Unfortunately, this temperature may be experimentally unrealisable for pure water; below 235K (the homogeneous nucleation temperature), supercooled water spontaneously freezes.

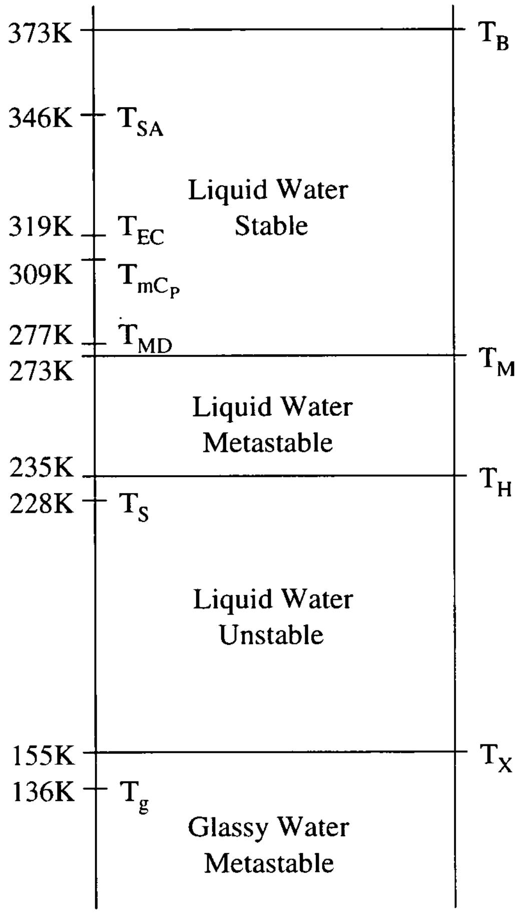

Figure 2.2: Temperature domains for liquid water, adapted from [16]. Between the boiling temperature, $T_B = 373K$, and the melting temperature, $T_M = 273K$, liquid water is stable. It remains metastable down to the temperature of homogeneous nucleation at $T_H = 235K$, below which it will spontaneously crystallise. Metastable glassy water is stable up to the "crystallisation temperature" at $T_X = 155K$, above which it will also spontaneously crystallise. Various anomalies occur for liquid water, including a maximum in the speed of sound (at $T_{SA} = 346K$), a minimum in the isothermal compressibility (at temperature of extremal compressibility $T_{EC} = 319K$), a minimum in the heat capacity (at $T_{mC_P} = 309K$), and a maximum in the density ($T_{MD} = 277K$). If response functions are extrapolated below experimentally realisable temperatures, they go through a power-law singularity at $T_S = 228K$ [15].

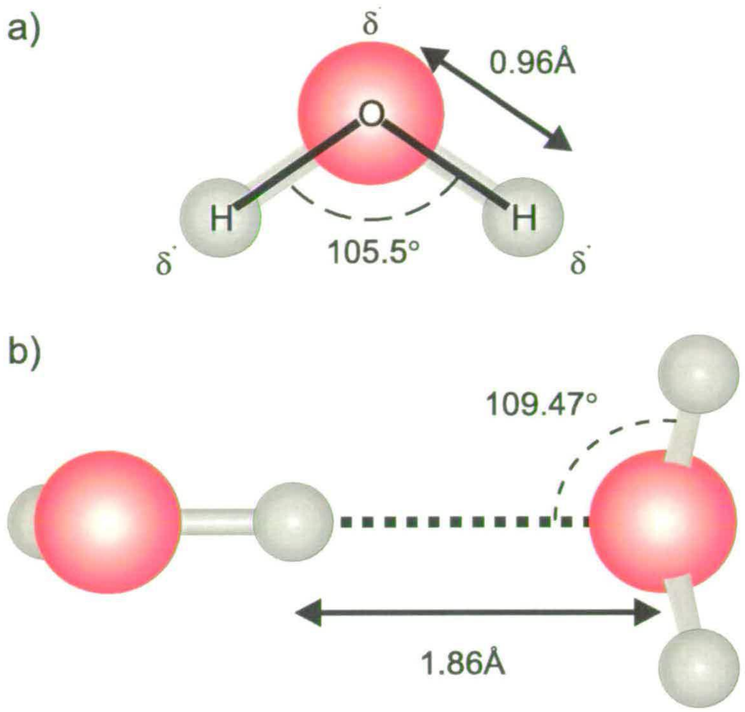

Figure 2.3: a) A water (H_2O) molecule, showing bond length and angle.
b) A hydrogen-bonded water dimer. The hydrogen bond has a strength of around 24kJ/mol, as compared to the covalent $H-O$ bond strength of around 470kJ/mol. The hydrogen bond is not entirely electrostatic in character, with some covalent character (delocalisation of electrons between the oxygen and hydrogen atoms concerned) being shown. The bond strength shows little dependence upon the $H - O \cdots H$ bond angle, with distortions up to around 25° showing little effect. Bond length is more important, with bond strength having been shown to fall off exponentially away from the $O \cdots H$ equilibrium distance of around 1.86Å [17].

Liquid State Anomalies as Structural Competition

The physical origin of these anomalies has been the subject of learned debate for many years. One of the most persuasive arguments of recent years [18] is that they are due to *structural competition* in the fluid. To explain this, let us first consider the water molecule (figure 2.3 a). The hydrogen-oxygen covalent bonds are strongly polarised, giving the hydrogens a slight net positive charge, and the oxygen atom a slight net negative charge; this allows nearby water molecules to form directionally-dependent, short-ranged hydrogen bonds between each other (figure 2.3 b). This bonding is somewhat stronger than Van der Waals interactions, but much weaker than true covalent bonding. All known low pressure solid ice phases involve fully hydrogen-bonded networks of water molecules. In the liquid phase, however, hydrogen-bonded networks are of necessity *transient*, with hydrogen bonds breaking and forming continuously as the molecules

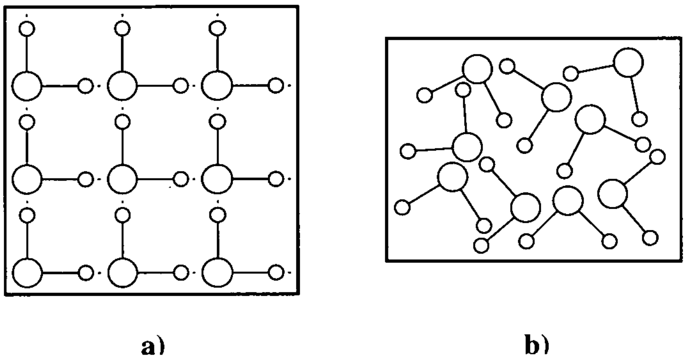

Figure 2.4: a) A network of water-like molecules in 2D. To form the network, the molecules must adopt a very ordered configuration (low entropy), which is also very open.
b) Randomly-packed water-like molecules in 2D. This configuration has much less order than that shown in figure 2.4 a, but is also much more dense.

move, and *short-ranged*, not persisting beyond second- or third-nearest neighbours. Due to the very specific directional and range requirements of hydrogen bonding, such networked clusters will have lower entropy than more traditional randomly-oriented liquid configurations; they will also have a greater specific volume (see figure 2.4) .

As our hypothetical sample of liquid water is cooled, the lower energy of the networked clusters indicates that they will form with greater probability amidst the liquid. The networked clusters take up more volume than the randomly-oriented clusters; if the formation of open clusters with cooling overtakes the contraction of both types of cluster with cooling, volume will increase, and a density maximum will have occurred. This is the same as saying that the entropy and volume of the fluid become *anti-correlated.* We can see this if we cast the thermal expansion coefficient, $\alpha_P = \frac{1}{V} \frac{\partial V}{\partial T}\big|_P$ in terms of fluctuations:

$$\alpha_P = \frac{1}{V} \langle \partial S \partial V \rangle \tag{2.1}$$

When S and V become anti-correlated, α_P passes through zero and becomes negative, and density passes through an extremal point. The temperature at which this occurs will vary with pressure, tracing out a line of temperatures of maximum density (or *TMD line*) through the phase diagram.

A similar explanation can be given for the compressibility anomaly. When both networked and random clusters are possible as equilibrium structures, application of pressure will convert the open, networked clusters back to dense, random clusters. Hence, as open clusters begin to appear with cooling, so the isothermal compressibility, $K_T = -\frac{1}{V}\left.\frac{\partial V}{\partial P}\right|_T$ will begin to increase, against its normal behaviour. Once more, this can be seen by recasting the response function in terms of fluctuations:

$$K_T = \beta \frac{1}{V} \left\langle \partial V^2 \right\rangle \tag{2.2}$$

As the networked clusters appear, whilst volume fluctuations within each type of cluster may be small, the presence of structures with two different equilibrium volumes within the liquid increases the volume fluctuations within the liquid as a whole. Hence K_T will increase upon cooling. Once again, there should be a locus of temperatures of extremal compressibility (*TEC line*) through the phase diagram.

As we cool further, we would expect these functions to return to more normal behaviour, as the open, networked structure comes to dominate the liquid, and fewer random clusters appear. Fluctuations should fall away back to the level within the networked structure, so the compressibility should pass through a maximum and fall again. Similarly, upon cooling, both volume and entropy within the networked clusters alone should begin to fall together on cooling; without random clusters converting to a networked structure, these two variables should correlate normally, α_P should rise back up through zero, and density should see a local minimum and rise with falling temperature once more. Water has not been seen to exhibit this return to "normal" behaviour. Three main explanations for this have been proposed:

1. The **Stability Limit Conjecture**

This hypothesis, due to Speedy [19], suggests that the liquid-gas spinodal line changes from positive to negative slope in the negative pressure regime, retracing back to positive pressures at low temperatures (see figure 2.5 a). In such a situation, as water is supercooled and approaches the spinodal line, it will lose mechanical stability with respect to a supercooled gas phase, signalled by the extrapolated divergence in the response functions. The cause of the re-entrant behaviour is argued to be the inevitable intersection between the negatively-sloped TMD curve and the spinodal line; Speedy [19] has shown through thermodynamic arguments that if the two curves meet, the slope of the spinodal line must change sign.

2. **The Second Critical Point Hypothesis**

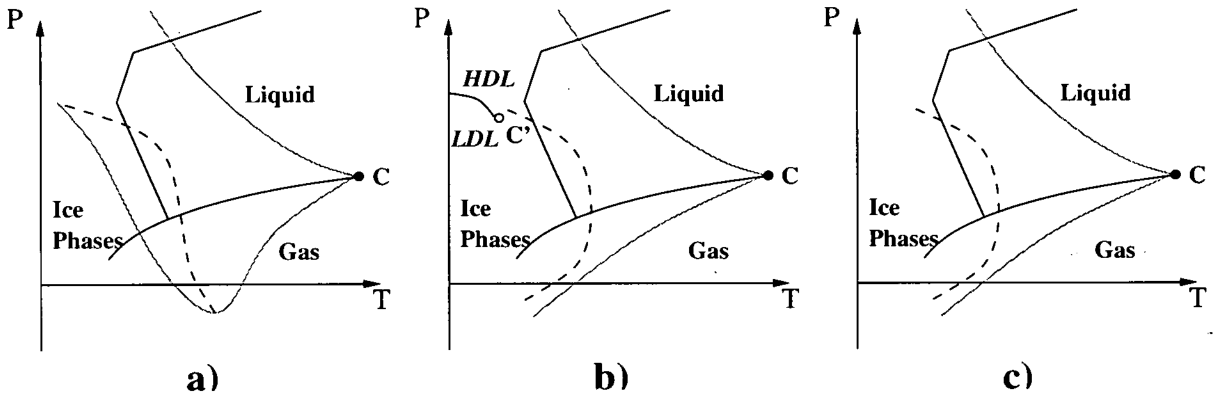

Figure 2.5: Three scenarios for the anomalous properties of water. Solid lines show the line of first order transition separating phases; stable phases are labelled in bold type, metastable phases in bold italic type. Critical points are marked with circles (filled for stable, empty for metastable). The locus of the density anomaly is marked with a dashed line, and the liquid-gas spinodal lines are marked with dot-dashed lines.

a) The Stability Limit Conjecture: the liquid-gas spinodal line begins to retrace at the point where it intersects the TMD line. The anomalies seen are due to approach to this spinodal line, with the associated loss of stability of the liquid phase.

b) The Second Critical Point Hypothesis: metastable with respect to the ice phases, there exists a critical point C′ which separates the liquid phase into low density liquid (LDL) and high density liquid (HDL) forms. The anomalies seen are the effects of this critical point.

c) The Singularity-Free Hypothesis: the anomalies are a "stand-alone" effect, a structural competition effect with no associated thermodynamic singularity.

The second critical point hypothesis [20] suggests that the apparent singularity in supercooled water represents a second critical point. In this explanation, as well as the familiar line of liquid-gas transition and critical point, there exists a second line transition in the fluid phase, also terminating in a critical point. This novel transition is the full fruition of the structural competition in water, and separates the liquid phase into a random-packed high-density liquid (HDL) phase at high pressure, and a strongly-networked low-density liquid at low pressure. The line of first-order transition between these phases terminates in a critical point C' (see figure 2.4 b), and it is the approach to the critical temperature, $T_{C'}$, that is causing the apparent singular behaviour. There is no retracing spinodal, as the TMD line changes slope such that it never intercepts the liquid-gas spinodal curve.

We note that the structure of the strongly-networked phase would still be made up of many separate networked clusters. Though molecules within these clusters would be locally strongly ordered, the clusters would maintain the characteristics of transience and short range. Hence the system as a whole retains the complete orientational and translational symmetry of a fluid phase.

3. Singularity-Free Hypothesis

The theory against which the other hypotheses must be tested is the singularity-free hypothesis. Sastry, et al, [21] have demonstrated through thermodynamic arguments that the compressibility *must* increase on cooling across a TMD line which is negatively sloped in the (T, P) plane. As such, anomalous increase in K_T on cooling does not guarantee approach to a thermodynamic singularity; instead, the extrapolation to an infinite compressibility may be incorrect, with the true behaviour being approach to a finite (yet arbitrarily large) compressibility maximum, below which normal behaviour reasserts itself. In this hypothesis, the structural competition is considered to be powerful enough to give the liquid state anomalies (as described above), but not powerful enough to erupt into a full-blown phase transition. This scenario is illustrated in figure 2.4 c.

Evidence

Since it has not yet proved possible to directly observe liquid water close to the extrapolated singularity, other, more indirect means must be used to study this problem. An important study in this field was carried out by Poole, et al, [20] who used the ST2 model potential for water [22] in molecular dynamics simulations to locate the liquid-gas spinodal curve, as a test of the retracing spinodal hypothesis. Their results showed a spinodal curve that was not re-entrant, instead showing a fluid-fluid transition and critical point as in figure 2.5 b, giving rise to the second critical point hypothesis. Whilst simulation work on real systems can never be seen as definitive (especially with a substance as infamously difficult to simulate as water), Poole's work established the second critical point hypothesis as a serious possibility.

The major experimental evidence for a fluid-fluid transition has come from studies of glassy amorphous water. At atmospheric pressure, only crystalline ice phases are accessible between pure liquid water's temperature of homogeneous nucleation (at around 235K) and a "crystallisation temperature" of around 155K (see figure 2.2). Below this, there is some controversy over whether there exists "ultra-viscous" supercooled liquid water [23], followed by a glass transition at 136K, or whether the actual glass transition is at some temperature above 155K, with liquid water quenched to this temperature falling straight into a glass phase [24]. What is established is that water demonstrates *polyamorphism,* in that there are two *separate* glassy forms - the Low Density Amorph (LDA) and the High Density Amorph (HDA). The LDA form, seen at low pressures, can be prepared through deposition of water molecules on a cold plate[1] [25], and can also be produced by directly quenching liquid water [26]. The high-pressure HDA form was discovered through compression of ice I_h below 150K, but can also be prepared through compression of the LDA form [27]. The transition between the two amorphs appears to be both sharp and reversible, and is accompanied by a large volume change of around 20%. This transition does seem to be first order, though such a description should be used with care around glassy phases.

This polyamorphism may support the second critical point hypothesis as evidence for a fluid-fluid transition in metastable water. It is often claimed [16] that the amorphs LDA and HDA represent kinetically arrested configurations of the LDL and HDL fluids respectively, with the transition between the amorphs being a continuation of a fluid-fluid transition into the glassy regime.

Such claims are not without support. Thermodynamic properties of liquid water at low and high pressures can be extrapolated smoothly through the "no-man's land" between 155K

---

[1] Most water in the universe is believed to exist in the LDA form, depositing from interstellar vapour onto dust particles in exactly this manner.

and 235K to respective low and high density amorphs [28]. Similarities between the structure factor data for high and low pressure supercooled water and the respective amorphs have also been found [29] (though this remains controversial [30]).The case is, however, certainly not solved; extrapolations can never be relied upon, and some workers suggests that, rather than representing a kinetically arrested HDL phase, the HDA is instead a poorly-crystallised form of ice I_h [31]. Further, the use of glassy phases as putative extensions of liquid phases remains controversial.

The proposed liquid-liquid transition in water is between metastable, supercooled phases, and has so far proved impossible to observe directly in experiment. Rather more concrete evidence of transitions between stable fluid phases is found under extreme conditions in both phosphorus and carbon, which we now describe briefly.

Liquid-Liquid Transitions - Phosphorus

Phosphorus has a rich phase diagram (see [32, 33]), across most of which the atoms remain trivalent and threefold coordinated. Solid phases include four crystalline forms, with rhombohedral, orthorhombic (black phosphorus), cubic (metallic phosphorus), and monoclinic (violet phosphorus) lattices, several amorphous polymeric "red" forms, and a molecular "white" solid, consisting of hexagonal or rhombic dodecahedral arrangements of tetrahedral P_4 molecules. Upon melting at low pressures, phosphorus forms a molecular liquid of such P_4 tetrahedra. Such melts show unusually strong spatial correlations (out to around 20Å, that is, around the fifth nearest neighbour molecule). Molten phosphorus can boil to form a vapour of P_4 molecules; upon further heating, these molecules will dissociate to form a vapour of P_2 dimers. The melting curve of black (orthorhombic) phosphorus shows a maximum with respect to temperature at around 1GPa.

Ab initio molecular dynamics computer simulations [34] of high pressure and temperature molten phosphorus have suggested that the molecular liquid may undergo a first order transition to a polymeric liquid at very high temperatures and pressures. It is suggested that this occurs via "opening" of the P_4 molecules, followed by bonding into a polymer made up of "roof-shaped" monomers. Experimental data appears to confirm this view [35], with a rapid (order of minutes), reversible transformation occurring, observed through X-ray diffraction measurements of the structure factor. The transition line appears to connect to the melting curve of orthorhombic

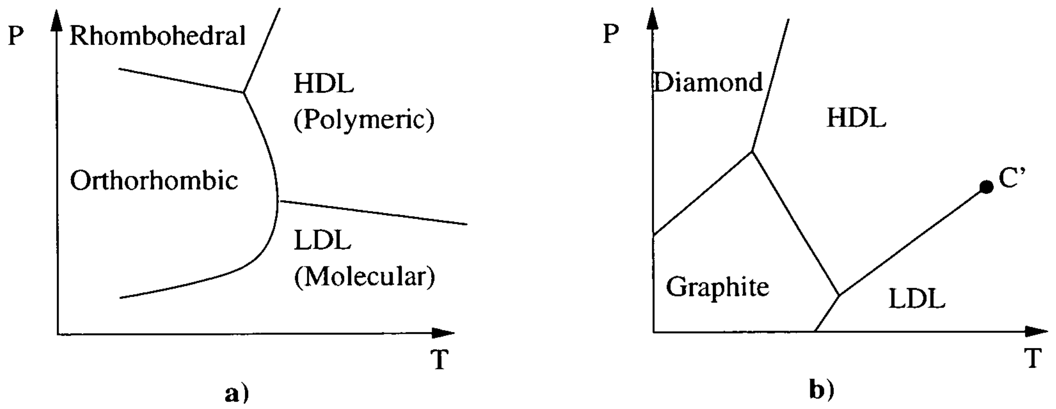

Figure 2.6: Schematic phase diagrams for Phosphorus and Carbon, showing the proposed liquid-liquid phase transitions.
a) Phase diagram for high temperature phosphorus. Upon melting, the orthorhombic phase can become either a molecular low-density liquid (LDL) made up of P_4 units, or a polymeric high-density liquid (HDL) depending upon pressure. The two liquids are separated by a line of first-order transition. The LDL-orthorhombic-HDL triple point is at approximately 1000°C and 1GPa.
b) Phase diagram for high temperature carbon. Graphite can melt into either a low-density liquid with a chain-like character, or a high-density liquid characterised as a tetrahedral network. These liquid phases are separated by a line of first-order transition, terminating in a critical point. The LDL-graphite-HDL triple point is at approximately 4500°C and 5.6GPa.

black phosphorus at or near the melting curve maximum (see figure 2.6 a), suggesting that the maximum is not a continuous change in the slope of the melting curve, but is instead a discontinuity, reflecting the transition between a liquid phase denser than the solid and a liquid phase less dense than the solid.

The slope of the line of fluid-fluid transition here does appear to be negative, showing the entropy-volume anticorrelation between structures we have noted above. However, the polymeric liquid and molecular liquid have an essentially different symmetry, and so this transition could not demonstrate a critical point in the same way as the proposed liquid-liquid transition in water. Though phenomenologically closer to the "λ-transition" in liquid sulphur (polymeric to S_8), this transition makes a good counterpoint to the hypothesised transition in water.

Liquid-Liquid Transitions - Carbon

Another proposed liquid-liquid transition may occur in liquid carbon. The melting curve of graphite shows an maximal point with respect to temperature at around 5.6GPa. Careful study of this curve [36] suggests that, once again, this is not a smooth maximum but a discontinuity.

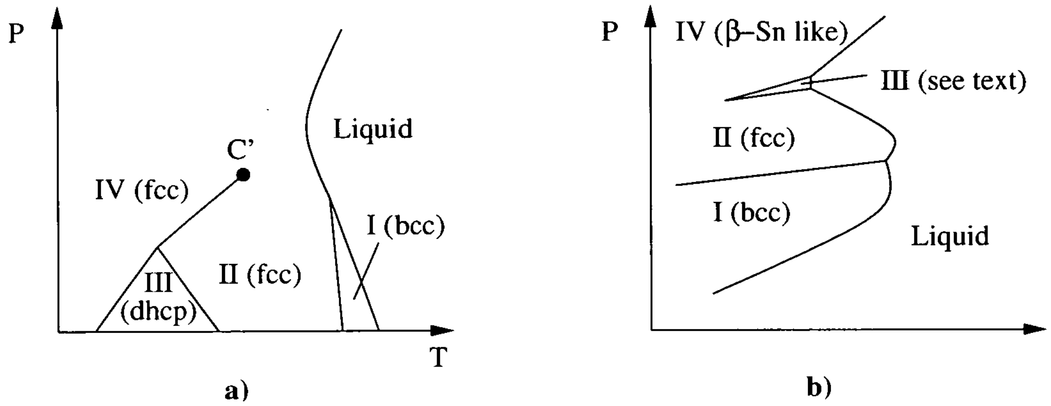

Figure 2.7: Schematic phase diagrams for Cerium and Cesium.
a) Phase diagram for Cerium. There is a critical point, C', terminating an isostructural transition between the fcc phases II and IV.
b) Phase diagram for Cesium. This system was long thought to also demonstrate an isostructural transition between fcc phases II and III, however, phase III is now widely believed to be a complex large supercell structure [41].

Data from the same study on resistivity of the liquid phase appears to show a discontinuity at around the same pressure, strongly suggesting that the liquid undergoes a first-order transition.

A molecular dynamics simulation study of carbon [37] gives results supporting this hypothesis, showing the discontinuity in slope of the graphite melting curve as a result of a stable liquid-liquid phase transition with critical point (see figure 2.6 b). From these results, the low pressure low, density liquid form is largely two-fold coordinated, with a chain-like, polymeric structure. The high pressure high, density liquid form is almost entirely four-fold coordinated, forming a dense diamond-like tetrahedral network.

2.1.2 Isostructural Lattice Transitions

At atmospheric pressure, there exist four stable crystal forms of the rare earth metal Cerium. At high temperature, the stable phase I, $\delta - \mathrm{Ce}$, has a body centred cubic (bcc) lattice. This cools to a face centred cubic (fcc) phase II ($\gamma - \mathrm{Ce}$), with lattice spacing $a \approx 0.52\mathrm{nm}$, at approximately $726°C$. Upon further cooling, Cerium passes through a double-hcp phase III ($\beta - \mathrm{Ce}$) at round $53°C$, then into the low-temperature phase IV ($\alpha - \mathrm{Ce}$) at around 96K - this phase IV is fcc with lattice spacing $a = 0.485\mathrm{nm}$.

As pressure is increased, the temperature stability range of phase III decreases. At a temperature of around 0.25GPa, phases II, III and IV meet at a triple point, and above this, phase

III is no longer stable, leaving a first order transition line between the fcc phases II and IV, across which there is a loss in volume of around 14.5%. This transition is marked by neither a change in lattice symmetry, nor in magnetic symmetry (both phases being paramagnetic), and was the first isostructural transition discovered in which the order parameter is simply the lattice spacing of the crystal[2]. Even more peculiarly, this line appears to terminate in a critical point at around 1.46GPa and 480K, above which phases II and IV appear to cease to have separate identities. Cerium is the only element known to exhibit such a stable isostructural critical point, and as such its properties have come in for a great deal of study. Much of this attention has focused on altering the position of the critical point through alloying and doping the metal with other rare earths and Thorium (see the indispensable reference [32] and references therein). Cerium is also noteworthy for having a minimum with respect to pressure in the melting curve (at approximately 3.3GPa and 660°C) in the supercritical fcc phase regime.

The isostructural transition in Cerium is credited to a pressure-induced transition in the $4f$ electrons of $\gamma - \mathrm{Ce}$, leading to a sudden diminution of the effective core diameter for the Cesium atoms. Whilst the exact nature of this transition remains a matter of debate [40], the general idea of pressure-induced *core collapse* seems sound.

The alkali metal Cesium was long thought to exhibit a similar fcc–fcc isostructural transition between phases II and III, associated with a fall in volume of around 9%, though with any critical point forestalled by melting. This transition was also generally accredited to electron core collapse (in this case, a pressure driven $6s \to 5d$ transfer). However, recent experimental evidence [41] strongly suggests that phase III is not fcc but instead has a complex large-period supercell structure. This is backed up by theoretical studies suggesting that the fcc phase is mechanically unstable at the densities seen in the Cs III phase [42].

2.1.3 Anomalous Phase Behaviour - Summary

The links between isostructural lattice transitions and liquid state anomalies are stronger than they may seem at first. Both rely on the existence of two distinct equilibrium particle separations in a substance. In water, these separations correspond to the widely-spaced hydrogen bonded networks, and randomly packed molecules. In Cerium, the two different stable electron

---

[2] It should be noted that in recent papers, it has been suggested that there is some essential difference between the phases (either $\alpha - \mathrm{Ce}$ having a subtly distorted fcc structure [38], or in a hidden electronic structure symmetry [39]), such that the observed critical point is actually a tricritical point, with the transition continuing as second order beyond this.

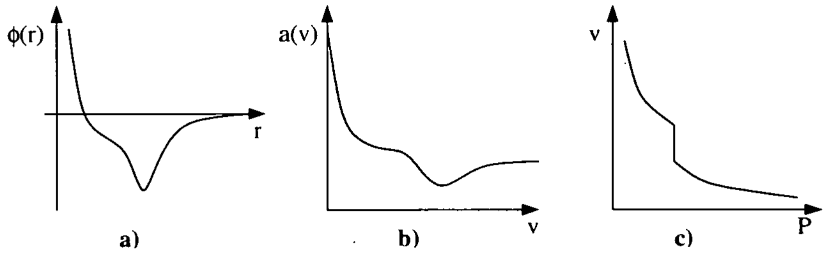

Figure 2.8: a) "Core-softened" interparticle potential; this has a "shoulder" (region of negative curvature) in its core.
b) Energy density with respect to volume for a system interacting via the potential shown in figure 2.8 a. At zero temperature, this is equal to the Helmholtz free energy.
c) Volume as a function of pressure for the zero-temperature system. This has a discontinuity.

structures provide two discrete core radii. These distinct particle separations give rise to two competing structures with the same symmetry, be that the continuous symmetry of the liquid state or the lattice symmetry of an fcc crystal. Further, if the second critical point hypothesis is true, then both water-like and Cerium-like systems have a full, first-order phase transition between phases of the same symmetry.

We have now tentatively identified a common factor between these two types of phase behaviour. We will now identify a class of simple interparticle potential which can, perhaps surprisingly, demonstrate liquid state anomalies, isostructural solid-solid transitions, and liquid-liquid transitions, without dealing with the complicated directional character of the water molecule, or the quantum mechanical electron orbitals of Cerium atoms.

2.2 Core-Softened Potentials

2.2.1 What is Core-Softening?

In order to model the behaviours described above, we desire an interparticle potential which will show two distinct possible particle separations in thermodynamic equilibrium, selected between by an externally applied field.

We know that the stable volume of the system at given (P, T) will be that for which the free energy is minimal and that only volumes at which the free energy is *convex* with respect to volume can be thermodynamically stable. Let us consider a system of particles at zero temperature. We will now suppose the particles to be interacting via an interparticle potential with a region in the repulsive core where the potential is both repulsive $(\frac{\partial \phi(r)}{\partial r} < 0)$ and concave

($\frac{\partial^2\phi(r)}{\partial r^2} < 0$) with respect to the interparticle separation, as shown in figure 2.8 a. At zero temperature, this concavity will be reflected in the function $e(v)$, and hence into the Helmholtz free energy curve (see figure 2.8 b). We can see that the equilibrium volume will no longer be a continuous function of pressure. We have introduced a first-order phase transition at a pressure P', as shown in figure 2.8 c, without assuming any change in the symmetry of the system.

The presence of such a shoulder in the repulsive core of a potential is known as *core-softening*, in analogy to the phenomena of electronic core collapse in Cerium. Potentials exhibiting such a region are known as *core-softened.*

Of course, the presence of such a transition at zero temperature does not indicate that the structure exhibiting such a transition at a given pressure will be the structure which is thermodynamically stable at that pressure. Nor does it indicate that phases stable at non-zero temperature will exhibit such transitions. Above $T = 0$, entropy must enter our considerations, and the curves shown in figures 2.8 b and c will become three-dimensional entropy-energy-volume landscapes, one for each possible structure, and such a simple analysis becomes impossible. However, the possibility that such a potential *could* exhibit a transition between phases of the same symmetry is demonstrated.

2.2.2 Stell-Hemmer Potentials - Early Work

The idea of core-softening was introduced by Stell and Hemmer in a 1970 paper [43], where they demonstrated that a core-softened potential could introduce "extra" phase transitions in both a lattice gas system of any dimensionality, and in a one-dimensional continuum system. We will review their argument here.

The Lattice Gas

A lattice gas is a simple model of a cell system, in which space is discretised into lattice points. Each lattice point is associated with an "occupancy number"; this is, the number of particles occupying the area of space corresponding to that lattice point. The interaction between particles is represented with a potential, depending only upon the relative location of lattice points and their occupancies. We represent the "hard core" repulsion of particles by allowing only occupancy numbers of 0 or 1. It can be seen that the lattice gas is equivalent to a spin system, and that by restricting the occupancy to have only two possible values, we have

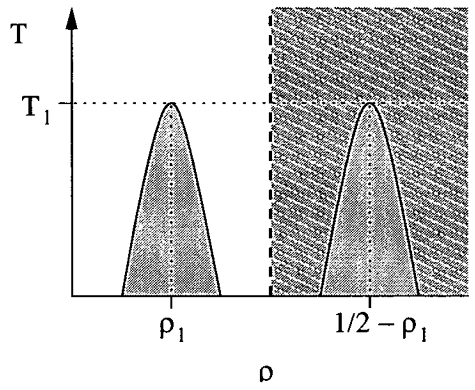

Figure 2.9: Lattice gas model phase diagram. The dashed line shows the line of symmetry around $\rho = \frac{1}{2}$; if interactions between adjacent sites are infinite, state points at densities above this line of symmetry (light shaded area) are unphysical, and only the transition at densities below the line of symmetry is seen. If interactions between adjacent sites are finite and very large, the entire state space is available, and the conjugate transition at $\rho > \frac{1}{2}$ becomes physical.

made our lattice gas equivalent to an Ising model.

Such a system has a symmetry between occupied sites ("particles") and unoccupied sites ("holes") [44]. A consequence of this symmetry is that the properties of every thermodynamic state point of the system can be calculated from the properties of another state point. This "mapping" between state points is reversible (if point $\mathcal{A}$ maps to point $\mathcal{A}'$, then point $\mathcal{A}'$ maps to point $\mathcal{A}$) and single-valued (point $\mathcal{A}$ is the *only* point which maps to point $\mathcal{A}'$), and points may map onto themselves (the locus of such points forms a single *line of symmetry* through the phase diagram). The mapping corresponds to "flipping the spins" on every lattice site in the system (that is, converting every lattice point with occupancy 0 to occupancy 1 and vice versa). The mapping between the thermodynamic functions of conjugate state points is relatively simple; the important parts for our argument are:

$$\begin{aligned} T &= T' \\ (\rho - \tfrac{1}{2}) &= (\tfrac{1}{2} - \rho') \end{aligned} \tag{2.3}$$

Now, consider a lattice gas system in which pairs of particles cannot occupy adjacent sites, that is, the potential V_0 between particles at adjacent sites is infinite. Further, there is an interaction acting between particles in non-adjacent sites capable of producing a line of first-order transition with a critical point at (ρ_l, T_l)[3]. The infinite interaction between adjacent

---

[3] In two or higher dimensions, most attractive potentials are capable of giving such a system a gas-liquid like transition. In one dimension, the attraction will have to be long ranged.

occupied sites constrains the density of the system to be less than or equal to $\frac{1}{2}$; whilst the conjugate pairs for the available state points exist, they are non-physical, as they have infinite energy.

We now take the interaction V_0 acting between adjacent sites to be finite but arbitrarily large. The factor V_0 enters the equation of state only through the Boltzmann factor $e^{-\beta V_0}$; since V_0 can be made arbitrarily large, this exponential can be made arbitrarily small, and hence the change in the $\rho \leq \frac{1}{2}$ part of the phase diagram can be made arbitrarily small. However, the $\rho > \frac{1}{2}$ part of the phase diagram has now become physically accessible, and with it a conjugate state "image" critical point (arbitrarily close to $(1 - \rho_1, T_1)$) and associated line of transitions, guaranteed through the continuity of the mapping (see figure 2.9). This has the effect of bringing a second transition to the system.

Extending this argument to real systems is tentative at best; the lattice gas model is quite basic, and the particle-hole symmetry which the argument rests upon is not applicable to continuum systems. However, exact results for the one dimensional continuous system (also presented in more detail in reference [45]) are more promising.

One Dimensional Continuum Fluid

For this system, particles are considered to interact via the potential given by:

$$\begin{aligned} \phi(r) &= \infty & & r < d \\ &= V_0\left(1 - (r-d)/d\lambda\right) & d &< r < d(1+\lambda) \\ &= -\alpha\gamma e^{-\gamma r} & d(1+\lambda) &< r \end{aligned} \tag{2.4}$$

The form of this potential is shown in figure 2.10 . Without the attractive part, and with $\lambda \leq 1$, this potential will act only between nearest neighbour particles. The exact intensive Helmholtz free energy in one dimension for the nearest neighbour-only potential, a_{nn} can be found using the Takahashi Nearest-Neighbour Gas method (see [46] and chapter 3). However, without the attractive contribution, the system will not exhibit a phase transition at non-zero temperature.

The form of the attractive long-ranged tail, when added to a simple hard core potential, gives a phase diagram with a single line of first-order phase transition, terminating in a critical point. When added to a nearest neighbour potential, this attractive contribution allows calculation

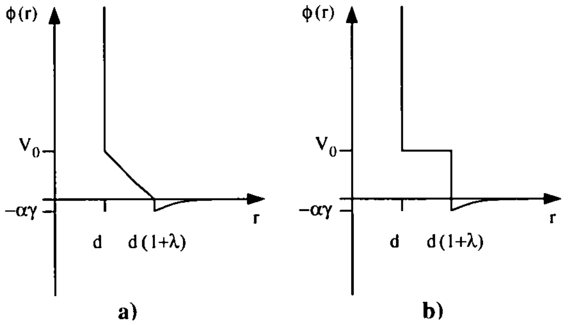

Figure 2.10: a) Ramped core-softened potential with long-range attraction, as given by equation 2.4. b) Shouldered core-softened potential with long-range attraction, as given by equation 2.6.

of the exact free energy in one dimension [47] in the limit $\gamma \longrightarrow 0$ (with large γ, the attraction becomes arbitrarily weak but arbitrarily long ranged). This free energy is given by:

$$a(v,T) = \mathrm{CE}\left(a_{\mathrm{nn}} - \alpha/v\right) \tag{2.5}$$

Here CE denotes the "convex envelope" of the function; that is, CE($A(v)$) is the maximal function convex with respect to the origin, but never higher than the function $A(v)$.

The phase diagram for the full potential depends upon two parameters, λ (the width of the shoulder) and the combination $V_0 d/\alpha$, as shown in figure 2.11 a . It can be seen that, for *all* $\lambda \leq 1$, there exists a value of $V_0 d/\alpha$ above which a *second* line of first order phase transitions with a critical point occurs. This line of phase transition may or may not meet the "normal" line of transition in a triple point; the higher $V_0 d/\alpha$ is, or the lower λ is, the less likely we are to observe a triple point.

All three possible phases seen in this model can only be described as fluid-like; as we noted in chapter 1, systems with translational order are unstable in one dimension. It is possible for such a potential to exhibit an extra fluid-fluid transition. Of course, and as we shall see, this does not mean that such potentials will definitely give fluid-fluid phase transitions in higher dimensions; it is merely that the "default" high density phase in one dimension is fluid, whereas in higher dimensions high density lattice phases become the norm.

Stell and Hemmer note in passing [45] that this model can exhibit "crossing isotherms" - that is, negative α_P, a liquid state anomaly as we described earlier for water - but they do not develop this further.

The unusual phase behaviour seen here is not a consequence of the exact form chosen for

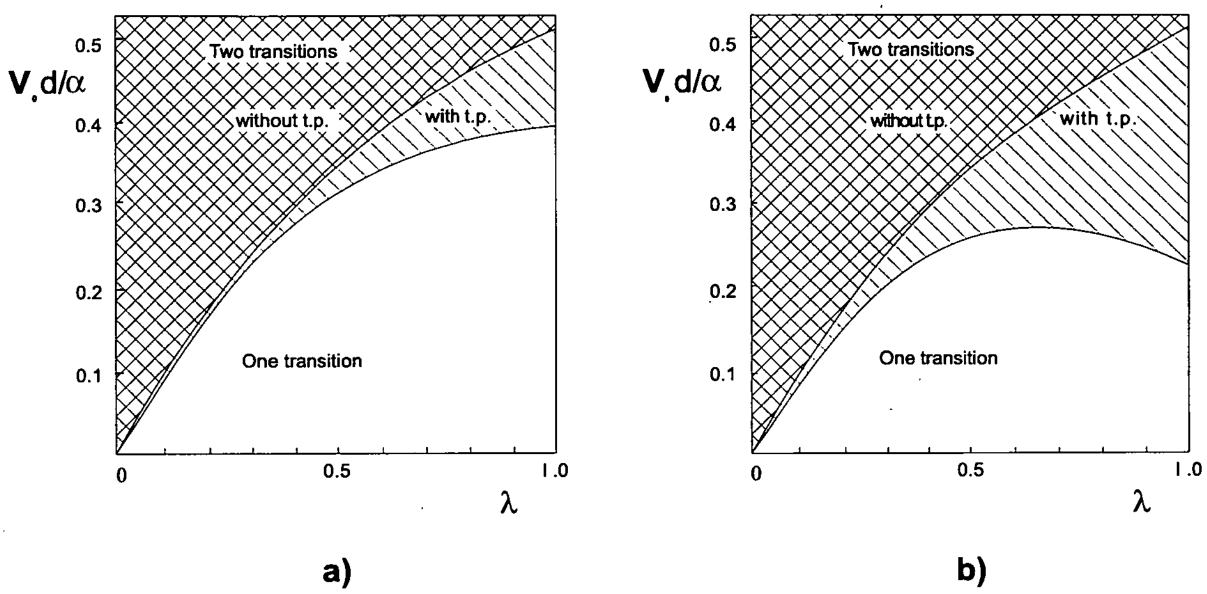

Figure 2.11: a) Characteristics of the phase diagram for a one dimensional system interacting via the potential given in equation 2.4.
b) Characteristics of the phase diagram for a one dimensional system interacting via the potential given in equation 2.6.
These diagrams are reproduced from reference [45]

equation 2.4; Stell and Hemmer also consider a potential of the form

$$\begin{aligned} \phi(r) &= \infty & & & r &< d \\ &= V_0 & d &< & r &< d(1+\lambda) \\ &= -\alpha\gamma e^{-\gamma r} & d(1+\lambda) &< & r & \end{aligned} \tag{2.6}$$

(see figure 2.10 b) which they treat in the same manner. This system gives qualitatively similar phase behaviour, as shown in figure 2.11 b. Further, none of the anomalous behaviour is due to the discontinuities within the interparticle potentials; as Stell and Hemmer point out, it is possible to construct continuous potentials arbitrarily close to those used here.

This work was followed by a series of papers examining the behaviour of the shouldered potential (given by equation 2.6) in higher dimensions. In reference [48], two complementary perturbation schemes are developed for the one dimensional system. Both calculate the free energy from the radial distribution function, $g(r)$. The shoulder height V_0 is taken as a perturbation parameter from a reference hard-sphere system of radial distribution function $g_{HS}(r)$.

The first scheme calculates expands $g(r; V_0)$ around V_0 such that:

$$g(r; v, V_0) = g_{HS}(r; v) + V_0 \left. \frac{\partial g}{\partial V_0} \right|_{V_0=0} + \dots \tag{2.7}$$

The authors note that the free energy calculated through this scheme is a rigorous upper bound to the "true" free energy though the Gibbs-Bogoliubov inequality; further, in one dimension it becomes exact in the limit of close packing.

The second scheme writes the radial distribution function as:

$$g(r; v, V_0) = e^{-\beta\phi(r,V_0)} y(r; v, V_0) \tag{2.8}$$

The function $y(r; v, V_0)$ is then expanded around $V_0 = 0$ such that:

$$g(r; v, V_0) = e^{-\beta\phi(r,V_0)} \left(y_{HS}(r; v) + V_0 \left. \frac{\partial y}{\delta V_0} \right|_{V_0=0} + \dots \right) \tag{2.9}$$

The authors note that this scheme appears to be a lower bound to the true free energy, though they are unable to show this rigorously; it further appears to become correct in the ideal gas limit.

These approximations are then extended to three dimensions [49], though there is no guarantee of rigour in this extension. Using the Weis and Percus-Yevick expressions for $g_{HS}(r)$, in three dimensions, and Hall and Alder-Hoover-Young expressions for the hard sphere solid free energy, and assuming the equilibrium crystal structure to be fcc, the authors find an isostructural solid-solid transition.

Similar results were found by Young [50], who used a Lennard-Jones-Devonshire cell model[4] to study the solid state phase diagrams for several potentials, including a shouldered square well potential (see figure 2.12 b) . This work takes into account several crystal lattices, including bcc and simple cubic, and finds results for the shouldered square well which qualitatively reproduce the experimental phase diagram for Cerium.

Since these first papers, there has been a great deal of research on the behaviour of core-softened potentials. Some has focused on their solid phase behaviour, whilst the possibility of a fluid-fluid transition in water has kindled a great deal of interest in their fluid phase behaviour.

---

[4] Lennard-Jones-Devonshire cell theory was originally developed as a mean-field lattice theory of the liquid state, though can be better interpreted as a theory of the solid state, conceptually sitting somewhere between the simple Einstein crystal and the harmonic approximation. See chapter 5 and [2] for a full discussion.

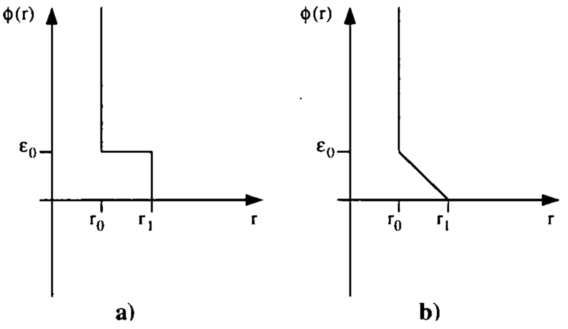

Figure 2.12: a) Simple shouldered hard-sphere core-softened potential.
b) Simple ramped core-softened potential.

We shall now review this body of work.

2.2.3 Solid State Phase Behaviour of Core-Softened Potentials

Two Dimensions

Two dimensional systems hold a certain degree of appeal for theoretical work. Whilst it is not possible to produce exact results as it is for many one-dimensional systems, two dimensional systems are sometimes more tractable than their three-dimensional counterparts. They are also often taken as qualitatively more similar to three dimensional systems than one dimensional systems are. There are still caveats (the largest being the instability of lattice phases in the infinite limit, and the possibility of continuous melting), but this field of study is still worthwhile.

In three dimensions, and for spherically-symmetric phases, the fcc lattice is, in general, the most stable lattice for a one-component crystalline phase. Researchers willing to go further than assuming fcc will often only go so far as to check for other possible close-packed lattices (and possibly simple cubic), unless some external evidence compels them to examine other lattices. In two dimensions, triangular lattice phases are the norm, and anything more exotic the exception.

Work by Jagla [51] has shown that a simple core-softened potential can produce a whole menagerie of possible lattice phases in two dimensions, even in the ground state (that is, $T = 0$).

The potential studied was a hard core with linear ramp (see figure 2.12 b), given by:

$$\begin{array}{rcl}\phi & = & \infty \qquad\qquad\qquad r < r_0 \\ & = & \varepsilon_0 \frac{r_1 - r}{r_1 - r_0} \qquad r_0 < r < r_1 \\ & = & 0 \qquad\qquad\quad r_1 < r\end{array} \tag{2.10}$$

Jagla uses ground state calculation to find which phases will be stable at zero temperature. A number of possible lattices are proposed, and their configurational energy as a function of volume, $e(v)$, are calculated; from this, their enthalpies h (equivalent to the Gibbs free energy at zero temperature) can easily be found, and their relative thermodynamic stabilities checked. The results (calculated for a range of the potential parameter, r_0/r_1) are surprising. Eight possible lattice phases are found. Two of these are triangular, corresponding to an interparticle separation of either the hard sphere diameter or the ramp diameter. A square and rhombic lattice are found, which are both normally unstable against shear deformations which would lead to collapse into a triangular structure. Other structures involve unit cells with more than one particle. Strangest of all is a ground-state quasicrystal, stable only at one distinct point of pressure and r_0/r_1.

The full (P, T) phase diagram for an example of this system was then calculated using a combination of Monte Carlo simulation and thermodynamic integration; this exhibits six separate lattice phases, including a region of entropically stabilised quasicrystal. The system exhibits three separate melting point maxima, and a density anomaly in its fluid phase[5].

This two dimensional linear-ramped potential system does not appear to exhibit a stable isostructural solid-solid transition. This does not discount the possibility that such a transition may exist, but is preempted by thermodynamically more stable lattices, and as such occurs between metastable phases.

At this point, a major caveat on isostructural solid-solid critical points must be made. It has already been pointed out that there exists an extra possible phase in two dimensions, the hexatic, lacking in any translational order but retaining orientational order. Though normally considered as a phenomenon of melting, a two-dimensional lattice phase will lose stability to a hexatic phase when the Kosterlitz-Thouless elastic constant C_{K-T} falls below a particular

---

[5] Since the potential lacks any attractive part, it does not show a liquid-gas transition.

value, $C_{K-T} \leq 16\pi$. We rewrite this constant in terms of the isothermal compressibility:

$$C_{K-T} = \frac{4\mu}{K_T\left(\mu + K_T^{-1}\right)} \tag{2.11}$$

Close to a critical point, critical fluctuations can make the bulk modulus arbitrarily small. Since these same fluctuations will have little effect upon the shear modulus μ, we should expect that, upon approach to an isostructural critical point, a two-dimensional system will pass through a second-order transition into an island of hexatic phase as the critical fluctuations make isothermal compressibility arbitrarily large [52]. Following on from these arguments, Bladon and Frenkel [52] have observed exactly this, and their results have been confirmed by further investigation [53]. This makes it unlikely that a stable isostructural solid-solid critical point in two dimensions could be directly observed.

Three Dimensions

It will be instructive at this point to consider work by Bolhuis, Frenkel and Hagen [54, 55]. Though not directly concerning core-softened potentials, it has strong implications for work on isostructural transitions. These authors have considered the phase behaviour of the simple square well potential, given by:

$$\begin{aligned} \phi(r) &= \infty & & & r &< \sigma \\ &= -\varepsilon & \sigma &< & r &< \sigma + \delta \\ &= 0 & \sigma + \delta &< & r & \end{aligned} \tag{2.12}$$

This potential is often used as a simple model for interactions between uncharged colloidal particles. It is known from experimental, theoretical and simulation work that simple attractive potentials will exhibit a liquid-gas type transition as long as δ/σ is large enough. Below a particular value, however , the liquid-gas critical temperature will drop below the melting curve; the condensation transition will be preempted by freezing, and the liquid-gas transition will become metastable with respect to the solid phase.

Bolhuis and Frenkel studied the phase behaviour for this system when δ becomes very small compared to σ (that is, with no stable liquid-gas transition), using a combination of Monte Carlo simulations and thermodynamic integration from the hard-sphere system. It was assumed that the stable lattice phase was either triangular or fcc, depending upon the dimension. They found that, for $\delta/\sigma < 0.07$, the system exhibits an isostructural fcc – fcc or triangular-triangular transition in three and two dimensions, respectively. For values of $\delta/\sigma \geq 0.07$, this isostructural transition is preempted by melting, becoming metastable.

This isostructural transition does not occur through the mechanisms we have mentioned above, being entropically driven, but such behaviour from such a simple potential is certainly interesting. With the potential so short-ranged, the liquid-gas transition has long sunk into metastability behind the solid phase, to a point at which it is effectively unobservable. As we raise the parameter δ, the potential becomes longer-ranged, and the position of the isostructural transition line moves up in volume and temperature until it becomes metastable with respect to the liquid phase. If we raise δ further, the liquid-gas transition will rise out of metastability and become part of the equilibrium phase diagram, whilst the isostructural transition will disappear back to unreasonably high free energies, before disappearing altogether. This behaviour is not some artifact of the square well potential; it has also been shown for the hard core attractive Yukawa potential [55]. This raises questions as to whether the liquid-gas transitions in other systems have isostructural "shadow" transitions between metastable solid phases; further, as to whether isostructural transitions have metastable fluid-fluid shadows.

Following this work, Bolhuis and Frenkel [56] have studied the phase diagram for a core-softened potential, the shouldered hard sphere, given by:

$$\begin{aligned} \phi(r) &= \infty & & r < \sigma \\ &= \varepsilon_0 & \sigma < {} & r < \sigma(1+\delta) \\ &= 0 & \sigma(1+\delta) < {} & r \end{aligned} \qquad (2.13)$$

This potential was studied using a combination of Monte Carlo simulations and thermodynamic integration, once again only considering the fcc lattice. They find that this system does appear to exhibit an isostructural fcc – fcc transition for a range of shoulder widths out to $\delta \approx 0.25$. This study was taken further by Rascon, et al [57]. These authors used a density functional perturbation theory to study the same system, but also considered bcc and sc lattices. Their results give quite reasonable agreement with Bolhuis and Frenkel's simulation data [56]. They suggest that, as the width δ of the shoulder rises, the bcc phase becomes stable at increasingly high temperatures, until by $\delta \doteq 0.16$ it has preempted the fcc – fcc transition altogether. For potentials with such wide shoulders, there will be one fcc phase with a

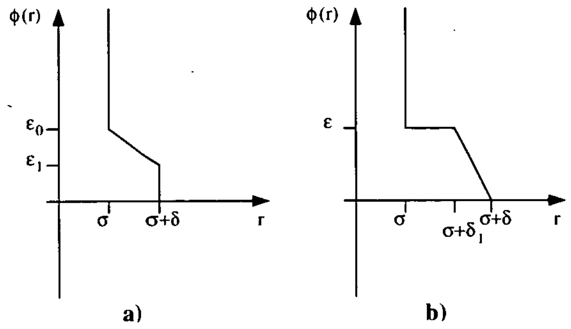

Figure 2.13: Core-softened potentials studied in reference [59].

low-temperature region of stable bcc phase, with the isostructural transition between phases metastable behind the bcc phase. This result is very similar to the interceding phases found by Jagla [58] in two dimensions. The authors also examined the phase behaviour for the repulsive Yukawa potential, given by:

$$\phi(r) = \frac{\lambda\sigma}{r} e^{-\kappa(r-\sigma)} \tag{2.14}$$

It will immediately be noticed that this potential does not satisfy the conditions for core-softening, being a monotonically decreasing function of the particle separation r. The authors note that their perturbation scheme gives poor quantitative results for this potential, though they believe their results to be qualitatively correct. Their results show a stable region of bcc phase, with no possibility of isostructural transition.

The same density functional perturbation scheme has been used by Velasco, et al [59] to study two core-softened potentials, both modifications of the shouldered hard sphere potential. Both modifications are shown in figure 2.13.

Both modifications show a low-temperature bcc region, with fcc becoming the stable phase at higher temperature. Interestingly, isostructural transitions can be found in *both* fcc and bcc lattices for both modifications; at low temperatures, the bcc phase overlays the fcc transition, such that there can exist an fcc – bcc – fcc triple point. In the range of potential parameter $\varepsilon_1/\varepsilon_0$ studied for the first modification (figure 2.13 a), the bcc – bcc transition ends in a critical point within the stable bcc range. Both fcc – fcc and bcc – bcc critical points recede in temperature with decreasing $\varepsilon_1/\varepsilon_0$, until the fcc – fcc transition recedes completely behind the bcc region, as has been discussed above. Velasco, et al, have calculated the value of the potential parameter such that the fcc – fcc critical point lies exactly on the fcc – bcc transition line - this gives rise to a novel form of triple point, between the bcc phase and two fcc phases of equal density.

For the second modification (figure 2.13 b), the chosen potential parameter is δ_1 (see figure 2.13 b). Here, the bcc – bcc transition extends beyond the bcc stability region, such that the bcc – bcc critical point is metastable with respect to the fcc lattice. As δ_1 increases, the fcc – fcc critical temperature increases, whilst its pressure falls; it is expected that with increasing δ_1, the fcc – fcc transition will disappear behind the liquid phase.

Considering this, and the work of Bolhuis and Frenkel [54, 55], we can make an interesting speculation. We have seen how, for the square well potential, there exist two isostructural transitions, the standard liquid-gas transition and an fcc – fcc transition. Depending upon the well width, only one is stable, the other being metastable, deep behind the other structure. Velasco's work [59] shows an isostructural transition in both the fcc phase and the bcc phase. It is possible to suggest that every "kink" in the free energy curve puts an isostructural transition into *every* possible structure for the system (each lattice, and also amorphous and fluid structures), but that these transitions are not normally observable, due to being either metastable with respect to other structures, or existing only as an analytic continuation off into regions where the structure is fully unstable.

These works have only considered the normal cubic lattices (that is, fcc, bcc and sc). We saw earlier how core-softened potentials can stabilise all kinds of exotic lattice phases in two dimensions, and this may be true in three dimensions, too. Jagla [58] has attempted to calculate the stable ground-state lattices for the linear ramp potential (equation 2.10, see figure 2.12 b). Once again, this has been done by proposing a set of possible lattice phases; the chosen set included not just the normal cubic lattices (sc, bcc and fcc), but also tetragonal, hcp, rhombohedral and hexagonal. All these lattices are found to have a stable region across the range of pressure and potential parameter examined; further, there exist areas in the phase diagram across which none of these structures were found to be mechanically stable, hence where the stable lattice must be outside of this set. To actually map the stability for many lattices across any reasonable range of the phase diagram would be an incredible job of work, even when confined to these high-symmetry lattices. It is possible that even more bizarre phases may be stabilised by core-softening. Work on atomic pseudopotentials for Cesium by Reed and Ackland [60] gives effective interparticle potentials which exhibit core-softening - it may be

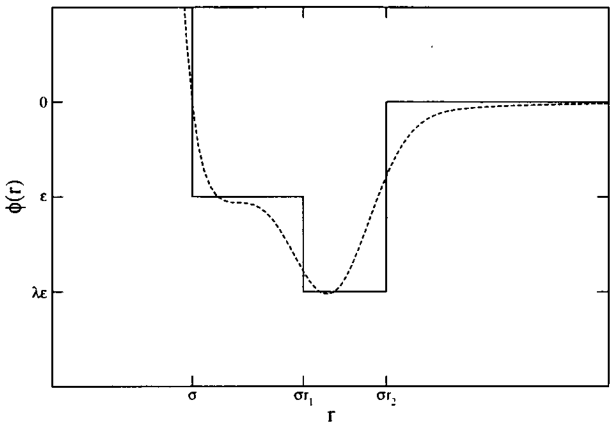

Figure 2.14: Potentials used in references [1, 61, 62].

interesting to investigate whether such potentials can give rise to large supercell structures similar to that speculated for the Cesium III phase [41].

2.2.4 Liquid State Phase Behaviour of Core-Softened Potentials

The current controversy over the second critical point hypothesis for water has sparked a great deal of investigation, both through theoretical approximations and direct simulation, into fluid systems which may demonstrate liquid state anomalies and/or liquid-liquid transitions. Here we will only be concerned with those investigations which have studied continuum core-softened systems.

Sadr-Lahijany et al [1, 61, 62] have studied the liquid phase behaviour in two dimensions resulting from two interaction potentials. The first of these is a combination of a 12-6 Lennard-Jones potential with a Gaussian well, given by:

$$\phi(r) = 4\varepsilon\left(\left(\frac{\sigma}{r}\right)^{12} - \left(\frac{\sigma}{r}\right)^{6}\right) - \lambda\varepsilon e^{-\left(w\left(\frac{r-r_0}{\sigma}\right)\right)^2} \tag{2.15}$$

Sadr-Lahijany et al [1, 61, 62] also study a discretised version of this potential, composed of

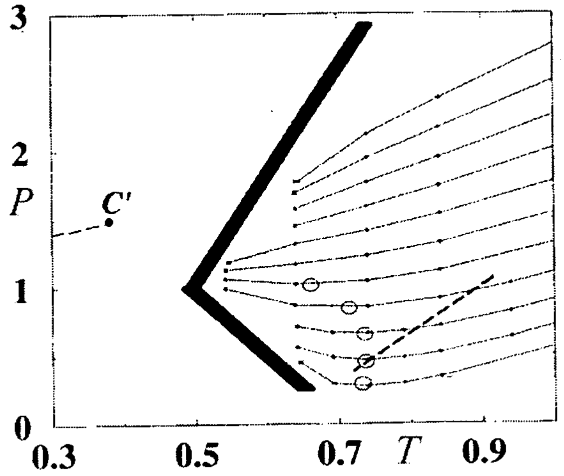

Figure 2.15: Phase diagram for potential given by equation 2.15, reproduced from [1]. The thick line shows the estimated melting curve, open circles mark temperatures of maximum density, and the dashed line marks temperatures of maximum compressibility. Curves mark lines of constant density. The point C' marks a critical point terminating a line of first order liquid-liquid transition estimated from cell theory.

two square wells, such that:

$$\begin{aligned} \phi(r) &= \infty & & r < \sigma \\ &= -\varepsilon & \sigma &< r < \sigma r_1 \\ &= -\lambda\varepsilon & \sigma r_1 &< r < \sigma r_2 \\ &= 0 & \sigma r_2 &< r \end{aligned} \tag{2.16}$$

The parameters studied were $\lambda = 1.7$, $r_0 = 1.5$ and $w = 5.0$ for the continuous potential, and $r_1 = 1.4$, $r_2 = 1.7$ and $\lambda = 2$ for the discrete potential - see figure 2.14. No motivation is stated for this choice of parameters. After confirming that the continuous potential could indeed give rise to density and compressibility anomalies in one dimension, they performed molecular dynamics simulations on a two-dimensional system using both potentials. The results for both potentials are described as being qualitatively similar [1]. These results show liquid state anomalies in density, compressibility, and diffusion, and two distinct solid phases (with the melting curves determined by the points where the diffusion coefficients vanish). At high pressures, the system freezes into a square lattice solid, whilst at low temperatures, the solid form is a triangular lattice. This triangular lattice has lower density than the liquid phase at the melting temperature, and therefore through the Clausius-Clapeyron equation has negative slope.

The presence of structural competition was investigated through study of the radial distribution function of the liquid, $g(r)$. This function shows a split in the first peak, indicating two preferred nearest-neighbour separations. The relative weights of the two sub-peaks change with applied pressure, indicating competition between open and closed structures, accounting for the anomalies. No full liquid-liquid transition was directly observed in these simulations. However, the authors fitted their compressibility data to power law divergences, and from this inferred the existence of a metastable liquid-liquid critical point behind one of the solid phases. They supported this hypothesis with calculations from a modified Lennard-Jones-Devonshire cell theory. Their reported phase diagram is shown in figure 2.15.

The first observation of a liquid-liquid transition from a core-softened potential has come from very recent work by Malescio and Pellicane [63]. These authors consider a combined shouldered hard sphere and square-well potential, given by:

$$\begin{array}{rclrcrcl} \phi(r) & = & \infty & & & r & < & \sigma \\ & = & \varepsilon & \sigma & < & r & < & \sigma r_1 \\ & = & -\lambda\varepsilon & \sigma r_1 & < & r & < & \sigma r_2 \\ & = & 0 & \sigma r_2 & < & r & & \end{array} \tag{2.17}$$

This potential, using parameters $r_1 = 2.5$, $r_2 = 3.0$ and $\lambda = 1.25$, was studied in three dimensions using thermodynamically self-consistent integral equations to approximate the equation of state, specifically, a combination of hypernetted chain and soft mean spherical approximation equations (see references within [63]). Once again, the authors do not motivate their choice of parameters. Their results show two transition lines and critical points, one the common or garden gas-liquid transition, the other a liquid-liquid transition. The authors estimate that this second transition lies between phases metastable with respect to the solid phase (estimated using the empirical Hansen-Verlet rule[6]); Monte Carlo simulations performed at state points near the purported second transition show no evidence of lattice structure, evidence that the metastable liquid states around the transition have appreciable lifespans.

Further work on this potential [64, 65] has been performed using parameters $r_1 = 2.0$,

---

[6] "Crystallisation occurs when the height of the first (main) peak of [the structure factor] $S(k)$ attains the value 2.85" [63]

$r_2 = 2.2$, $\lambda = 2$. These parameters have been chosen by calculating liquid equations of state through the procedures mentioned above, to find values which appear most likely to give a liquid-liquid phase transition. Molecular dynamics simulations are used to directly observe the transitions once parameters have been established. The liquid-state approximations are quoted as showing good qualitative agreement with the simulation results. The simulations show both transitions as metastable with respect to the solid phase, with their positions sensitive to the potential parameters. Increase in width of the attractive well increases both critical temperatures, whilst increase in λ or decrease in r_1 the temperature of the liquid-liquid critical point is lowered with respect to the liquid-gas critical temperature.

This model has one final important feature; it shows no density anomaly in the fluid phase.

The other core-softened potential known to demonstrate a liquid-liquid transition is a version of the linear ramp potential, due to Jagla [66]. This potential is given by:

$$\begin{aligned} \phi(r) &= \infty & r &< r_0 \\ &= \varepsilon\left(\frac{r_1-r}{r_1-r_0} - \lambda\frac{r_2-r}{r_2-r_0}\right) & r_0 < r &< r_1 \\ &= -\varepsilon\lambda\frac{r_2-r}{r_2-r_0} & r_1 < r &< r_2 \\ &= 0 & r_2 &< r \end{aligned} \tag{2.18}$$

Systems interacting via this potential have been shown to have extra liquid-liquid transitions and critical points in both two and three dimensions, using direct Monte Carlo simulation. In two dimensions, Jagla shows the liquid-liquid transition to occur between stable phases, with the transition line reaching a triangular-liquid-liquid triple point at low temperatures; this triangular lattice is less dense than either liquid phase, and so has a melting curve of negative slope. In three dimensions, the transition also appears to be stable, with none of the simulations performed showing evidence of a solid phase. Both two and three dimensional +systems show liquid state anomalies.

2.3 Summary

We have seen that simple core-softened potentials can mimic the phase behaviour of several unusual, and apparently disparate real systems. On the one hand, these potentials can give rise to the unusual liquid phase behaviour seen in a variety of tetrahedrally coordinated systems, including water, Si, Ge, SiO_2, and GeO_2, and to a certain extent carbon and phosphorus. The real interaction potentials for such systems are complex and strongly anisotropic, making accurate modelling difficult. Similarly, core-softened potentials can exhibit the unusual solid phase behaviour of the metal Ce. We have distilled these features down to one essential property of the interaction potential; the presence of two distinct particle separations, selected between by pressure. As such, these potentials are extremely relevant to the understanding and development of experimental work in several areas of ongoing research.

The exotic and varied phase diagrams that such potentials give us access to suggest that these potentials may facilitate study of several other phenomena. By inducing a critical point in a two dimensional solid phase, we can induce a surrounding area of hexatic phase stability; hexatic phases are notoriously difficult to cause and to pin down, and so core-softened potentials could aid in their study. The richness of phases shown by core-softened systems could hold other such surprises, such as stable quasi-crystals. Further, many of the features attracting study to these potentials regularly occur in metastable phases; these may lead to better methods for artificially altering the relative stability of phases in simulation work.

Finally, these potentials could be of great interest at a more basic level of condensed matter theory; they may help to give a better understanding of how shape of potential influences phase and state behaviour. We have seen suggestions that transitions within phases (such as the liquid-gas transition) may have corresponding “shadow” transitions in other phases, raising interesting questions as to how the free energy landscape of lattice and fluid phases reflect and affect each other. Apparently similar potentials give transitions with liquid state anomalies, or phase diagrams where such anomalies are completely absent. In summary, core-softened potentials offer a rich seam of potential research, which should be of interest in terms of theory, simulation, and experiment alike.

2.4 Research Aims

In this work, we intend to follow up on the work of Sadr-Lahijany et al [1], making an extended study of the phase behaviour of a two-dimensional system of particles interacting via the core-softened potential given in equation 2.15. We will investigate the origin of the liquid state anomalies in the system, particularly with respect to whether they are the result of structural competition which may give rise to liquid-liquid phase separation at sufficiently low temperature. We will also study the solid state phase behaviour, checking for the possibility of solid-solid isostructural transitions and any relation to the liquid state phase behaviour. Finally, we shall investigate the liquid state behaviour of the system in three dimensions, checking for liquid state anomalies and evidence of liquid-liquid transitions. Through this study, we hope to gain insight into the behaviour of this particular model, and through that insight, learn more about the phase behaviour of core-softened potentials in general.

Chapter 3

Analytical Results in 1D

Before we start examining the Sadr-Lahijany system, we will take a look at the much simpler example of a core-softened system in one dimension. Whereas continuum systems in two and higher dimensions are often analytically intractable, exact solutions exist for several classes of simple one dimensional systems. The study of such a solution for a core-softened system should allow us to get a "feel" for the behaviour of core-softened systems in higher dimensions. Of course, one dimensional systems also lack many of the features seen in higher dimensions; as such, the work presented here should be seen as an instructive example.

3.1 The Takahashi Nearest-Neighbour Gas

We will use this elegant method, which allows for the exact treatment of one dimensional systems of particles, provided that only particles which are nearest neighbours interact[1]. The method was originally developed by Takahashi [46] (and independently by Gursey [67]) as a generalisation of the "Tonks gas" one dimensional hard rod system [68].

We start with the configurational integral for our one-dimensional system at constant pressure, given by:

$$Z = \int \underset{x_0<x_1<\ldots<x_n}{\cdots\cdots\cdots} \int e^{-\beta \sum_{i=1}^{i=n} \phi(x_i - x_{i-1})} e^{-\beta P \sum_{i=1}^{i=n} (x_i - x_{i-1})} dx_1 \ldots dx_n \tag{3.1}$$

---

[1] An example of such an interaction is an interparticle potential with a hard core and no interaction beyond twice the hard core radius.

where x_i is the coordinate of the ith particle, P is the applied pressure, and $\phi(r)$ is the potential acting between particles separated by r. The total volume of this system is given by $L = x_n - x_0$.

We rephrase equation 3.1 such that:

$$r_i = x_i - x_{i-1} \tag{3.2}$$

and observe that

$$\frac{\partial\left(x_1, x_2, \ldots, x_n\right)}{\partial\left(r_1, r_2, \ldots, r_n\right)} = 1 \tag{3.3}$$

This allows us to write equation 3.1 in the following form:

$$\begin{aligned} Z &= \int\int_{r_1,r_2,\ldots,r_n>0}\int e^{-\beta\left(\sum_{i=1}^{i=n}\phi(r_i)+P\sum_{i=1}^{i=n}r_i\right)}dr_1...dr_n \\ &= \int\int_{r_1,r_2,\ldots,r_n>0}\int\prod_{i=1}^{i=n}e^{-\beta(\phi(r_i)+Pr_i)}dr_1...dr_n \\ &= \left(\int_0^\infty e^{-\beta(\phi(r)+Pr)}dr\right)^n \end{aligned} \tag{3.4}$$

This simple equation is equivalent to the partition function of a chain of n non-interacting spin sites, each of which can take spin values $r = 0..\infty$, have an internal energy dependent upon their spin $\phi(r)$, and are acted upon by an external field P which decreases the energy of each spin site by Pr. These spins correspond to the interparticle separations, hence we have the partition function of n spin sites corresponding to the partition function of $n + 1$ particles.

Now that we have the configurational part of the partition function, we can easily calculate the corresponding thermodynamic potential, in this case the Gibbs free energy:

$$\begin{aligned} G &= -\frac{1}{\beta}\log\left(\frac{Z}{\Lambda^n}\right) \\ &= -\frac{n}{\beta}\log\left(\frac{\int_0^\infty e^{-\beta(\phi(r)+Pr)}dr}{\Lambda}\right) \end{aligned} \tag{3.5}$$

with Λ as the thermal de Broglie wavelength - this merely adds a constant contribution to the free energy, and is taken as unity through convenient choice of units.

Knowing the free energy, it is possible to calculate all thermodynamic quantities of the system, for instance the average interatomic distance:

$$\begin{aligned} l &= \frac{1}{n}\left[\frac{\partial G}{\partial P}\right]_T \\ &= -\frac{\frac{\partial}{\partial P}\left(\int_0^\infty e^{-\beta(\phi(r)+Pr)}dr\right)}{\beta\int_0^\infty e^{-\beta(\phi(r)+Pr)}dr} \\ &= \frac{\int_0^\infty re^{-\beta(\phi(r)+Pr)}dr}{\int_0^\infty e^{-\beta(\phi(r)+Pr)}dr} \end{aligned} \tag{3.6}$$

showing that, for a nearest-neighbour interaction 1D system, the interparticle separation is equal to the average atomic distance for a system of only two particles interacting via a potential $\phi(r)$ and subject to a pressure P. We also note that, since $\phi(r)$ will be a single-valued function of r, average interatomic distance l must be a single-valued function of P - there can be no true phase transitions at non-zero temperature for the Takahashi gas[2].

3.2 The 1D Hard Rod System

We will now demonstrate Takahashi's model with the one-dimensional equivalent of hard spheres - the simple hard rod potential, given by:

$$\phi = \begin{cases} \infty & r < \sigma \\ 0 & r > \sigma \end{cases} \tag{3.7}$$

We first calculate the configurational integral for this system:

$$\begin{aligned} \int_0^\infty e^{-\beta(\phi(r)+Pr)}dr &= \int_0^\sigma e^{-\beta Pr}e^{-\infty}dr + \int_\sigma^\infty e^{-\beta Pr}e^{-0}dr \\ &= 0 - \frac{1}{\beta P}\left[e^{-\beta Pr}\right]_{r=\sigma}^{r=\infty} \\ &= \frac{e^{-\beta P\sigma}}{\beta P} \end{aligned} \tag{3.8}$$

which gives the free energy for a 1D hard-sphere system:

$$\begin{aligned} G &= nP\sigma + \frac{n\log(\beta P)}{\beta} + \frac{n}{\beta}\log\Lambda \\ &\equiv ng \\ g &= P\sigma + \frac{\log(\beta P)}{\beta} + \frac{1}{\beta}\log\Lambda \end{aligned} \tag{3.9}$$

with g as the intensive Gibbs free energy per particle.

Applying equation 3.6 gives us :

$$l - \sigma = \frac{1}{\beta P} \tag{3.10}$$

which is the correct equation of state for the 1D hard sphere system [68], and is continuous and

---

[2] Indeed, it has long been suggested that there cannot be a phase transition at non-zero temperature for *any* one dimensional model interacting via a finite-ranged potential, though no general proof of this exists [69].

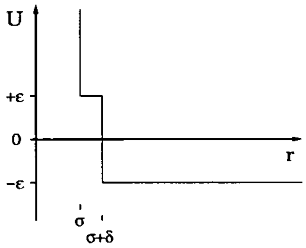

Figure 3.1: Shouldered hard rod/sphere potential

single valued for all $T \geq 0$ and positive P.

3.3 The Shouldered Hard Rod System

We will now use Takahashi's model to study a very simple core-softened potential; a hard rod potential with a shoulder, as shown in figure 3.1:

$$\phi = \begin{cases} \infty & 0 < r < \sigma \\ \epsilon & \sigma < r < \sigma(1+\delta) \\ -\epsilon & \sigma(1+\delta) < r < \infty \end{cases} \tag{3.11}$$

Calculating the configurational integral gives us:

$$\begin{aligned} \int_0^\infty e^{-\beta(U(r)+Pr)}dr &= \int_0^\sigma e^{-\beta Pr}e^{-\infty}dr + \int_\sigma^{\sigma(1+\delta)} e^{-\beta Pr}e^{-\beta\epsilon}dr + \int_{\sigma(1+\delta)}^\infty e^{-\beta Pr}e^{\beta\epsilon}dr \\ &= 0 - \tfrac{1}{\beta P}\left(e^{-\beta\epsilon}\left[e^{-\beta Pr}\right]_{r=\sigma}^{r=\sigma(1+\delta)} + e^{\beta\epsilon}\left[e^{-\beta Pr}\right]_{r=\sigma(1+\delta)}^{r=\infty}\right) \\ &= -\tfrac{e^{-\beta P\sigma}}{\beta P}\left(e^{-\beta\epsilon}e^{-\beta P\delta\sigma} - e^{-\beta\epsilon} - e^{\beta\epsilon}e^{-\beta P\delta\sigma}\right) \\ &= \frac{e^{-\beta P\sigma}e^{-\beta\frac{P\delta\sigma}{2}}}{\beta P}\left(\left(e^{-\beta\epsilon}e^{\beta\frac{P\delta\sigma}{2}} + e^{\beta\epsilon}e^{-\beta\frac{P\delta\sigma}{2}}\right) - e^{-\beta\epsilon}e^{-\beta\frac{P\delta\sigma}{2}}\right) \\ &= \frac{e^{-\beta P\sigma\left(1+\frac{\delta}{2}\right)}}{\beta P}\left(2\cosh\left(\beta\left(\epsilon - \tfrac{P\delta\sigma}{2}\right)\right) - e^{-\beta\left(\epsilon+\frac{P\delta\sigma}{2}\right)}\right) \end{aligned} \tag{3.12}$$

Let us now move to the reduced units $\beta^*$and P^*:

$$\beta^* = \beta\epsilon \qquad P^* = \tfrac{\sigma\delta}{2\epsilon}P \tag{3.13}$$

giving the configurational integral as:

$$\int_0^\infty e^{-\beta(U(r)+Pr)}dr = \frac{2}{\sigma\delta}\frac{e^{-\beta^* P^*\left(1+\frac{2}{\delta}\right)}}{\beta^* P^*}\left(2\cosh\left(\beta^*\left(1-P^*\right)\right) - e^{-\beta^*\left(1+P^*\right)}\right) \tag{3.14}$$

The reduced Gibbs free energy per particle is therefore:

$$g^* = \frac{g}{\epsilon}$$

$$g^* = P^*\left(1+\frac{2}{\delta}\right) - \frac{1}{\beta^*}\log\left(\frac{1}{\beta^* P^*}\frac{2}{\Lambda\sigma\delta}\right) - \frac{1}{\beta^*}\log\left[2\cosh\left(\beta^*\left(1-P^*\right)\right) - e^{-\beta^*\left(1+P^*\right)}\right] \tag{3.15}$$

The equation of state is:

$$\frac{2}{\sigma\delta}(l-\sigma) = \frac{1}{\beta^* P^*} + 1 + \frac{2\sinh\left(\beta^*\left(1-P^*\right)\right) - e^{-\beta^*\left(1+P^*\right)}}{2\cosh\left(\beta^*\left(1-P^*\right)\right) - e^{-\beta^*\left(1+P^*\right)}} \tag{3.16}$$

We know that this system can exhibit no phase transition at $T > 0$, so we will examine the zero temperature limits:

$$\lim_{\beta^*\to\infty} g^* = P^*\left(1+\frac{2}{\delta}\right) + \frac{1}{\beta^*}\log\left[e^{\beta^*\left(1-P^*\right)} + e^{-\beta^*\left(1-P^*\right)}\right] \tag{3.17}$$

$$\lim_{\beta^*\to\infty}\frac{2}{\sigma\delta}(l-\sigma) = 1 + \frac{e^{\beta^*\left(1-P^*\right)} - e^{-\beta^*\left(1-P^*\right)}}{e^{\beta^*\left(1-P^*\right)} + e^{-\beta^*\left(1-P^*\right)}} \tag{3.18}$$

There are two possible limits here; one, at $P^* > 1$, where the $e^{\beta^*\left(1-P^*\right)}$ terms go to zero, and the other at $P^* < 1$, where the $e^{-\beta^*\left(1-P^*\right)}$ terms go to zero. As such, the zero temperature behaviour is given by:

$$\begin{array}{llcc} P^* < 1 & \lim_{\beta^*\to\infty} g^* & = & \frac{2}{\delta}P^*(1+\delta) - 1 \\ & \lim_{\beta^*\to\infty}(l-\sigma) & = & \sigma\delta \\ P^* > 1 & \lim_{\beta\to\infty} g^* & = & \frac{2}{\delta}P^* + 1 \\ & \lim_{\beta\to\infty}(l-\sigma) & = & 0 \end{array} \tag{3.19}$$

The zero temperature behaviour is shown in figure 3.2. We can see that there is a disconti-

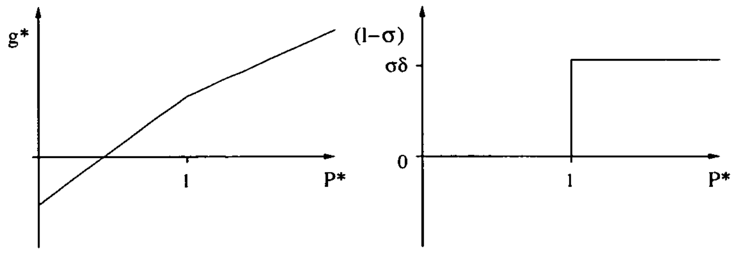

Figure 3.2: Gibbs free energy and equation of state for the shouldered hard rod system in the zero-temperature limit.

nuity in the derivative of the Gibbs free energy at $T^* = 0, P^* = 1$; that is, a first-order phase transition exists at this point. This is a transition between interparticle separations lying at the base of the shoulder ($l = \sigma(1+\delta)$) at low pressure ($P^* < 1$) and interparticle separations lying at the hard-core radius ($l = \sigma$) at high pressure ($P^* > 1$). At non-zero temperature, thermal disorder smooths out this transition; at least one particle will have enough energy to overcome (at $P^* > 1$) the applied pressure or (at $P^* < 1$) the shoulder repulsion of a neighbour, making l a continuous function of P.

3.3.1 Liquid State Anomalies

We have now shown that softening the hard rod potential with a shoulder introduces a zero-temperature transition in this system. We will now investigate whether core-softening in this simple system will give rise to anomalous behaviour in density and compressibility.

Density Behaviour

The derivative of l (the equivalent to v in this system) with respect to T for the shouldered hard sphere potential is given by:

$$\frac{2}{\sigma\delta}\frac{\partial l}{\partial T^*}\bigg|_P = \left(\frac{1}{P^*} - \left(\frac{4\beta^{*2}\left(1 - P^* + P^* e^{-2\beta^*}\right)}{\left(2\cosh\left(\beta^*\left(1-P^*\right)\right) - e^{-\beta^*(1+P^*)}\right)^2}\right)\right) \tag{3.20}$$

Anomalous expansion upon cooling will occur when equation 3.20 is negative; it can be seen that this can never happen if $P^* > 1$. Density anomalies cannot occur at pressures greater than the transition temperature in this model.

Analytically solving $\frac{\partial l}{\partial T}_P = 0$ is very difficult for this system; it is easier to use numerical methods. This gives us a locus of temperatures of maximum density, shown in figure 3.3 for

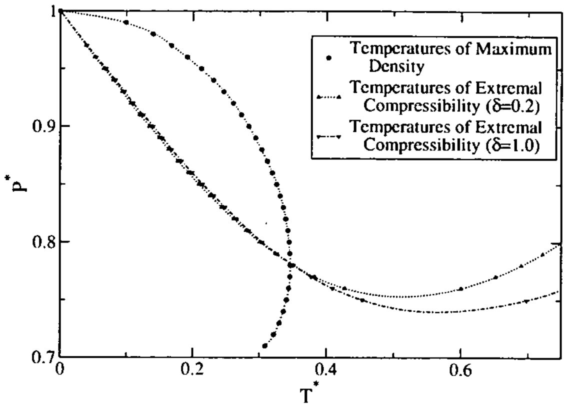

Figure 3.3: Liquid state anomalies numerically calculated for the potential 3.11. Temperatures of maximum density are independent of the detail of this potential, whilst temperatures of extremal compressibility are not; we show TEC lines calculated at $\delta = 0.2$ and $\delta = 1.0$. Lines serve as guides to the eye.

$\delta = 1.0$. We see a TMD curve which retraces in temperature at a pressure of $P^* = 0.757$, tending towards (though never reaching) $P^* = 1.0$ at $T^* = 0.0$. At pressures below $P^* = 0.694$, we see no further density anomalies - the TMD line ceases with an inflection in density at this pressure.

We now offer a physical explanation for this behaviour, in terms of structural competition. Consider the effect on the free energy from a particle moving up onto the shoulder of its neighbour; there is a deleterious positive contribution from an increase in configurational energy, but there is also a favourable negative contribution from decreasing volume, and also from increasing entropy (increasing the amount of configuration space explored). The balance between these contributions depends upon temperature and pressure. As temperature is decreased, the contribution of entropy to the free energy becomes less important; when temperature becomes low enough, configurational energy becomes the most important factor, and configurations in which particle separation is above the shoulder width come to dominate. This "switch over" leads to the density anomaly. With further decrease in temperature, most particles will not sample the shoulder, and the "normal" expansivity behaviour of these particles will overcome the anomalous structural competition contribution, leading to a return to normal density behaviour.

Now consider the pressure/volume behaviour. At high pressures (specifically, above the transition pressure at $P^* = 1$), the volume contribution to the free energy outweighs the configurational energy contribution; particles move onto the shoulder of their neighbours potentials with ease. In terms of structural competition, one structure completely dominates, and so there is no competition to cause the density anomaly. As we lower pressure, some particles move down off the shoulders; since there are few, there is only a slight configurational energy gain to the total free energy to move them back onto the shoulder, and so temperature must be very low to get the density anomaly. As pressure is lowered still further, the number of particles not sampling the shoulders increases, the configurational energy gain to the total free energy for moving them back up increases, and the temperature at which the density anomaly occurs increases.

Of course, this structural competition is only one contribution to the expansivity, $\frac{\partial l}{\partial T}\big|_P$. As we lower pressure still further, particles are sampling separations further and further from either the hard core distance or the shoulder, acting more like a hard rod gas. This adds a large positive contribution to the expansivity, which begins to overcome the signature of the structural competition. This causes the TMD line to curve back towards the pressure axis, at first retracing, then, at low enough pressure, disappearing entirely, swamped by the hard rod gas contribution.

We now consider the dependence of the TMD line on the only free parameter of the potential, δ. We observe that the contents of the brackets in equation 3.20 have no δ dependence, and so we can rewrite the expansivity as:

$$\left.\frac{\partial l}{\partial T^*}\right|_P = \frac{\delta}{2} f_1\left(\beta^*, P^*\right) \tag{3.21}$$

The δ dependence is given by:

$$\begin{aligned} \left.\frac{\partial^2 l}{\partial T^* \partial \delta}\right|_P &= \frac{1}{2} f_1\left(\beta^*, P^*\right) + \frac{\delta}{2}\frac{\partial f_1(\beta^*, P^*)}{\partial \delta} \\ &= \frac{1}{2} f_1\left(\beta^*, P^*\right) \end{aligned} \tag{3.22}$$

We are specifically considering the case $\frac{\partial l}{\partial T^*}\big|_P = 0$; since this requires $f_1\left(\beta^*, P^*\right) = 0$, we see from equation 3.21 that the TMD line is *independent* of δ. All dependence on this parameter has been subsumed into our choice of reduced units, specifically the reduced pressure P^*.

Compressibility Behaviour

We now turn to the behaviour of the isothermal compressibility, K_T. This is given by:

$$\begin{aligned} K_T &\equiv -\frac{1}{l}\frac{\partial l}{\partial P}_T \\ K_T &= \frac{1}{l}\left(\frac{1}{\beta^* P^{*2}} + 2\beta^* \frac{2-e^{-2\beta^*}}{\left(2\cosh(\beta^*(1-P^*))-e^{-\beta(1+P^*}\right)^2}\right) \end{aligned} \tag{3.23}$$

We are interested in the possibility of extrema in the compressibility, that is, points where $\frac{\partial K_T}{\partial T}|_P = 0$; unfortunately, the expression for this condition is even less tractable than the condition for the temperatures of maximum density. As such, we have found the TEC loci numerically for a variety of values of δ. Two typical curves are shown in figure 3.3.

We first examine their general behaviour. In all cases, the line of maximum compressibility originates at the zero temperature transition point, $P^* = 1$, where compressibility diverges. This line proceeds with negative slope, passing through the TMD line at the point where the latter has infinite slope (as thermodynamically required [21]). The slope of the line of compressibility maxima decreases with increasing temperature, until we reach a pressure below which there are no compressibility anomalies. At this point (an inflection in compressibility with respect to temperature), the line of maxima becomes a line of minima, with positive slope in the phase diagram, which continues with increasing temperature.

Once again, we make a physical explanation for this general behaviour. We initially consider the system at the transition pressure ($P^* = 1$). At very high temperatures, entropy favours particles exploring configurations both on and beyond the potential shoulder. Changes in pressure will create changes in volume in a "normal" manner; thus, compressibility behaves as normal. As we decrease temperature, however, the increase in favour to configurational energy considerations will cause some particles to drop down from the shoulder; an increase in pressure will cue some of these to move back up onto the shoulder. This creates an increase in compressibility with decreasing temperature; that is, compressibility passes through a minimum by decreasing temperature. As we decrease temperature still further, more particles will drop from the shoulder, so the increase in compressibility will continue, until finally diverging as we reach the transition point.

We now consider the system at a lower pressure. Upon cooling from a very high temperature, we will see the same compressibility behaviour; initial decrease with cooling, then passing through a minimum to anomalous increase with cooling via the same mechanism. However, upon reaching a low enough temperature, an infinitesimal increase in pressure is no longer enough to overcome the configurational energy bonus to falling from the shoulder; compressibility stops increasing, passing through a maximum and returning to normal behaviour. At low enough pressures this effect is strong enough that compressibility anomalies will never occur.

We now turn to the δ dependence of the compressibility lines in the same way as for the expansivity; that is, we rephrase equation 3.23 into a δ dependent part and a δ independent part, thus:

$$K_T = \frac{1}{l\left(\beta^*, P^*, \delta\right)} f_2\left(\beta^*, P^*\right) \tag{3.24}$$

We first consider the behaviour with respect to temperature:

$$\left.\frac{\partial K_T}{\partial T^*}\right|_P = \frac{1}{l}\left(\left.\frac{\partial f_2\left(\beta^*, P^*\right)}{\partial T}\right|_P - \frac{1}{l}\left.\frac{\partial l}{\partial T^*}\right|_P f_2\left(\beta^*, P^*\right)\right) \tag{3.25}$$

And now with respect to δ:

$$\begin{aligned} \left.\frac{\partial^2 K_T}{\partial T^* \partial \delta}\right|_P &= \frac{1}{l}\left(-\frac{\partial l}{\partial \delta}\frac{\partial K_T}{\partial T^*} + \frac{\partial^2 f_2(\ldots)}{\partial T^* \partial \delta} - \left(\frac{\partial l^{-1}}{\partial \delta}\left.\frac{\partial l}{\partial T^*}\right|_P f_2(\ldots) + \frac{1}{l}\left(\frac{\partial^2 l}{\partial T^* \partial \delta} f_2(\ldots) + \left.\frac{\partial l}{\partial T^*}\right|_P \frac{\partial f_2(\ldots)}{\partial \delta}\right)\right)\right) \\ &= \frac{1}{l}\left(-\frac{\partial l}{\partial \delta}\frac{\partial K_T}{\partial T^*} + \frac{1}{l^2} f_2(\ldots)\frac{\partial l}{\partial \delta}\left.\frac{\partial l}{\partial T}\right|_P - \frac{1}{l}\frac{\partial^2 l}{\partial T^* \partial \delta} f_2(\ldots)\right) \end{aligned} \tag{3.26}$$

where we have used the fact that all differentials of $f_2\left(\beta^*, P^*\right)$ are zero. We are concerned with the behaviour of the anomaly lines, that is, where $\left.\frac{\partial K_T}{\partial T^*}\right|_P = 0$; this allows us to simplify further, to:

$$\left.\frac{\partial^2 K_T}{\partial T^* \partial \delta}\right|_{P;TEC} = \frac{1}{l^2} f_2\left(\beta^*, P^*\right)\left(\frac{\partial l}{\partial \delta}\left.\frac{\partial l}{\partial T^*}\right|_P - \frac{\partial^2 l}{\partial T^* \partial \delta}\right) \tag{3.27}$$

Substituting in from equations 3.21 and 3.22, and by comparison with equation 3.24, we find:

$$\left.\frac{\partial^2 K_T}{\partial T^* \partial \delta}\right|_{P;TEC} = \frac{1}{2l} K_T \frac{\partial l}{\partial \delta}\left(\delta - 1\right) f_1\left(\beta^*, P^*\right) \tag{3.28}$$

Let us now consider the sign of this. The first three terms are all positive. The term $(\delta - 1)$ is by necessity negative. All hangs on the sign of $f_1\left(\beta^*, P^*\right)$, which is the δ-independent part of the expansivity, and will take the same sign.

As such, where the expansivity is positive ("normal" density behaviour), $\left.\frac{\partial^2 K_T}{\partial T^* \partial \delta}\right|_{P;TEC}$ will be negative. As such, increasing δ will increase the range over which anomalous compressibility occurs. Where expansivity is negative (that is, there is anomalous density behaviour), increase in δ will decrease the range over which anomalous compressibility occurs. There will be no δ dependence where the TEC line crosses the TMD line; the TEC line is "pinned" at this point, as well as at the zero temperature transition point. This is consistent with our numerical results - see figure 3.3.

This behaviour can be explained as follows. Consider the system at temperatures above the TMD curve. As we increase δ, we favour particles having separations on the shoulder of the potential, by increasing the entropy and pressure driven incentives to do so. As such, there are fewer particles to move up onto the shoulder by increasing pressure, the decrease in system volume by increasing pressure will be less, and therefore compressibility will be lower; this pulls the compressibility minima to higher temperatures and the compressibility maxima to lower temperatures.

At temperatures below the TMD curve, however, many particles do not sample the potential shoulder. Since increasing δ makes occupying the shoulder more favourable, an increase in pressure will cause more particles to move up onto the shoulder at high δ than at low δ, increasing compressibility. This drives compressibility maxima in this region to higher temperatures.

3.4 Summary and Discussion

We have studied a simple shouldered hard rod potential in one dimension using the Takahashi nearest-neighbour gas model, producing exact analytic results. We have shown that this system exhibits a phase transition (albeit a residual zero-temperature phase transition), whereas the unsoftened hard rod potential does not. Further, we have shown that our softened potential exhibits liquid state anomalies of the kind discussed in the previous chapter. We have studied the behaviour of these anomalies, both by studying our exact forms for density and compressibility, and through numerical methods. These behaviours seem amenable to interpretation of the anomalies as a result of structural competition, as has been suggested by other authors. Having a good grasp on this very simple system, we may now turn to the behaviour of core-softened systems in higher dimensions.

Chapter 4

Solid State Approximations

We now begin to study our chosen system, that is, extending work done by Sadr-Lahijany, et al [1], on particles interacting via equation 2.15 in two dimensions. Before turning to direct simulation, it will be useful to perform some exploratory analysis with a series of approximations. In this chapter, we begin to explore the solid part of the phase diagram using the two tried and trusted methods of *ground state calculation* and the *harmonic approximation*. The first of these is powerful, in that it is simple and can give us exact free energies, but limited, in that it only gives us information about the system's behaviour at zero temperature. The second is a natural extension of the first, a second-order approximation that can extend our initial beachhead out into the phase diagram, though it loses accuracy with increasing temperature. These results we gain here will be utilised in chapter 7 as starting points for direct simulation work.

4.1 Ground State Calculations

At zero temperature (the "ground state"), the entropic contribution to a purely classical system's free energy becomes zero. The Helmholtz free energy per particle, a, for a given configuration becomes simply the energy per particle e, and the Gibbs free energy per particle, g, becomes equal to the enthalpy per particle, h:

$$\begin{aligned} a &\equiv e - Ts \\ a(T=0) &= e_{gs} \end{aligned} \tag{4.1}$$

$$\begin{aligned} g &\equiv a + Pv \\ g(T=0) &= e_{gs} + Pv \\ &= h \end{aligned} \tag{4.2}$$

where e_{gs}, the "ground state energy", is the energy per particle of the system in a "ground state" configuration. At zero temperature and positive pressure, and in dimensionality two or greater, the equilibrium phases will almost invariably be crystalline in the sense described in chapter 1. We can also safely assume that the "ground state" configurations for these phases will have all particles sitting exactly on lattice sites, which we shall denote $\mathbf{R}$. For an additive pairwise potential $\phi(r)$, the ground state energy for such a configuration will be given by

$$e_{gs} = \frac{1}{2N} \sum_{\mathbf{R}\mathbf{R}'} \phi(\mathbf{R} - \mathbf{R}') \tag{4.3}$$

These energies are easy to calculate for simple potentials, and can be combined with equations 4.1 and 4.2 to construct zero temperature phase diagrams. In this process, a number of possible lattices are proposed, and their ground state energies as functions of volume calculated. From this, we can calculate what volume of each lattice will give minimum Gibbs free energy at a given pressure (measuring the local minimum within each of a set of restricted free energy spaces), and then which of these minima is lowest and therefore thermodynamically stable (measuring the global minimum across the entire free energy space). This is called a *ground state calculation.*

Phase transition details can be found through the normal phase equilibrium conditions, that is, equality of Gibbs free energy and of pressure between phases:

$$\begin{aligned} g_1(v_1) &= g_2(v_2) \\ P_1(v_1) &= P_2(v_2) \end{aligned} \tag{4.4}$$

with subscripts indicating phase. Pressure as a function of volume can be calculated through the identity $P \equiv -\left.\frac{\partial f}{\partial v}\right|_T$, which at zero temperature becomes:

$$P(v) = -\left.\frac{\partial e_{gs}(v)}{\partial v}\right|_{T=0} \tag{4.5}$$

Since the method already requires the ground state energies as a function of volume, this derivative should take very little extra calculation.

There are two subtleties we must be aware of when using this method. The first is the matter of mechanical stability. Consider a crystal lattice, and within it a particle occupying lattice site $\mathbf{R}$. At equilibrium, there must be no force acting upon this particle, so that

$$\widehat{\mathbf{u}} \cdot \nabla \left(\sum_{\mathbf{R}'} \phi\left(\mathbf{R} - \mathbf{R}'\right) \right) = 0 \tag{4.6}$$

Here, $\widehat{\mathbf{u}}$ is a unit vector of arbitrary direction. This tells us that the lattice point $\mathbf{R}$ is an extremal point in the local energy landscape. This will be true for all sensible lattices, but is not enough to guarantee stability; if this extremal point is not a minimum, then the crystal lattice is not mechanically stable, as the positions of particles occupying the lattice sites will not be stable with respect to any perturbation in their position. So the condition for mechanical stability is that, for all lattice sites $\mathbf{R}$,

$$(\widehat{\mathbf{u}} \cdot \nabla)^2 \left(\sum_{\mathbf{R}'} \phi\left(\mathbf{R} - \mathbf{R}'\right) \right) > 0 \tag{4.7}$$

We note that equations 4.6 and 4.7 are equivalent to saying that our system is occupying a free energy minimum with respect to the dN particle position phase space dimensions, as well as with respect to volume.

When performing a simple implementation of a ground state calculation, explicitly checking stability against every possible set of particle displacements is not feasible[1]. We must content ourselves with testing stability against those deformations which a given lattice is most obviously vulnerable to, and checking the sign of the second derivative of e_{gs} at given v with respect to those parameters of the lattice which describe those deformations.

The second, and more limiting problem with this method is that without proposing and testing an infinite number of lattices it is only ever possible to say that the resulting phase diagram shows the most stable lattice of the proposed set, rather than representing the true free energy minima. Some knowledge of which structures are stable at non-zero temperature (from experimental and/or simulation data for either the system at hand, or one similar) should, if possible, be used as a guide; otherwise, a large set of possible structures should be proposed (see Jagla [51] for an example).

---

[1] Though note that the more advanced harmonic approximation (see section 4.2) can do this for us.

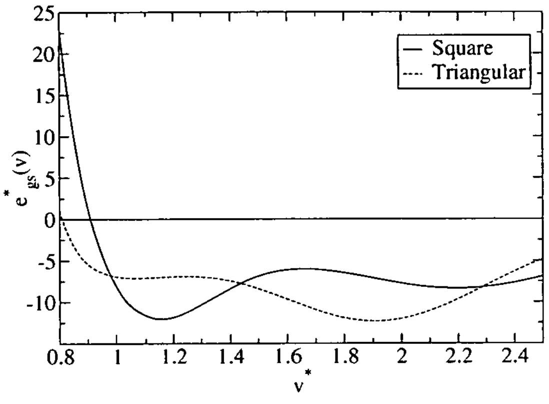

Figure 4.1: Ground state energies for the 2D square and triangular lattices using the potential given by 2.15.

4.1.1 Ground State Results

We have performed a simple ground state calculation for a two dimensional system interacting via equation 2.15, with parameters as stated in chapter 2 and in [1]. Results from this potential are quoted with reduced units as for the standard Lennard-Jones potential, such that:

$$\begin{aligned} e^* &= e/\varepsilon \\ v^* &= v/\sigma^d \\ \rho^* &= N\sigma^d/V \\ T^* &= kT/\varepsilon \\ P^* &= P\sigma^d/\varepsilon \end{aligned} \tag{4.8}$$

Simulation results from Sadr-Lahijany, et al [1] show only square and triangular lattice phases across the region of interest, so these are the lattices which we shall propose for our calculation. Ground state energies per particle for these lattices as functions of volume are shown in figure 4.1 . Rather than calculating the energy for the system in the thermodynamic limit, the energies shown are those for an $N \times N$ lattice, where N is chosen to be the lowest value such that going to an $(N+1) \times (N+1)$ lattice changes the value of e^*_{gs} by no more than one part in 10^6. For both lattices, N is never more than 30 over the range of volumes shown.

Waterloo Maple was then used to calculate analytic expressions for the ground state energies and their derivatives as functions of volume for both square and triangular 30×30 lattices. Conditions for phase coexistence (equation 4.4) were solved for using these expressions (equivalent

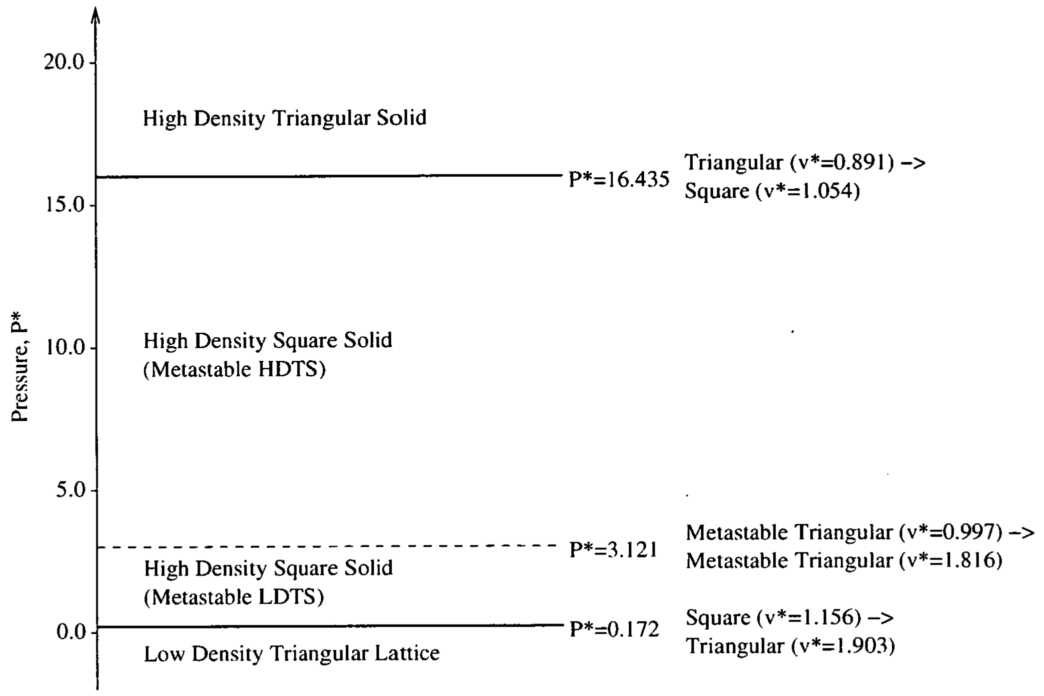

Figure 4.2: Zero-temperature phase diagram for the potential given in equation 2.15. Solid lines indicate transitions between thermodynamically stable phases; dashed lines represent transitions between metastable phases.

to a common tangent construction for the system), giving the zero-temperature phase diagram shown in figure 4.2 .

This phase diagram shows two stable triangular lattice phases bracketing a region ($0.172 < P^* < 16.435$) where the stable phase is a square lattice. The two triangular phases are separated by an isostructural transition (at $P^* = 3.121$), metastable with respect to the square lattice. This hidden transition is due to the region of concavity which can be seen in the triangular lattice ground state energy curve (figure 4.1). There is also a region of concavity in the square lattice phase ground state energy, however it can be seen that it can only yield a transition at negative pressures, where any lattice will be unstable with respect to a gas phase.

Stable square lattice phases are unusual, and normally mechanically unstable, so mechanical stability has been checked explicitly against two possible deformations. The first of these was a Brillouin zone boundary shear deformation, or lattice plane slip, in which neighbouring lattice planes slip past each other in opposite directions. The second was a long-wavelength shear deformation, in which the entire sample is sheared.

To describe these deformations in terms of the lattice, we use a "doubled-up" parallelogram

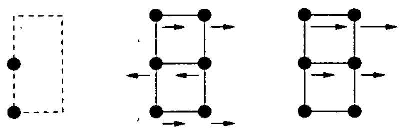

Figure 4.3: a) "Doubled-up" square lattice cell with two-point basis.
b) Lattice plane slip deformation of the square lattice.
c) Long wavelength shear deformation of the square lattice.

unit cell with a two-point basis, as shown in figure 4.3 a. For a lattice spacing r_a, the shape of this doubled lattice cell is described using the matrix $\begin{pmatrix} r_a & 0 \\ \beta & 2r_a \end{pmatrix}$, whilst the basis vectors are given by $\begin{pmatrix} 0 \\ 0 \end{pmatrix}$ and $\begin{pmatrix} \alpha \\ r_a \end{pmatrix}$, with both α and β equal to zero. The parameter α describes the position of one of the particles in the cell; non-zero α moves every other lattice plane slightly across, corresponding to the plane slip as shown in figure 4.3 b. The parameter β describes the shape of the lattice cell, such that a non-zero β gives a parallelogramic cell, corresponding to the long-wavelength shear deformation as shown in figure 4.3 c. If e_{gs} for the square lattice is calculated with this parameterisation, stability against these deformations can checked by finding the sign of $\left.\frac{\partial^2 e_{gs}}{\partial \alpha^2}\right|_{\beta=0}$ around $\alpha = 0$ and the sign of $\left.\frac{\partial^2 e_{gs}}{\partial \beta^2}\right|_{\alpha=0}$ around $\beta = 0$ at given v.

The appropriate derivatives were checked in a Maple calculation, with the square lattice stable against both deformations across volume ranges of $1.0 < v^* < 1.352$ and $2.234 < v^* < 2.680$. The square lattice is therefore stable against these deformations across its range of thermodynamic stability ($1.054 < v^* < 1.156$).

Whilst the zero temperature phase diagram is a good starting point for study of the solid phase diagram, it tells us nothing of the behaviour at non-zero temperature. Further, in a ground state approximation we must explicitly check against given mechanical instabilities. A more sophisticated method is needed, and so we turn to the harmonic approximation.

4.2 The Harmonic Approximation

Above zero temperature, particles in crystalline systems can no longer be expected to sit immobile at their lattice sites, and the entropic contribution to the free energy becomes significant. We will model solid state phase behaviour at non-zero temperature with the *harmonic approx-*

imation [9, 70], which is both simple to implement and exact in the low temperature limit.

We first assume that a system of N particles have equilibrium positions at the sites of a d-dimensional Bravais lattice, with these sites denoted by $\mathbf{R}_i$. We shall further assume that particles are reasonably localised around, and can be associated with, these positions - that is, that their typical separation from their equilibrium sites is small compared to the distance between sites. We denote the separation of the ith particle from its associated lattice site by $\mathbf{u}_i$, so that the actual position of particle i is given by $\mathbf{r}_i = \mathbf{R}_i + \mathbf{u}_i$. If particles interact by a pairwise-additive potential, then the total energy of such a system is given by

$$\begin{aligned} E &= \tfrac{1}{2}\sum_{ij}\phi(\mathbf{r}_i - \mathbf{r}_j) \\ &= \tfrac{1}{2}\sum_{ij}\phi(\mathbf{R}_i - \mathbf{R}_j + \mathbf{u}_i - \mathbf{u}_j) \end{aligned} \tag{4.9}$$

Since we are assuming that all $\mathbf{u}_i$ are small, we can approximate this through a Taylor expansion around the $(\mathbf{R}_i - \mathbf{R}_j)$'s with the $(\mathbf{u}_i - \mathbf{u}_j)$'s as the small parameter. The vector form of the Taylor series is:

$$\begin{aligned} E = & \tfrac{1}{2}\sum_{ij}\phi\left(\mathbf{R}_i - \mathbf{R}_j\right) + \tfrac{1}{2}\sum_{ij}\left(\mathbf{u}_i - \mathbf{u}_j\right)\cdot\nabla\phi\left(\mathbf{R}_i - \mathbf{R}_j\right) \\ & + \tfrac{1}{4}\sum_{ij}\left(\left(\mathbf{u}_i - \mathbf{u}_j\right)\cdot\nabla\right)^2\phi\left(\mathbf{R}_i - \mathbf{R}_j\right) + \ldots \end{aligned} \tag{4.10}$$

The first term in this expansion is the number of particles N times the ground state energy e_{gs} , the second proportional to the force acting on a particle at its equilibrium position, a lattice site, which should be zero by symmetry. Neglecting terms of third order and higher, this gives us:

$$E = Ne_{gs} + \frac{1}{4}\sum_{ij}((\mathbf{u}_i - \mathbf{u}_j)\cdot\nabla)^2\phi(\mathbf{R}_i - \mathbf{R}_j) \tag{4.11}$$

The first term here is known as the ground state potential energy, E_{eq}, and the second term is known as the *harmonic* energy, E_{harm}. Let us now expand the harmonic term into its Cartesian components.

First, we will simplify our nomenclature:

$$\begin{aligned} \mathbf{R}_{ij} &= \mathbf{R}_i - \mathbf{R}_j \\ \mathbf{u}_{ij} &= \mathbf{u}_i - \mathbf{u}_j \end{aligned} \tag{4.12}$$

Greek superscripts will indicate Cartesian components (for instance, in three dimensions, $\alpha, \beta = \{x, y, z\}$). We write the harmonic energy as:

$$E_{harm} = \frac{1}{4} \sum_{ij} \left(\left(\sum_{\alpha\beta} \left(u_i^\alpha - u_j^\alpha\right) \left(u_i^\beta - u_j^\beta\right) \frac{\partial^2}{\partial r^\alpha \partial r^\beta} \right) \phi\left(\mathbf{R}_{ij}\right) \right) \tag{4.13}$$

Multiplying this out followed by some index manipulation gives us:

$$E_{harm} = \frac{1}{2} \sum_{ij} \sum_{\alpha\beta} K_{ij}^{\alpha\beta} u_i^\alpha u_j^\beta \tag{4.14}$$

with the *dynamical matrix* $\mathbf{K}_{ij}$ defined as:

$$\begin{array}{rcll} K_{ij}^{\alpha\beta} & = & \frac{u_{ij}^\alpha u_{ij}^\beta}{R_{ij}^2} \left(\frac{\phi'(R_{ij})}{R_{ij}} - \phi''(R_{ij}) \right) - \frac{\phi'(R_{ij})}{R_{ij}} \partial_{\alpha\beta} & i \neq j \\ K_{ii}^{\alpha\beta} & = & -\sum_{j \neq i} K_{ij}^{\alpha\beta} & \end{array} \tag{4.15}$$

The off-diagonal elements of this matrix represent minus the double derivative in equation 4.13; the condition for the on-diagonal elements ensures that the system is invariant under uniform translations of and rotations around the centre of mass of the system.

Since the $\mathbf{u}$-dependence of the energy has been approximated to only second order in the Taylor series, the $\mathbf{u}$ dependence of the energy contributions for particles in the direction of other particles (the terms summed over in equation 4.14) are parabolic in character. The equations of motion for the N particles on the lattice are therefore those of N coupled *harmonic oscillators* for each component of the displacements - hence *harmonic approximation.* Working in reduced units of particle mass, these equations of motion are :

$$\ddot{u}^\alpha = -\frac{\partial E_{harm}}{\partial \mathbf{u}^\alpha} \tag{4.16}$$

We anticipate that the solutions of this will be in the form of simple plane waves, $\mathbf{u}(\mathbf{R}, t) = \epsilon e^{i(\mathbf{k}\cdot\mathbf{r} - \omega t)}$. Substituting this into the equations of motion gives us the eigenvalue problem:

$$\omega^2 \epsilon = \left(\sum_j \mathbf{K}_{ij} e^{-i\mathbf{k}\cdot\mathbf{r}_{ij}} \right) \epsilon \tag{4.17}$$

The properties of the Bravais lattice restrict solutions to only N non-equivalent values of the wave vector **k**. Since **K** is both real and symmetric, it can be shown that for each of these values of **k**, there will be d eigenvectors ϵ, the polarisation vectors allowed for that wave vector, and d eigenvalues $\omega_a^2(\mathbf{k})$, whose square roots give the frequency of vibration along that wave vector. d of the frequencies should be found to be zero, these correspond to translations of the entire system. If any frequency $\omega(\mathbf{k})$ is found to be imaginary (that is, a negative eigenvalue $\omega_a^2(\mathbf{k})$), then the chosen lattice is mechanically unstable - this is equivalent to the condition for mechanical stability given by equation 4.7. Note that by performing this calculation, stability against *every* possible deformation is checked implicitly, within the limits of the approximation.

For a stable lattice, then, there should be $(dN - d)$ normal modes of oscillation for the particles (corresponding to d polarisations of N wave vectors minus the d zero-frequency modes). In analogy to excitations of the normal modes of the electromagnetic field in quantum mechanics (photons), excitations of these modes are known as *phonons*.

We, however, are more interested in the thermodynamic properties of a system described in the harmonic approximation than in its kinetics. Since we have a form for the energy of the system (see equation 4.11), we can calculate its partition function according to the approximation, Z_{harm}:

$$E(\{u\}) = Ne_{gs} + \frac{1}{2}\sum_{ij}\sum_{\alpha\beta} K_{ij}^{\alpha\beta} u_i^\alpha u_j^\beta \tag{4.18}$$

$$Z_{harm} \equiv \prod_k \int e^{-\beta E(\{u\})} du_k \tag{4.19}$$

By comparison with integrals of Gaussian functions, this becomes:

$$Z_{harm} = e^{-\beta N e_{gs}} \left(\frac{2\pi}{\beta}\right)^{\frac{N}{2}} [\det \mathbf{K}]^{-\frac{1}{2}} \tag{4.20}$$

which allows us to calculate all thermodynamic properties normally; principally, the approximate Helmholtz free energy per particle:

$$\begin{aligned} \beta a_{harm} &\equiv -\frac{\ln Z_{harm}}{N} \\ &= \beta e_{gs} - \tfrac{1}{2}\ln\tfrac{2\pi}{\beta} + \tfrac{1}{2N}\ln[\det \mathbf{K}] \\ &= \beta e_{gs} - \tfrac{1}{2}\ln\tfrac{2\pi}{\beta} + \tfrac{1}{dN-d}\textstyle\sum_{\omega_a^2\neq 0}\ln\omega_a^2 \end{aligned} \tag{4.21}$$

The restriction on the summation over the eigenvalues corresponds to fixing the position of the centre of mass of the system (since modes of oscillation where $\omega_a(\mathbf{k}) = 0$ correspond to translations of the entire system).

From this, we can work out the phase diagram in the harmonic approximation for a system with a similar method to that used for finding the ground state phase diagram: propose a number of lattices, calculate the ground state energy and dynamical matrix, check for mechanical stability by ensuring all eigenvalues are positive, and find lines of phase transition by equating pressure and Gibbs free energy at each temperature. This will normally be carried out numerically rather than analytically, using a finite lattice of N particles with periodic boundary conditions and the minimum image convention (that is, particles interact with the nearest periodic image of other particles - see chapter 6 and reference [71]). Finite size effects to the calculated free energy per particle f are expected to be of order $\frac{\ln N}{N}$ [72].

It can be seen from equation 4.21 that, as temperature tends to zero, the harmonic approximation tends to the exact ground state free energy (equation 4.1); as such, the harmonic approximation is a controlled approximation, exact in the low temperature limit. However, as temperature increases, particles will stray further and further from their lattice points, invalidating the underlying assumptions of the approximation. We must be aware that at high temperatures, or under other circumstances where these assumptions may be invalid (such as the appearance of defects in a two dimensional crystal near melting), the approximation will break down altogether. By including higher order terms in the Taylor expansion of equation 4.10, it is possible to construct *anharmonic* approximations to overcome these problems, though we will not consider such theories here.

4.2.1 Harmonic Approximation Results

The procedure given above for calculation of phase coexistence was implemented numerically in the C language. The eigenvalues of the dynamical matrix for a lattice at a given volume were solved for using an implementation of the QL algorithm with implicit shifts [73]. Our code warns if there exist more or less than d zero eigenvalues (the "soft" phonon modes) - note that computer calculations of these modes will only give approximate zeroes, so are in practise found to be of values within a given tolerance factor of zero. The code also warns if negative modes are found - that is, if the crystal structure is found to be mechanically unstable at given volume. The logarithms of the non-zero eigenvalues are then summed to calculate the harmonic free energy, which is combined with the calculated ground state energy to give the full free energy within the approximation. The conditions for phase coexistence are solved for using an implementation of the Newton-Raphson method [73], with the pressure calculated using a central difference method.

This code was used to find the phase diagram in the harmonic approximation for a 2D system of 16×16 particles on square and triangular lattices interacting via the potential given in equation 2.15. With this size lattice, the finite size corrections to the harmonic free energy should be of the order of 0.01, with the free energies found to be of the order of 10. Above the 16×16 system size, the vast increase in computational time (the algorithm is $O(N^2)$) is not worth the extra precision.

As a consistency check, the code was used to find volumes at which the square lattice becomes mechanically unstable - that is, at which negative frequencies are found. A range of such volumes was found as $1.343 < v^* < 2.234$. The upper bound is identical to that found above for stability against shear deformations in the ground state energy calculation. The lower bound of $v^* < 1.343$ is lower than the bound of $v^* < 1.352$ found for the limit of stability with respect to shear. This is attributed to instability against some deformation other than shear or lattice plane slip, and is consistent with our ground state calculation results.

Coexistence lines were calculated up to a reduced temperature of 0.9; these are plotted in figure 4.4. As shown by the ground state calculation, we have a low pressure region of a low density triangular solid (LDTS) phase , passing through a transition into a high density square solid (HDSS) phase with increasing pressure. At high pressures, a further transition takes us into a high density triangular solid (HDTS) phase. A hidden triangular-triangular transition line exists in the square lattice's region of stability. Figure 4.5 a shows the $T - \rho$ projection of this phase diagram.

We note in passing a curiosity which can be seen straight away in the HDSS-HDTS transition (see figure 4.4); the coexistence line passes through a pressure maximum at around $T^* = 0.51$. From the Clausius-Clapeyron equation $\left(\frac{dP}{dT} = \frac{\Delta S}{\Delta V}\right)$, at this point these two phases have equal entropy.

We see in figure 4.4 that the hidden isostructural triangular-triangular transition line stops at $T^* = 0.205$, and that the LDTS-HDSS transition line stops at $T^* = 0.575$. Above these tem-

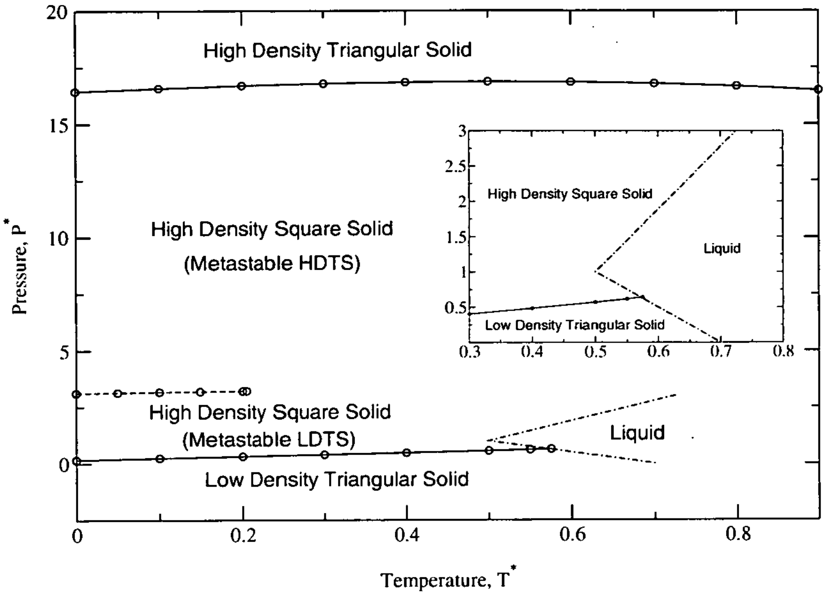

Figure 4.4: Low-temperature phase diagram in the harmonic approximation for the potential given in equation 2.15. Solid lines indicate transitions between thermodynamically stable phases; dashed lines represent transitions between metastable phases. The dot-dashed line shows the melting curve reported in reference [1].
Inset: The same phase diagram viewed on the same scale as shown in reference [1].

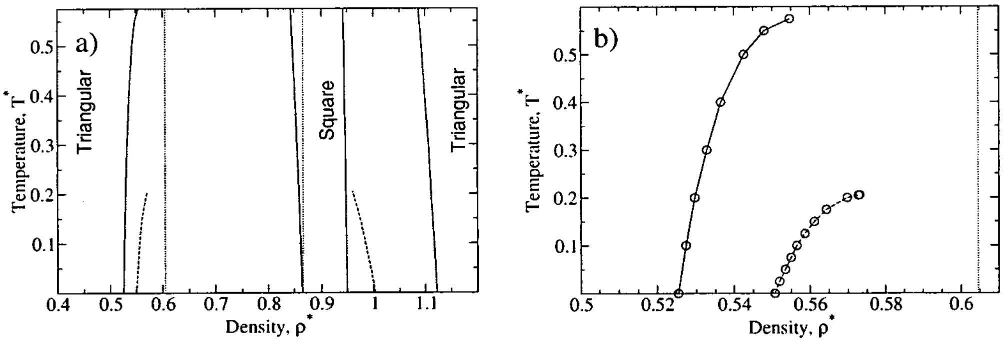

Figure 4.5: a) $T - \rho$ projection of figure 4.4. Solid lines indicate binodals, curves showing the equilibrium coexistence densities between phases. Dashed lines indicate the binodal for the metastable triangular-triangular transition. Between the dotted lines, the triangular lattice is not mechanically stable within the harmonic approximation.
b) Enlarged portion of (a), showing the low-density triangular binodal curve for the triangular-triangular transition (lower, dashed, curve) and the open square-triangular transition (upper curve). Symbols indicate the points at which the coexistence densities were evaluated. The dotted line shows the density above which the open triangular lattice loses mechanical stability.

peratures, the method used could not find densities for the LDTS phase which satisfy the coexistence conditions. Figure 4.5 b shows an enlargement of figure 4.5 a, showing the low-density side of the LDTS halves of the appropriate binodal curves, as well as the temperature-independent density above which the LDTS lattice loses mechanical stability within the approximation. It can be seen that the binodal curves are rapidly approaching this limit of mechanical stability; no further solutions to the coexistence conditions can be found because no stable coexistence volumes exist within the approximation above these temperatures.

We note that the LDTS lattice loses stability along the LDTS-HDSS lattice transition remarkably close to the melting line reported from the molecular dynamics results of Sadr-Lahijany et al [1]. We have already noted how the harmonic approximation should break down close to melting in two dimensional systems, which explains why this coexistence line meets the reported melting curve well below its triple point; the loss of stability can be explained as a complete break down of the approximation.

For the isostructural transition line, we suggest that the loss of stability is caused by approach to an isostructural critical point. As the volumes of the coexisting phases approach each other, it is possible that one or both phases could reach a volume at which mechanical stability is lost. Alternatively, the loss of stability could represent a breakdown of the harmonic approximation close to an isostructural critical point, with the triangular lattices in the true system maintaining mechanical stability.

4.3 Summary and Discussion

We have used both a ground state calculation and the harmonic approximation to examine the solid state phase diagram of our chosen system. Our results are consistent with those presented by Sadr-Lahijany, et al [1], who note that the liquid phase coexists with an open triangular lattice at low pressure and a dense square lattice at high pressure. The harmonic approximation LDTS-HDSS coexistence line does not pass through the triple point found by those authors, but we note that we cannot expect this approximation to be accurate near melting. We note the further existence of a dense triangular lattice at very high pressure, with the harmonic approximation suggesting that the high pressure square-dense triangular lattice transition line exhibits a pressure maximum.

It is possible that the two triangular lattices are not thermodynamically connected. Our results show that they are separated by an isostructural transition at low temperature, though this transition is hidden behind the stable square lattice phase. The harmonic approximation suggests that there is a region of volumes between those seen in the stable triangular phases across which the triangular lattice is not stable, though it is possible that anharmonic effects could stabilise the lattice here, in which case the hidden isostructural transition line could end in a critical point, rather than a triple point meeting a line of transition to the next-most-stable lattice phase. The pressure at which this hidden transition line occurs is too high for effects of this possible hidden isostructural critical point (such as a metastable island of hexatic phase, as discussed by [52]) to be causing the thermodynamic singularity in the metastable liquid phase suggested by Sadr-Lahijany et al [1].

These results give us a foothold in the solid state part of the phase diagram for this system, which we will return to in chapter 7.

Chapter 5

Lennard-Jones Devonshire Cell Theory

Having begun to numerically explore the solid state of our system, we now turn to the fluid state. Most modern work on fluid equations of state use density functional theories. However, the work which we are following [1] uses an older model for fluid state behaviour, the Lennard-Jones Devonshire Cell theory, to investigate the possibility of liquid-liquid phase separation. Using this model, the authors claim to find two lines of first order phase transition, both ending in critical points, one of which is the expected liquid-gas transition line, the other a novel transition separating a low density liquid from a high density liquid.

In this chapter, we will discuss the Lennard-Jones Devonshire cell theory (hereafter abbreviated to *LJD cell theory*), its use and its limitations. We will attempt to reproduce the behaviour observed for the model by Sadr-Lahijany, et al, and discuss the implications of our results.

5.1 Background and Model

LJD cell theory [74, 75, 76, 77] is a mean-field lattice approximation to the liquid state. Until the advent of density functional theories, it was the main method for calculation of liquid equations of state [78], and remains in research use today [1, 79].

In the model, particles are considered to be localised in singly occupied "cells". These cells are centred on the sites of a fully occupied lattice, and particles are considered to move independently within these cells, with the lattice sites as their equilibrium positions. For simplicity, cells are assumed to be spherical, and are of volume $v = V/N$, radius s. The interactions with the neighbours of a particle are simplified by "smearing" them across the surface of a further sphere, radius r_a, concentric with the cell. The volume of this "interaction shell" is related to the cell volume by:

$$r_a^3 = \gamma v \tag{5.1}$$

where γ is a lattice-dependent constant, chosen such that for a primitive unit cell of volume v, the lattice parameter r_a will be the radius of the interaction shell (see figure 5.1 a). Interactions with particles beyond nearest neighbour are neglected.

The Helmholtz free energy within this approximation is given by:

$$a = -kT \ln v_f \sigma_c + \frac{e(\mathbf{O})}{2} \tag{5.2}$$

Here, $e(\mathbf{O})$ is the ground state energy for the lattice (normally the same as e_{gs} from the previous chapter); σ_c is a constant "communal entropy" term[1], which accounts for the entropy lost due to the localisation of particles into cells; and v_f is the "free volume", given by:

$$v_f = \int_\Delta e^{-(U(\mathbf{r})-e(\mathbf{O}))/kT} d\mathbf{r} \tag{5.3}$$

with $U(\mathbf{r})$, the "cell potential", as the interaction energy of a particle at a position $\mathbf{r}$ within its cell, and the integral being carried out across the cell volume.

Within this approximation, it is a simple matter to calculate the interaction of a particle with its neighbours. The radial symmetry of the system allows us to reduce $U(\mathbf{r})$ to $U(r)$, where r is the radial coordinate of the particle's position within the cell. Figure 5.1 b shows the geometry within the cell. Simple trigonometry gives us the separation R between the particle at $\mathbf{P}$ and an element dA of the shell. If the shell represents c particles and the interparticle potential is given by $\phi(R)$, the total interaction of the particle with the shell $U(r)$ is given by:

$$U(r) = c\frac{\int_{shell} \phi(R) dA}{\int_{shell} dA} \tag{5.4}$$

---

[1] Reference [74] assigns $\sigma_c = e$, although the exact value chosen for σ_c has no impact upon phase coexistence as long as it remains independent of volume.

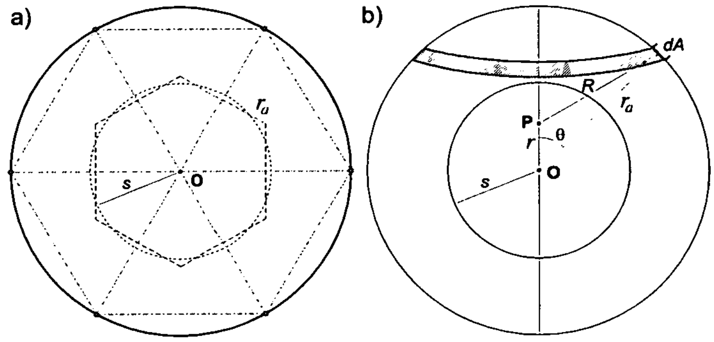

Figure 5.1: a) A two dimensional cell (dotted circle) of volume v and radius s is assumed to be centred on a lattice site with primitive unit cell (dashed hexagon) of the same volume. The underlying lattice is shown with dot-dashed lines, with lattice sites as filled points. The interaction with neighbouring lattice sites is approximated with an interaction shell (full circle), of radius the same as the lattice spacing a.
b) The geometry for the interaction of a particle at position $\mathbf{P}$ within a three dimensional cell with an element of the shell dA. Given the radial coordinate r of the particle, the angular coordinate θ of the element and the shell radius a, it is simple to calculate the separation R between particle and shell element; from this, the interaction can be integrated around the shell.

Here, the integral is carried out across the surface of the interaction shell. This integral would normally be carried out numerically, with further numerical integration to calculate the free volume according to equation 5.3 for given density ρ, which enters through the limits on the integrals.

In their original implementation of this method, Lennard-Jones and Devonshire approximated the phase diagram for the 12-6 Lennard-Jones potential, given by:

$$\phi(r) = 4\varepsilon\left(\left(\frac{\sigma}{r}\right)^{12} - \left(\frac{\sigma}{r}\right)^{6}\right) \tag{5.5}$$

We quote reduced units for this potential as shown in equation 4.8.

Lennard-Jones and Devonshire used an fcc lattice, which has coordination number $c = 12$ and geometric constant $\gamma = \sqrt{2}$. The value of $U(r)$ (equation 5.4) was calculated using the 12-6 Lennard-Jones potential; however, the ground state energy $e(\mathbf{O})$ appearing in equation 5.3 was calculated using the potential:

$$\phi(r) = 4\varepsilon\left(\left(\frac{\sigma}{r}\right)^{12} - 1.2\left(\frac{\sigma}{r}\right)^{6}\right) \tag{5.6}$$

This is a modified 12-6 Lennard-Jones potential, with the attractive part increased in strength by 20%. This modification was motivated as representing the effects of next and higher nearest neighbour interactions.

For this system, Lennard-Jones and Devonshire found a critical point[2] at $T_c^* \approx 1.3$, $P_c^* \approx 0.6$, $\rho_c^* \approx 0.56$. These results should be compared with the consensus arising from a number of simulation studies of criticality in the LJ fluid, the most recent and sophisticated of which [80] quotes $T_c^* = 1.3120(7)$, $P_c^* = 0.1279(6)$, $\rho_c^* = 0.316(1)$. The accuracy with which the cell theory appears to predict the critical temperature of the LJ fluid has long been regarded as its major success [75].

5.2 The 12-6 Lennard-Jones Fluid

We have obtained the cell theory phase diagram for the 12-6 Lennard-Jones fluid, using the same model parameters as the original study. This was performed, initially at least, as a consistency check for our implementation of the method.

Using the Romberg method [73], numerical integration was carried out to calculate the cell potential and thence free volume and Helmholtz free energy (according to equations 5.2-5.4) for the system at given v. An initial equation of state for the system was found by using a golden section search [73] to minimise the Gibbs free energy with respect to v on a grid of points in (P, T) space, with phase transitions located as apparent discontinuities in $T - v$ curves. Like simulation and experiment, this golden section search method is vulnerable to finding local minima in the free energy curve near phase transitions, so the method was supplemented by using a Newton-Raphson root finding algorithm [73] to solve for the standard coexistence conditions, using the approximate coexistence points from the golden section search as starting points. Critical points are approximated as the first point along a phase boundary where no distinct coexistence volumes could be found.

The results from this implementation can be seen in figure 5.2. We find a critical point at $T_c^* = 1.354, P_c^* v_c^* / T_c^* = 0.68$; we suggest that we have indeed duplicated the critical point from the original study [74]. However, our full phase diagram shows *two* lines of first order transition, meeting at a triple point, *both* terminating in critical points.

Since LJD cell theory is a lattice model, accurate representation of non-lattice phases is not

---

[2] Hill [75] describes the cell theory without the modified ground state term used by LJD, but quotes the critical parameters corresponding to a modified system defined in reference [82], which uses further interaction shells to account for next and higher nearest neighbours.

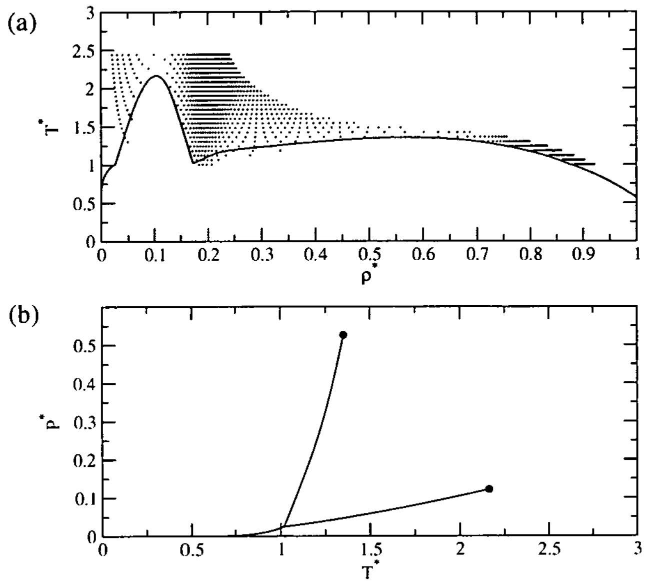

Figure 5.2: (a) (ρ, T) projection of the modified cell theory LJ potential phase diagram. Dots show density points found using the golden section search. Solid lines show coexistence densities. (b) (P, T) projection of the same phase diagram. Solid lines indicate lines of first-order phase transition, filled circles indicate critical points. Note that the lower temperature, higher pressure critical point is that found by Lennard-Jones and Devonshire.

possible, making accurate physical characterisation of the phases seen in figure 5.2 impossible. However, a plausible identification of the phases is suggested by the shape of the phase diagram near the triple point, where it resembles that of the true 12-6 Lennard-Jones fluid, with a low pressure, low density gas phase, an intermediate liquid phase and a high pressure, high density solid phase. We will support this characterisation of the phases by examining their cell potentials, calculated at the triple point ($T_c^* = 1.02, P_c^* = 0.025$). These can be seen in figure 5.3. Figure 5.3 a shows the cell potential for the low density phase; this is three orders of magnitude less than kT across the whole cell, so this phase can quite reasonably be interpreted as gas-like. In contrast, the cell potential for the high density phase (figure 5.3 b) has a very steep minimum at $r = 0$, the centre of the cell. The hard core repulsion of the particle's neighbours makes the potential very large and positive away from the cell's centre. As such, the particle is strongly confined to its lattice site, so we interpret this as a solid-like phase. Finally, figure 5.3 c shows the cell potential for the intermediate density phase. We see that its form is similar to that of the gas like phase, with a broad "hump" in the middle of the cell, of height around kT; the particle is still reasonably free within the cell. We interpret this as a

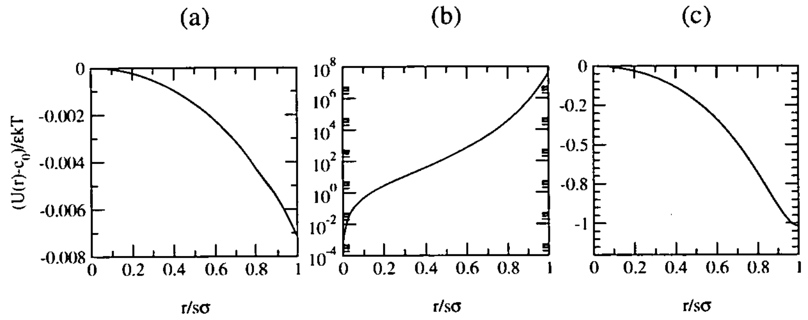

Figure 5.3: Radially symmetric cell potentials for the modified cell theory with LJ potential, calculated at the triple point from figure 5.2.
(a) Potential for the low density phase ($\rho^* = 0.026$)
(b) Potential for the high density phase ($\rho^* = 0.869$)
(c) Potential for the intermediate density phase ($\rho^* = 0.171$)

liquid-like phase. With these assignments, the critical point found by Lennard-Jones Devonshire is between a *solid*-like and liquid-like phase, whilst the other, lower-temperature critical point at $T_c^* = 2.17, P_c^* = 1.221, \rho_c^* = 0.104$ terminates a line of liquid-gas like transition.

We point out that these results are not a consequence of Lennard-Jones and Devonshire's modification of the potential. We have performed calculations using the unmodified potential to calculate $e(\mathbf{O})$, and find a qualitatively similar phase diagram and cell potentials, though with the solid-liquid like critical temperature reduced to $T_c^* = 0.82$.

5.3 Reappraisal of the LJD cell theory

We have found that the original LJD cell theory critical point for the 12-6 potential terminates a line of pseudo solid-liquid coexistence, rather than a liquid-gas coexistence, as originally suggested; further, that the model shows another first order transition line, which we believe to be a better candidate for the liquid-gas transition. It seems likely that Lennard-Jones and Devonshire were not aware of this second line of transition, since at the time of their study, numerical integration was a time-consuming and labour intensive matter, making it difficult to extend the calculations down to the rather low densities at which the gas-like phase appears. Also, the proximity of their critical point temperature to that for the "real" 12-6 LJ critical point (estimated at the time from experimental data for Argon) would have made the attribution extremely tempting. In hindsight, the agreement in temperature can only be regarded as coincidental, since mean field theories (such as the cell model) are expected to considerably overestimate the critical temperature, as they cannot take into account large fluctuations. The liquid-gas like critical point here does indeed do so.

A critical point between liquid-like and solid-like phases can have no physical equivalent. It is an artifact of the cell theory, in which cell volume is the only available order parameter, since the model imposes the orientational and translational symmetries of an underlying lattice upon fluid-like states, which in reality have no such symmetries. This inability to accurately represent disordered phases has long been appreciated even if the existence of artifact solid-liquid critical points has not, and several attempts have been made to "patch" the model against this and other shortcomings. These include zero and multiple occupancy of cells ("hole" theories) [75, 81], calculations of interactions with second and higher nearest neighbours (see for example reference [82]), use of Monte Carlo integration to give more accurate cell shapes and free volumes [83], and differing methods for calculating the cell potential (see eg. reference [79]). However, none of these extensions fully address the underlying lattice approximation which renders any cell theory equation of state for a liquid suspect - by definition, a liquid is a disordered state without a lattice. Even hole theories will only be able to represent a liquid of appreciable density as a highly defective crystal.

If a basic cell theory for even a simple 12-6 Lennard-Jones potential exhibits two critical points, use of cell theory to study possible liquid-liquid phase separation should be treated with caution. Because of this, we will now attempt to reproduce the cell theory results of Sadr-Lahijany, et al, and examine them in the context of our findings about the model.

5.4 The 2D Sadr-Lahijany Potential System

In reference [1], Sadr-Lahijany, et al, briefly discuss the use of cell theory to investigate the possibility of a second fluid phase critical point in two dimensions, using their potential (equation 2.15). Whilst they do not go into detail about their cell theory implementation[3], they do quote equations for the free volume and Helmholtz free energy differing from our equations 5.2 and

---

[3] The closest implementation to SadrLahijany's we have found in the literature is used in work by D.A. Young to calculate the solid state free energy of a system with a square-well type potential [50]. The Young form for the free energy is as equation 5.7, with a free volume given by $v_f = \int_\Delta e^{-U(\mathbf{r})/2kT} d\mathbf{r}$, and is "based on agreement with molecular dynamics data ... in the square well solid."

5.3. In our nomenclature, Sadr-Lahijany, et al calculate the free energy using:

$$a = -kT \ln v_f \sigma_c \tag{5.7}$$

with $\sigma_c = 1$. Their free volume is given by:

$$v_f = \int_{\Delta} e^{-U(\mathbf{r})/kT} d\mathbf{r} \tag{5.8}$$

This is equivalent to equations 5.2 and 5.3 with $e(\mathbf{O}) = 0$. No detail is given concerning the underlying lattice used; it seems reasonable that they would have used a triangular lattice, which has lattice constant $\gamma = 2/\sqrt{3}$ and coordination number $c = 6$. Using this model, the authors report two lines of first order phase transition ending in critical points, one at low pressures corresponding to liquid-gas phase separation, the other at higher pressures corresponding to liquid-liquid phase separation, with a critical point C' at $T^*_{C'} \approx 0.4, P^*_{C'} \approx 1.5$.

We have attempted to reproduce these results, to check whether or not this second critical point is a cell theory artifact liquid-solid transition.The phase diagram we have found is shown in figure 5.4. Whilst this phase diagram does indeed show two critical points, neither point is at the coordinates described in reference [1]. As with the 12-6 Lennard-Jones potential, our results show three phases, separated by three lines of first order phase transition meeting at a triple point, and two critical points. Unlike the Lennard-Jones potential, the slope of one of the lines of phase transition is negative. We will once again cautiously attempt to identify these phases through their cell potentials evaluated at the triple point, seen in figure 5.5. We will start with the low density phase cell potential, as seen in figure 5.5 a. This potential has a very steep central minimum, which leads to strongly confinement of particles to the centres of their cells. We must identify this phase with a solid. The cell potential for the highest density phase (see figure 5.5 c) shows similar character, and we will identify this phase as solid-like as well. The presence of two separate solid phases is due to the shape of the interparticle potential; in the low density phase, particles sit in the bottom of the Gaussian well part of the interaction with their neighbours, whilst in the high density phase, they sit at the ledge of the potential due to the minimum of the Lennard-Jones part of the interaction, with the Gaussian well part overcome by the Lennard-Jones hard core repulsion.

The intermediate density phase has the cell potential shown in figure 5.5 b. Here, the cell

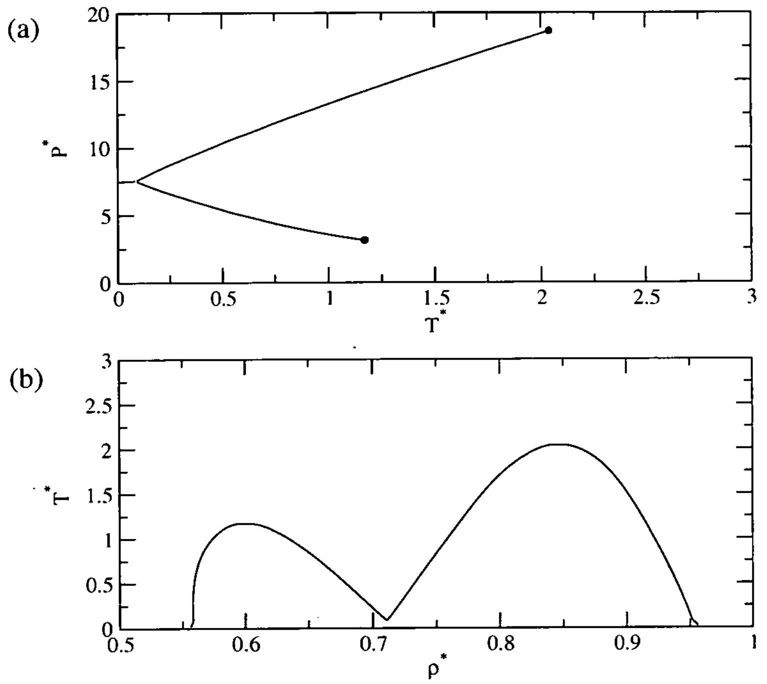

Figure 5.4: Phase diagram for the Sadr-Lahijany cell theory form using the core-softened potential (equation 2.15). Compare with figure 5.6.

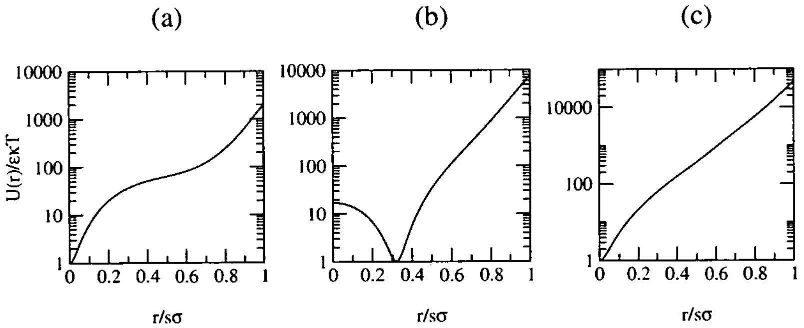

Figure 5.5: Radially symmetric cell potentials for the core-softened potential, calculated at the triple point from figure 5.4. Note that, for the logarithmic plots, the energy scale zero has been shifted for purposes of clarity.
(a) Potential for the low density phase ($\rho^* = 0.558$)
(b) Potential for the intermediate density phase ($\rho^* = 0.715$)
(c) Potential for the high density phase ($\rho^* = 0.952$)

potential has a local maximum at the centre, on the lattice site. Surrounding this in a ring is a steep energy minimum, at radial coordinate $r/s\sigma \approx 0.325$. Though this minimum has a depth of order $10kT$, we will characterise this phase as fluid-like. This is because the energy maximum at the lattice site indicates that this lattice is mechanically unstable at this density. The shape of this potential occurs at densities where the lattice site sits between the minima of the Lennard-Jones and the Gaussian well parts of the interparticle potential, but the Gaussian well is not completely swamped by the Lennard-Jones repulsive contribution.

For this model, then, we find neither a liquid-gas transition nor a liquid-liquid transition, but instead two liquid-solid transitions with artifact critical points, and a low-density solid-like phase which will change to a gas-like phase with decreasing pressure without a transition. Since we have failed to reproduce the results of Sadr-Lahijany, et al with this model, we will make one further attempt, returning to equation 5.2 for the free energy and equation 5.3 for the free volume.

Using this form for cell theory, we find the phase diagram shown in figure 5.6 . The same phase diagram on a larger scale, showing the full extent of the coexistence lines, is shown in figure 5.7 . This shows four phases (identified with roman numerals i – iv), with two critical points (once again, neither is at the coordinates given by Sadr-Lahijany, et al) and one triple point. We will attempt to characterise these phases using the now-familiar method.

The cell potentials are shown in figure 5.8 . Figures 5.8 a-c show the cell potentials evaluated at the triple point for phases i-iii. We also show cell potentials for phases iii and iv (figures 5.8 d and 5.8 e); these are evaluated at the triple point temperature and phase iii-iv coexistence.

We see that phase ii (figure 5.8 b) and phase iv (figure 5.8 d) are solid-like, with deep central wells. As with the Sadr-Lahijany version of the cell theory, the two separate solid phases correspond to the central well being near either the Gaussian well minimum of the interparticle potential, or the Lennard-Jones minimum. We also see two fluid-like phases with energy maxima at the cell centres. Phase iii (figures 5.8 c and 5.8 d) is similar to the intermediate density phase of the Sadr-Lahijany cell theory, and so we attribute it as liquid-like. Phase i has the centre of the cell occupying the tail of the interparticle potential, and can be attributed as somewhat gas-like.

This gives us a phase diagram similar to that given by the Sadr-Lahijany cell theory, but with a liquid-gas transition (cutting off the low-pressure solid-liquid artifact critical point), and

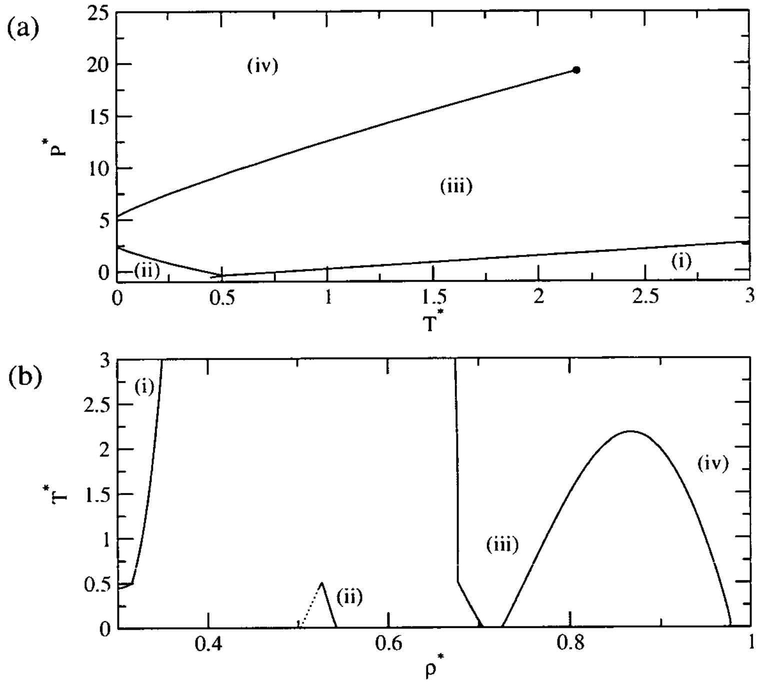

Figure 5.6: "Standard" cell theory phase diagram projections for the core-softened potential (see equation 2.15), with phases identified by roman numerals i – iv. No coexistence data is available between the two lowest density phases, i and ii, below a temperature of $T^* = 0.44$, as below this temperature the lowest density phase i reaches zero density to machine precision, causing the root-finding algorithm to fail. As such, the dashed line in the $\rho - T$ projection is a purely schematic continuation for purposes of clarity.

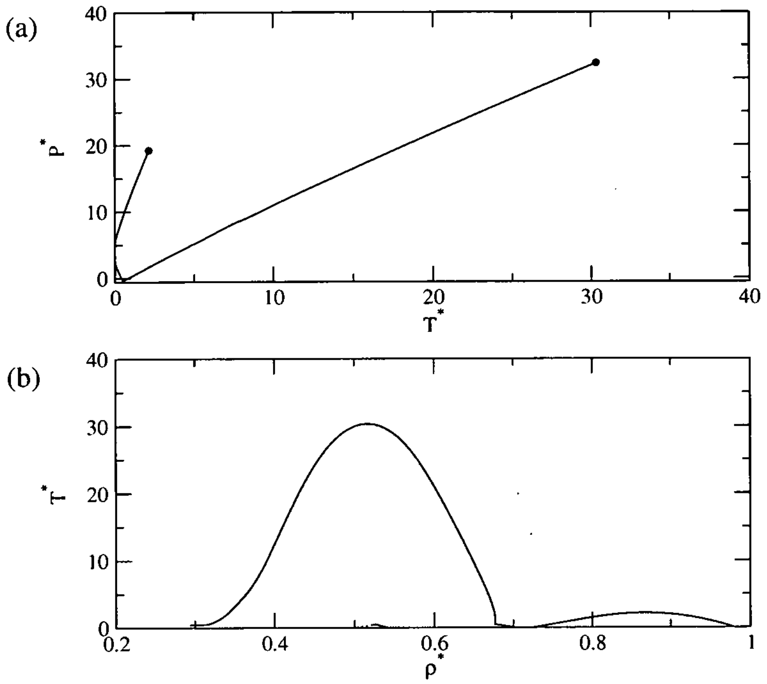

Figure 5.7: Larger scale view of figure 5.6, showing the full extent of the coexistence lines.

without the solid-solid transition. Our two critical points are liquid-gas like and liquid-solid like, and once again we find no evidence for a liquid-liquid transition.

5.5 Summary and Discussion

Our major finding here is that the original LJD cell theory critical point [74] was misattributed, with this misinterpretation continuing to the present day. The major problem here is that simple cell theory is really a theory of the solid lattice state, a first-order expansion around lattice displacements without particle position correlations, and is not really applicable to the liquid state. Whilst this flaw in the theory has long been appreciated [77], its full consequences, that is, the existence of solid-liquid artifact critical points within the model, has not.

We have been unfortunately unable to reproduce Sadr-Lahijany's results. They appear to have used a non-standard cell theory implementation, of which their work [1] gave insufficient detail for us to duplicate. Even so, it seems likely that their reported "second critical point" is more likely to be of solid-liquid like character, and an artifact of the cell theory, rather than representing a second critical point in the fluid phase, as they believed.

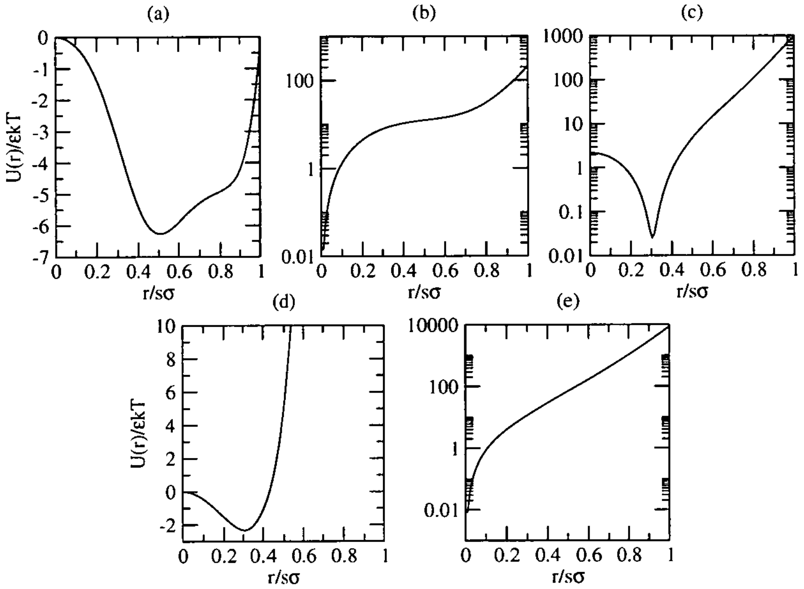

Figure 5.8: Radially symmetric cell potentials for the phases from figure 5.6. Note that, for the logarithmic plots, the energy scale zero has been shifted for purposes of clarity.
a) Potential for the low density phase (i) ($\rho^* = 0.315$) calculated at the triple point.
b) Potential for the intermediate density phase (ii) ($\rho^* = 0.527$) calculated at the triple point.
c) Potential for the high density phase (iii) ($\rho^* = 0.677$) calculated at the triple point.
d) Potential for the high density phase (iii) ($\rho^* = 0.750$) calculated at the triple point temperature and (iii)-(iv) coexistence.
e) Potential for the very high density phase (iv) ($\rho^* = 0.966$) calculated at the triple point temperature and (iii)-(iv) coexistence.

Whilst there are qualitative similarities between our cell theory results and both Sadr-Lahijany's simulation results (the presence of lines of transition with negative slope) and our own solid state results (the presence of two solid-like phases with the same lattice structure), quantitative agreement is very poor. We can see from comparison with our solid state results that as well as a poor approximation to the liquid state, cell theory is also a poor approximation to lattice states.

In summary, cell theory has provided us with no new information on the "true" physical behaviour of this system, and despite previous reports, its use leaves us none the wiser on the existence or otherwise of liquid-liquid transitions in the system we have chosen to study.

Chapter 6

Monte Carlo Methods

We are now in a position to investigate our system with direct simulation methods. Two main methods are available for this; Monte Carlo (MC) simulations and Molecular Dynamics (MD) simulations. The first proceeds in the spirit of statistical mechanics, attempting to numerically integrate a quantity proportional to the configurational integral, whilst the second has more of a classical mechanics bent to it, attempting to solve Newton's equations of motion for the system. Both should give equivalent results. Whilst Sadr-Lahijany, et al, used MD simulations, in this work we turn to MC simulation work. This means that we turn away from the dynamics of the system, but enables us to investigate the "open" ensembles (NPT and μVT) more easily.

We will begin this chapter with a brief illustration of the principles behind Monte Carlo simulation, following one of the standard works on the subject [71]. We will follow this with a discussion of the extensions to this basic algorithm which we have used in this work, some of which are well documented elsewhere, others of which of more recent additions to the simulation toolkit.

6.1 Basic Monte Carlo

The idea of simulation is to perform a "virtual experiment" in which we can measure the same observables we measure in "real" experimental work. As we know, in statistical mechanics these observables are given by ensemble averages. We recall from chapter 1 that the ensemble average for such an observable $\mathcal{A}$ in the NVT ensemble will be given by:

$$\langle \mathcal{A} \rangle_{NVT} = \frac{\int d\mathbf{r} \mathcal{A}(\mathbf{r}) e^{-\beta U(\mathbf{r})}}{\int d\mathbf{r} e^{-\beta U(\mathbf{r})}} \tag{6.1}$$

Since these integrals are rarely analytically tractable, we will turn to methods of numeric integration. A naive first approach might be to attempt to evaluate the integrals with a simple quadrature, such as Simpson's Rule. Such simple quadratures involve dividing the interval of each integral into n equally spaced abscissas, evaluating the function to be integrated at each of these points, and approximating the integral through some combination of these calculated values. This is an effective method for integration in one or two variables, but not for this problem. If the physical system we represent is d dimensional, then the number of function evaluations required will be n^{Nd}. If we were to study a system of only 100 particles in three dimensions, using only 10 abscissas, we would have to perform an incredible 10^{300} function evaluations. Worse still, across most of the phase space, there would be significant overlap between particles, giving a vanishingly small Boltzmann factor, so most of the vast number of evaluations would contribute virtually nothing to the integral.

6.1.1 Simple Monte Carlo Integration

A more efficient method is to perform our function evaluations at randomly chosen points across phase space. Whilst in quadrature, a fixed number of function evaluations *must* be carried out across the phase space for the results to be combined meaningfully, by picking random points we avoid this. Our estimate for the integral, and our estimate of the error of this, can be refined as we go, until we reach a desired level of accuracy. Whilst less efficient for one-variable integration, even for three-variable integrations such *Monte Carlo* integration can far outstrip normal quadrature [73, 71].

The simplest implementation of this is to pick our evaluation points independently, from a probability density uniform across the phase space. To combine our function evaluations, we simply note that any integral can be rewritten in terms of an average, thus:

$$\int_V f(\mathbf{r}) d\mathbf{r} = V \left(\overline{f(\mathbf{r})} \right) \tag{6.2}$$

with the average performed over the region of integration. Therefore, in this simple implementation, we can estimate this "true" mean, and the error in our estimate, through standard statistics.

Though we will no longer be performing an astronomical number of calculations, most of our evaluations will still contribute very little to our integrals. As such, this method, the very simplest form of Monte Carlo numerical integration, is still not suitable. We must find a way to concentrate our function evaluations in the regions of phase space which contribute most to our integrals.

6.1.2 Importance Sampling

Let us recast equation 6.1 in terms of of a probability density function, $p_{NVT}(\mathbf{r})$, thus:

$$\langle \mathcal{A} \rangle_{NVT} = \int d\mathbf{r} \mathcal{A}(\mathbf{r}) p_{NVT}(\mathbf{r}) \tag{6.3}$$

$$p_{NVT}(\mathbf{r}) = \frac{e^{-\beta U(\mathbf{r})}}{\int d\mathbf{r} e^{-\beta U(\mathbf{r})}} \tag{6.4}$$

If we could choose our random evaluation points according to the probability density function $p(\mathbf{r})$, then our problem would be far simpler. For most observables $\mathcal{A}$, the phase points which would contribute most to the integral will be those where $p(\mathbf{r})$ is significant. Since part of $p(\mathbf{r})$ is one of the integrals we wish to calculate, this may seem unhelpful. Fortunately, an elegant solution to the problem exists, originally developed by Metropolis, et al.

We first approximate our phase space as being made up of a finite set of discrete points, $\{\mathbf{r}_1 \ldots \mathbf{r}_n\}$. Rather than generating a number of independent random points in phase space from this set, we will generate a *Markov chain* of evaluation points. Trial points in the Markov chain are not independent, but are generated with a probability which depends solely on the previous phase space point in the chain. This probability is generated through a fixed *transition matrix* π, such that if the ith point in our chain is $\mathbf{r}_i$, the probability that the next point is $\mathbf{r}_j$ is given by:

$$P(\mathbf{r}_j) = \pi_{ij} \tag{6.5}$$

We can see immediately that the matrix π must be a *stochastic matrix*, that is, the sum of any of its rows is one:

$$\sum_n \pi_{mn} = 1 \tag{6.6}$$

Now, we will randomly pick an initial point for our chain. If the probability that this will be any given point from our set is given by a vector $\rho^{(1)}$, then the equivalent probability vector for the second point in our chain will be given by:

$$\rho^{(2)} = \rho^{(1)}\pi \tag{6.7}$$

We can see that the probability vector for the third point in our chain will be given by:

$$\begin{aligned} \rho^{(3)} &= \rho^{(2)}\pi \\ &= \rho^{(1)}\pi^2 \end{aligned} \tag{6.8}$$

And by extension, the probability vector for the ith member of the chain will be given by:

$$\rho^{(i)} = \rho^{(1)}\pi^{i-1} \tag{6.9}$$

Over a large number of iterations the probability vector should tend to a limiting distribution ρ:

$$\rho = \lim_{i\to\infty} \rho^{(1)}\pi^{i-1} \tag{6.10}$$

This limiting distribution will be given by the solution to the eigenvalue problem:

$$\rho = \rho\pi \tag{6.11}$$

If there is only one such eigenvector, then our Markov chain is ergodic (that is, will explore the whole phase space), and this limiting distribution will be independent of the initial probability vector $\rho^{(1)}$. It can be shown that this will be so provided the transition matrix π is not only stochastic but irreducible.

To solve our problem, therefore, we can pick configurations (that is, points at which we evaluate our integrand) as a Markov chain with a transition matrix such that the limiting distribution will be given by equation 6.4. To make this easier, we take a stricter condition on ρ and π than equation 6.11, that of *detailed balance* (also known as *microscopic reversibility*):

$$\rho_m \pi_{mn} = \rho_n \pi_{nm} \tag{6.12}$$

This condition states that the probability of being in state $\mathbf{r}_m$ and the next state in the chain being $\mathbf{r}_n$ is the same as the probability of being in state $\mathbf{r}_n$ and the next state being state $\mathbf{r}_m$. It is a simple matter to show that a transition matrix and limiting distribution which fulfil this condition will also fulfil equation 6.11.

We will use a transition matrix which fulfils *Metropolis' Asymmetric Solution* for π. This is given by:

$$\pi_{mn} = \begin{cases} \alpha_{mn} & \rho_n \geq \rho_m \quad m \neq n \\ \alpha_{mn}\frac{\rho_n}{\rho_m} & \rho_n < \rho_m \quad m \neq n \\ 1 - \sum_{n \neq m} \pi_{mn} & \qquad\qquad\quad m = n \end{cases} \tag{6.13}$$

If the *underlying matrix* $\boldsymbol{\alpha}$ is symmetric, it is easy to show that this solution will fulfil detailed balance[1]. To give a stochastic transition matrix, $\boldsymbol{\alpha}$ should also be stochastic.

With given $\boldsymbol{\alpha}$, we can see that the dependence of π on ρ comes in only through the ratio $\frac{\rho_n}{\rho_m}$. Considering equation 6.4, we can see that by calculating the *ratio* of two such probabilities, we completely avoid having to calculate the configurational integral for the ensemble, and instead are left with a simple function of the energy of given configurations, a quantity which should be relatively easy to calculate:

$$\frac{\rho_n}{\rho_m} = e^{-\beta(U(\mathbf{r}_n)-U(\mathbf{r}_m))} \tag{6.14}$$

So, given a trial configuration n already generated from configuration m with probability according to the matrix α_{mn}, the probability of accepting that trial configuration as the next member of our chain is given by:

$$p_{mn} = \min\left(1, e^{-\beta \Delta U_{nm}}\right) \tag{6.15}$$

where the function $\min(x, y)$ returns the smaller of the two arguments and:

---

[1] Non-symmetric matrices can fulfil equation 6.12, or even just equation 6.11, but are not normally used.

$$\Delta U_{nm} = U(\mathbf{r}_n) - U(\mathbf{r}_m) \tag{6.16}$$

This cancellation of the configurational integral makes Metropolis Monte Carlo a feasible method. It also gives the method a major weakness; since the full configurational integral is never calculated, so our ensemble average will not be properly normalised. As long as our Markov chain of configurations passes through *most* of the region which significantly contributes to the ensemble average, our results will be good - that is, reasonably well normalised. If the Markov chain is not reasonably ergodic over the length of the simulation, however, our results will be less good. This weakness also means that such Monte Carlo integration is not a *direct* route to properties such as the full free energy, the entropy, or the chemical potential, whose calculation depends on knowledge of the full configurational integral.

6.1.3 The Metropolis Method

We now need to specify the underlying matrix, $\boldsymbol{\alpha}$. As such, we will consider a very simple implementation of the the Metropolis Monte Carlo method on a digital computer.

We consider a system specified in NVT in two dimensions. As such, we have N particles, whose positions (the $2N$ dimensions of the phase space) are specified by $2N$ variables held in the computer. These positions are constrained to remain within a square simulation volume, V, that is, they are constrained to remain within the range $\left(0 \ldots \sqrt{V}\right)$. We also specify the interaction between the particles, such that we can calculate the energy for any configuration $\mathbf{r}$, $U(\mathbf{r})$.

We begin with an initial configuration of these particles, $\mathbf{r}^{(1)}$. We must now pick the next member of the Markov chain; that is, the next configuration of particles. To do this, we randomly pick one of our N particles, whose coordinate we denote $\mathbf{r}_n^{(1)}$. We then apply a random displacement to that particle, generating a trial position for that particle $\mathbf{r}_n^{(1t)}$ and hence a new trial configuration $\mathbf{r}^{(1t)}$. This is done such that the particle has equal probability of ending up at any position within a square region $\mathcal{R}$ centred on that particle (see figure 6.1). This can be done by picking two random numbers from distributions uniformly distributed on the region $(-\delta r_{max} \ldots \delta r_{max})$, and adding these numbers to the the components of the particle position; this will give $\mathcal{R}$ a volume $4\delta r_{max}^2$. Since our positions are discrete in machine

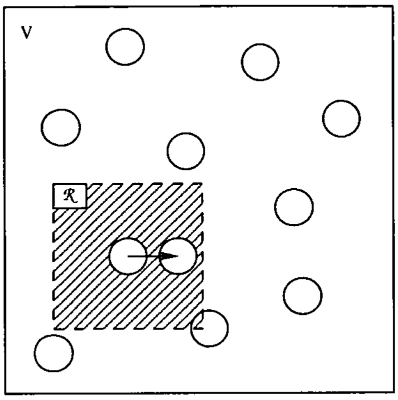

Figure 6.1: A new trial configuration is generated by moving a randomly selected particle with uniform probability to a position within the shaded region $\mathcal{R}$, which is a square with side length $2\delta r_{max}$.

representation, the probability of picking a given trial configuration $\mathbf{r}^{(1t)}$ is given by the matrix:

$$\begin{array}{rclccc} \alpha_{\mathbf{r}^{(1)}\mathbf{r}^{(1t)}} & = & 1/4\delta r_{max}^2 & \mathbf{r}_n^{(1t)} & \in & \mathcal{R} \\ \alpha_{\mathbf{r}^{(1)}\mathbf{r}^{(1t)}} & = & 0 & \mathbf{r}_n^{(1t)} & \notin & \mathcal{R} \end{array} \qquad (6.17)$$

This equation defines our underlying matrix $\boldsymbol{\alpha}$. To fully implement equation 6.13, we now calculate the energy for both configurations, $U(\mathbf{r}^{(1)})$ and $U(\mathbf{r}^{(1t)})$, and the difference between these energies, $\Delta U_{(\mathbf{r}^{(1t)})(\mathbf{r}^{(1)})}$ according to equation 6.16. Now, to follow equation 6.15, if ΔU is negative, (that is, $\rho_{\mathbf{r}^{(1t)}} \geq \rho_{\mathbf{r}^{(1)}}$), we *accept* our trial configuration $\mathbf{r}^{(1t)}$, that is, make it our new configuration, and next member of our Markov chain, $\mathbf{r}^{(2)}$. The probability of moving between two given states $\mathbf{r}_m$ and $\mathbf{r}_n$ with ΔU negative is α_{mn}, which was the probability of generating a given configuration $\mathbf{r}^{(1t)}$ in the first place.

If ΔU is *positive* ($\rho_{\mathbf{r}^{(1t)}} < \rho_{\mathbf{r}^{(1)}}$), then we accept the move with probability given by equation 6.14, that is, $e^{-\beta\Delta U}$. This fulfils the second part of equation 6.13. If the move is not accepted, we discard our trial configuration, and the next member of our chain is the same as the current member of our chain, $\mathbf{r}^{(2)} = \mathbf{r}^{(1)}$; this fulfils the final part of equation 6.13, accounting for the probability of remaining in the same state.

From here, we can continue generating our chain of configurations, by generating new *trial* configurations, comparing their energies, and either accepting them or rejecting them appropriately. We can record calculated observables from these configurations as we go along, and once we have generated sufficient configurations, estimate the ensemble averages for the observables

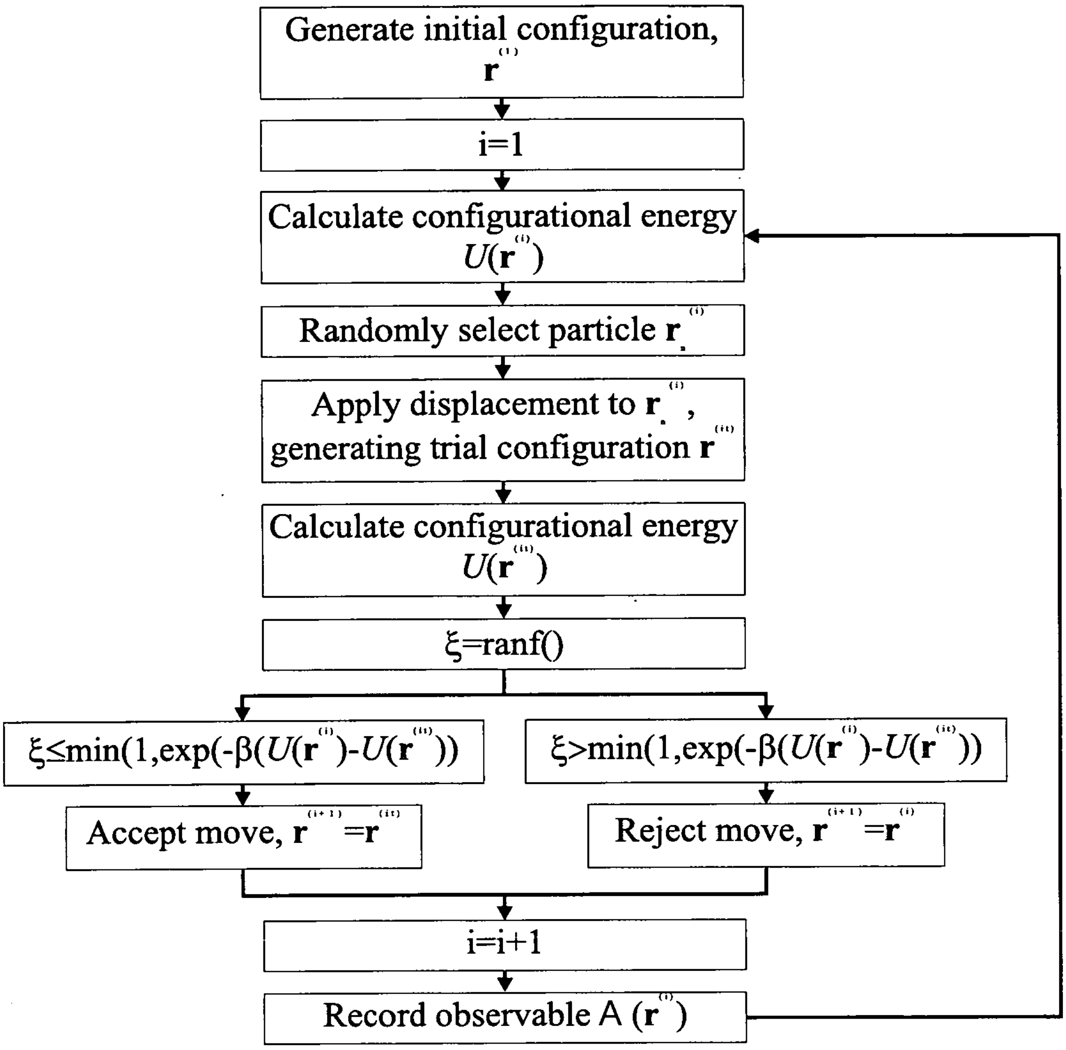

Figure 6.2: Flow chart describing basic NVT Monte Carlo algorithm.

as their mean calculated value. This algorithm is summed up as a flow chart in figure 6.2.

The algorithm described here is enough to create a complete "toy" Metropolis Monte Carlo program, easily generalised to three dimensions. All that is missing is a prescription for the value of the parameter δr_{max}, the maximum trial displacement along an axis for a particle. The size of this parameter has a direct impact on the efficiency of a Monte Carlo simulation. With large δr_{max}, particles can be displaced to essentially anywhere in the simulation box; as such, we begin to lose the advantages of importance sampling, with many moves rejected, and hence poor sampling of phase space. As δr_{max} becomes very small, most moves will make only a small difference to the energy of the system, and the rate of acceptance will become very high;

however, the new configurations will be only very slightly different to the old configurations, giving us very little new information. Once again, this leads to poor sampling. Conventional wisdom holds that δr_{max} should be adjusted such that the about 50% of moves attempts are accepted - this is normally done by adjusting δr_{max} over a set of Monte Carlo runs before actual sampling begins to take place. No proof that this gives the "best" results exists.

6.2 Implementation

We have described above the theory behind Monte Carlo simulation, and in principle, given enough detail to implement such simulations. As ever, though, there are a number of fiddly details to attend to, and a number of tricks, optimisations and approximations that will make our life easier, which we will discuss in this section.

Further, we have only described how to make these simulations work in the NVT ensemble, which has a number of disadvantages, not least that most actual experimental work is carried under conditions of fixed pressure and temperature. So we shall go on to describe how to work in the "open ensembles", that is, fixed NPT and μVT.

Finally, it is possible to gain much more than simple ensemble averages at a state point from Monte Carlo simulation. We will close this section by describing how we can process our results.

6.2.1 Real Simulations

Periodic Boundaries and the Minimum Image Convention

Even on the most advanced of modern digital computers, it is not possible to perform simulations at anything like the order of magnitude of size of the thermodynamic limit. Nor will this be possible in the foreseeable future. At most, we can only simulate systems with N of a few tens of thousands, and normally we will be dealing with thousands or even hundreds of particles. This will introduce serious *finite size effects* into our work. Further, we have not yet dealt with how the boundary conditions on our simulation box should work.

The first part of the standard solution to these problems is that of *periodic boundary conditions.* We will fool our system into believing that it is part of an infinite system by tessellating our simulation volume across space, as shown in figure 6.3. Just as the box is repeated across

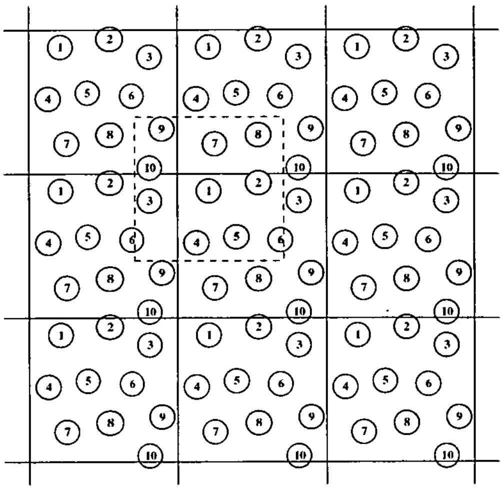

Figure 6.3: Periodic boundary conditions and the minimum image convention. The central box is the simulation box; this is repeated across space to imitate an infinite system. Rather than calculating interactions with an infinite number of image particles, a particle will only interact with the nearest images of other particles; for instance, the shaded particle labelled '1' will only interact with particles within the dashed box.

space, so are its contents, as "periodic image" particles. The box has no walls, either, with particles interacting and moving freely across the notional boundaries; if a Monte Carlo step displaces a particle through a face and out of the central box, then it will merely reappear through the opposite face. As such, we need only store the coordinates of the particles in the central box, as it is a simple matter to calculate the coordinates of their periodic images.

For this system to be a good imitation of a "true" infinite system, neither individual particles nor the system as a whole must be able to "notice" this imposed periodicity. For individual particles, this requires that the interaction energy between a particle and its periodic images must be negligible - that is, the effective range of the interparticle potential must be less than half the width of the simulation box. For "long-range" potentials[2], the interaction between particle images can remain significant; various methods have been devised to deal with such systems [71]. Such potentials are not studied in this work, however; over system sizes of order greater than a hundred particles, the influence of periodic boundaries on individual particle interactions should be minimal.

More of a problem is the occurrence of long-wavelength fluctuations in the system. The enforced periodicity will obviously restrict the available phonon wave-vectors. If a system has a

---

[2] Long range particles are defined as those in which the interaction falls off no faster than r^{-d}, where d is the dimensionality of the system.

correlation length longer than half the box length (as will occur on approach to critical points or any other second-order transition, where correlation length diverges), this will introduce problems.

In general, though, periodic boundary conditions give a good approximation to full thermodynamic systems for reasonably large system sizes, and the presence of finite size effects can be checked for by repeating simulations at larger system sizes and comparing the results.

Given our new ersatz infinite system, which we represent using a finite number of particle positions, we must now calculate the total energy using a finite number of calculations. We should calculate the interaction between every one of our N particles and every other particle, including images. This is obviously unfeasible, as there are an infinite number of images. We have already noted, however, that for the potentials we will be using here the effective range should be less than the width of the simulation box. So we will approximate by calculating only the interactions of a particle with the $N-1$ closest normal or image particles within a region the same size and shape as the simulation box, but centred on the particle in question. This *minimum image convention* is illustrated in figure 6.3.

Potential Cutoffs and Cell Structures

We can take the idea behind the minimum image convention even further. We can approximate a given pairwise potential by saying that, beyond a *cutoff range* r_c, the interaction between particles is as good as zero, and as such we will only need to calculate interactions between particles separated by $r < r_c$, that is, within a spherical (or circular) region radius r_c. Since calculating the potential is often computationally expensive, this should result in an appreciable saving of computer time for most systems.

Such truncation does effect the results from a simulation. Methods exist to counter this, though not perfectly, for example by approximating liquid systems as perfectly homogeneous outside the cutoff radius. The errors introduced by a well chosen potential cutoff of sufficient range should only change the results in quantitative detail, rather than in general behaviour.

For systems where the simulation box length is much larger than $2r_c$, and where the number density is reasonably high, further savings in computer time can be made by using a cell list structure. Using a cutoff, it is still necessary to calculate distances to all $N-1$ other particles in the system, then compare against the cutoff range; computational time for calculating a

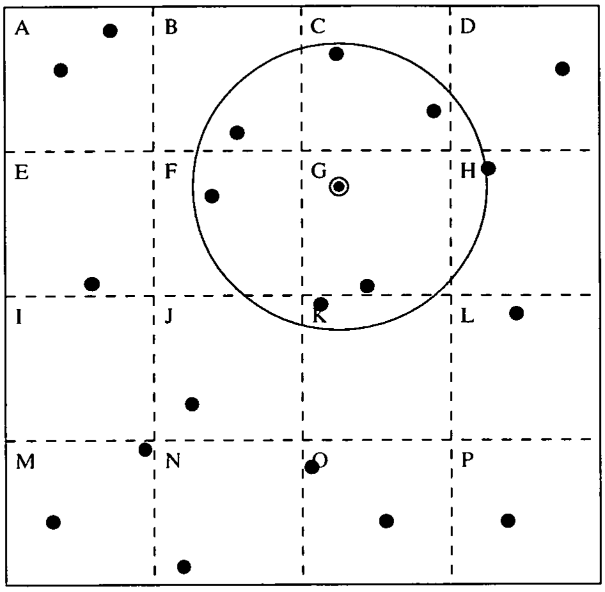

Figure 6.4: With a potential cutoff, the highlighted particle will only interact with particles within the circle, though distances to all particles must be still be calculated. Using a cell structure, only distances to particles within the filled cells need to be calculated.

pairwise interaction will still scale as N^2. To counter this, we can divide the simulation box into a number of sub-boxes (known as *cells*) with side length at least equal to r_c, and maintain lists of which particle occupies which cell. We then only need to calculate interactions between a particle and those particles in the same or neighbouring cells (see figure 6.4) . This algorithm will scale as N (collation of the lists is order N, and at given density, the number of interactions to be calculated will be constant), making it very efficient; however, the large amount of extra book keeping necessary will make this method comparatively slow for small system sizes.

6.2.2 Monte Carlo in Open Ensembles

Now that we have discussed how to effectively and efficiently perform NVT Monte Carlo simulations, we will turn to Monte Carlo in other ensembles, specifically the open ensembles, constant NPT (isothermal-isobaric) and constant μVT (grand canonical).

Before this, though, we will briefly ask why should we want to use these ensembles? Consider performing simulations in the NVT ensemble on a system capable of exhibiting two-phase coexistence. As long as we remain in the single-phase regions, we will be fine. As soon as we reach a state point in the two-phase coexistence region, however, we will find problems. At such a point, the system will want to phase separate, and at a large enough system size, would happily do so. However, in a small simulated system, it may well be unable to. This is because an interface must form between the coexisting phases. This interfacial region will have a very large free energy per particle; in an infinite system, this will have an infinitesimal contribution to the full free energy, but in our simulation (where the interface is repeated off into infinity by the periodic boundary conditions), it will make a very large and prohibitive contribution. Thus, NVT simulations of first order phase transitions are very difficult, and are dogged by metastability and finite size effects.

Consider instead simulating the same system using an open ensemble. At every point except the exact coexistence point, there is only a single thermodynamically stable phase. An open ensemble should be free to vary its size (volume for NPT, particle number for μVT) until its configuration is entirely in the phase of lowest Gibbs free energy. Of course, things are not this simple; on passing across the transition, the configurations sampled by an open ensemble must still pass through interfacial states, and will also suffer from metastability and finite size effects. These effects will not be so harsh as they are in the NVT ensemble, however, and methods exist for getting around them (see section 6.3).

NPT Monte Carlo

Working in the isothermal-isobaric ensemble has the advantage that most experimental work is carried out under conditions of constant pressure and temperature; hence NPT ensemble Monte Carlo allows for direct comparison with experimental results.

Since an NPT ensemble system will not have fixed volume, it is convenient to introduce the concept of *scaled coordinates* for the particles. We assume a square (cubic) box of side $L = V^{-1/d}$, though the method is easy to generalise. Particle positions are now determined by the set of scaled coordinates $\mathbf{s}$, such that:

$$\mathbf{r}_i = L\mathbf{s}_i \tag{6.18}$$

We can now write ensemble averages as:

$$\langle \mathcal{A} \rangle_{NPT} = \frac{\int dV e^{-\beta PV} V^N \int d\mathbf{s} \mathcal{A}(\mathbf{s}) e^{-\beta U(\mathbf{s};L)}}{\int dV e^{-\beta PV} V^N \int d\mathbf{s} e^{-\beta U(\mathbf{s};L)}} \tag{6.19}$$

The factor V^N has come about due to the change in integration variable from $\mathbf{r}$ to $\mathbf{s}$. In our Monte Carlo procedure, we will be making moves which alter V. This gives us a limiting distribution of:

$$\rho_{NPT} \propto e^{-\beta(PV+U(\mathbf{s};L))+N\ln V} \tag{6.20}$$

Rather than working in V, where checks must be in place against moving to unphysical negative volume, it is more convenient to work in $\ln V$. Making the change in variable in equation 6.19, we have ensemble averages given by:

$$\langle\mathcal{A}\rangle_{NPT} = \frac{\int Vd\ln Ve^{-\beta PV}V^N\int d\mathbf{s}\mathcal{A}(\mathbf{s})e^{-\beta U(\mathbf{s};L)}}{\int Vd\ln Ve^{-\beta PV}V^N\int d\mathbf{s}e^{-\beta U(\mathbf{s};L)}} \tag{6.21}$$

The limiting distribution function for our Markov chain will now be given by:

$$\rho_{NPT} \propto e^{(-\beta(PV+U(\mathbf{s};L)))+(N+1)\ln V} \tag{6.22}$$

We will now specify two types of move to generate trial configurations. The first moves particles in s space, and works as NVT Monte Carlo, that is, a particle i is picked at random, and a displacement applied such that:

$$\mathbf{s}_i^{(t)} = \mathbf{s}_i + \delta s_{max}\left(\boldsymbol{\xi} - 1\right) \tag{6.23}$$

where $\boldsymbol{\xi}$ is a vector with components that are random numbers uniform over the range $(0\ldots1)$. The second move changes V such that:

$$\ln V^{(t)} = \ln V + \delta\left(\ln V_{max}\right)\left(\xi - 1\right) \tag{6.24}$$

where ξ is a random number uniform on $(0\ldots1)$. Changes in V will be introduced through changes in L, which alter the particle positions $\mathbf{r}$ whilst preserving scaled coordinates $\mathbf{s}$.

As before, trial moves are accepted with a probability equal to the ratio of the unnormalised probabilities ρ_{NPT} between original configuration m and trial configuration n. To this end, we calculate the quantity ΔH:

$$\Delta H_{nm} = \Delta U_{nm} + P(V_n - V_m) - (N+1)\beta^{-1} \ln \left(V_n / V_m\right) \tag{6.25}$$

and accept or reject moves with probability:

$$p_{nm} = \min\left(1, e^{-\beta \Delta H_{nm}}\right) \tag{6.26}$$

In the case of s-space moves (ie no change in V), this reduces to the same acceptance probability as equation 6.15.

Particle displacement moves are generally attempted with N times the frequency of volume moves, and the parameter $\delta\left(\ln V_{max}\right)$ is generally chosen to yield $30 - 50\%$ move attempt acceptance. Once again, these are "rules of thumb" without a rigorous basis.

Periodic boundaries and potential cutoffs work here as in the NVT ensemble. Cell structures can also be applied, but the cell lists should be recalculated after every volume move, with the cell box length being recalculated.

μVT Ensemble

Performing Monte Carlo simulation at constant chemical potential may at first seem somewhat odd, as μ is not a natural variable for experiment. However, this ensemble gives us certain unique advantages, though it is rather constrained in its range of application.

The grand canonical ensemble allows fluctuation of particle number N at constant volume. We will allow for this by putting our system in equilibrium with a hypothetical infinite ideal gas system of particles of the same type, and exchanging particles between the systems. Our hypothetical system will have volume $V_0 \approx \infty$; to manage exchanges, we retain the scaled coordinate system from the NPT ensemble, with particles retaining their $\mathbf{s}_i$ coordinate between systems. Since V_0 is so enormous, of course, particles in the hypothetical system will be effectively non-interacting, and this system need not be modelled; the scaled coordinate representation is necessary to ensure detailed balance.

With this representation, an ensemble average is given by:

$$\langle\mathcal{A}\rangle = \frac{\sum\limits_{N=0}^{\infty} (N!)^{-1} V^N \Lambda^{-dN} e^{\beta\mu N} \int d\mathbf{s}\mathcal{A}(\mathbf{s}) e^{-\beta U(\mathbf{s})}}{\sum_{N=0}^{\infty} (N!)^{-1} V^N \Lambda^{-dN} e^{\beta\mu N} \int d\mathbf{s}(\mathbf{s}) e^{-\beta U(\mathbf{s})}} \tag{6.27}$$

Λ is the thermal de Broglie wavelength for the particles; this is taken as unity through convenient choice of unit. From this, we are seeking from our algorithm a limiting distribution function given by:

$$\rho_{\mu VT} \propto e^{-\beta(U(\mathbf{s})-N\mu)-\ln N!-dN\ln\Lambda+N\ln V} \tag{6.28}$$

Once again, we will make two kinds of move. The first will sample $\mathbf{s}$ space; it should come as no surprise that this is carried out exactly as for NVT and NPT Monte Carlo, with random displacements applied to randomly chosen particles. The second will move through particle number, mimicking particle exchange with the ideal gas system. Particle number moves are split into two possible types; "creation" moves (effectively taking a particle from the ideal gas into the system of interest), and "destruction" moves (moving a particle from the studied system into the ideal gas system).

In a creation move, the trial configuration is generated by placing a new particle at a random location chosen uniformly from the simulation volume. The energy for this trial configuration is evaluated, and a *creation factor* C_{nm} calculated:

$$e^{-\beta C_{nm}} = \frac{V}{\Lambda^d(N+1)} e^{\beta(\mu-\Delta U_{nm})} \tag{6.29}$$

Such a configuration is accepted with probability given by:

$$p_{nm} = \min\left(1, e^{-\beta C_{nm}}\right) \tag{6.30}$$

In a destruction move, a random particle is picked from the simulation volume, and the trial configuration is made by deleting it. From this, the *destruction factor* D_{nm} is calculated:

$$e^{-\beta D_{nm}} = \frac{\Lambda^d N}{V} e^{-\beta(\mu+\Delta U_{nm})} \tag{6.31}$$

This trial configuration is accepted with probability:

$$p_{nm} = \min\left(1, e^{-\beta D_{nm}}\right) \tag{6.32}$$

To preserve detailed balance, creation moves and destruction moves *must* be attempted with equal probability. Any probability ratio between creation/destruction moves and displacement moves is legal, but simulation lore has it that an equal probability for attempts to create, destroy, and displace particles gives the most efficient simulations. Once again, this is only a rule of thumb.

Grand canonical Monte Carlo is more tricky programming-wise than working in the NVT and NPT ensembles. In the fixed-N ensembles, particle positions can be stored in a fixed-length array. In μVT work, the length of array necessary can fluctuate considerably. One method to work around this is to use a fixed length array of length much greater than the expected $\langle N \rangle$ [71]. Use of non-fixed arrays in languages like C and of dynamic linked list structures are also possible; though in principle these should be less computationally efficient, many modern compilers are capable of optimising such algorithms.

The main reason for using μVT Monte Carlo is that it can directly evaluate the free energy of a system. We have seen that normally Monte Carlo integration cannot do this; it will only ever give unnormalised partition functions, giving an unknown additive constant to the free energy. In this algorithm, however, we have set up the system with a known (indeed, preset) chemical potential for particle exchange with an ideal gas particle reservoir. Since the free energy of an ideal gas can be calculated directly, the full free energy of our system can be calculated [84].

Unfortunately, the range of application for grand canonical Monte Carlo is limited by its reliance on particle insertion moves. In a dense liquid, most particle insertion attempts will be rejected, due to large overlap between particle cores. After a particle deletion, a hole will be left; it may take a long time for displacement moves to allow the system to respond to this, and following particle insertions may well merely put a particle back into this hole. As such, the algorithm will explore phase space very slowly. Methods exist to alleviate this [86, 85], though not completely. The situation is even worse for crystalline solids; particle insertions will, in general, only be accepted at empty lattice points, which are themselves unusual defects, and particle deletions, which would create such defects, are likely to be rejected. As such, μVT

Monte Carlo study of bulk phases is limited to low to moderate density fluids.

6.2.3 Processing the Results

Recording Observables

Each of the ensembles we have mentioned includes an obvious observable to measure from Monte Carlo simulation. In NVT Monte Carlo, this is the energy; since this has to be measured for every configuration generated, it takes little effort to record. In NPT Monte Carlo work, both volume and energy are calculated and can be recorded, whilst in the μVT ensemble, the readily accessible observables are particle number and energy. It is unnecessary (and indeed uneconomic in terms of storage space) to record these observables after every move attempt, since such data will be strongly correlated, with each point yielding little extra information; instead, data should be recorded at regularly spaced intervals throughout the simulation run.

It can be useful to collect certain other information from a simulation run. A good example is the pair distribution function, $g(r)$. This is to simulation what its Fourier transform, the structure factor $s(k)$, is to experiment; that is, the best source of information on structure, since whilst "snapshot" configurations from simulations can be very helpful for visualisation purposes, there is no real way of telling if a given configuration is "typical" or not.

The function $g(r)$ measures the probability of observing a pair of particles having separation r. It is measured in simulation by evaluating all the pair separations in the system at intervals through the simulation, and compiling this data in histogram bins (normally stored in the computer as an array), then performing the appropriate normalisation [71].

Another useful quantity which can be measured for pairwise additive potentials is the pressure. To measure this, we must take an ensemble average of the "internal virial function" $\mathcal{W}(r)$, given by:

$$\mathcal{W} = -\frac{1}{d}\sum_{i}\sum_{i<j} r_{ij}\frac{d\phi(r_{ij})}{dr_{ij}} \tag{6.33}$$

This function is susceptible to problems with potential cutoffs, which can be corrected for in the same way as for energy measurements. If this data is recorded over the simulation run, then the ensemble average pressure is given by:

$$\langle \mathcal{P} \rangle = \frac{N}{V}\beta^{-1} + \frac{1}{V}\langle \mathcal{W} \rangle \tag{6.34}$$

If the ensemble is such that either volume or particle number vary, then the appropriate quantities must also be measured as ensemble averages. In all ensembles, this average should give the pressure; this may seem pointless for the NPT ensemble, but is a good exercise as a consistency check.

As well as calculating the averages of observed variables, the variances of these averages also hold useful data. It is possible to use these to calculate response functions [6] such as the isothermal compressibility K_T and the specific heats from our simulation data. The exact method varies across ensembles; whilst ensemble averages are equivalent across ensembles, the fluctuations do vary (as an example, consider that volume fluctuations are zero in the NVT ensemble whilst non-zero in the NPT ensemble). A good list of formulae for calculating these quantities in different ensembles can be found in Allen and Tildesley's book [71].

Error Estimation

Assuming that our Monte Carlo run has been infinitely long in a completely ergodic system, then our results will be "exact". However, since most researchers do not have access to infinitely powerful computers, or infinitely long research grants, our results will normally be susceptible to statistical errors; that is, the distribution we sample will be an approximation to the "exact" result. As such, we must attempt to estimate this error.

Our individual recorded data points will, in general, not be independent. The data will have a correlation length, τ_c^A, the characteristic decay time of the autocorrelation function for the observable $\mathcal{A}$ through the simulation run. If we can calculate this length for a run with τ data points, then the variance in the mean $\langle \mathcal{A} \rangle$ that we measure is given by:

$$\sigma^2\left(\langle \mathcal{A} \rangle\right) = \frac{\tau_c^A}{\tau^2}\sum_{\tau}\left(\mathcal{A} - \langle \mathcal{A} \rangle\right)^2 \tag{6.35}$$

This is a standard statistical result. Since the correlation length is often costly to calculate, however, it is standard practise in simulation to calculate error using *block averages*. For this, the simulation data is divided into n_b blocks, each length $\tau_b = \tau/n_b$. The ensemble average of $\mathcal{A}$ over each block, $\langle\mathcal{A}\rangle_b$, is then calculated. The variance of these block averages can then calculated:

$$\sigma^2\left(\langle\mathcal{A}\rangle_b\right) \approx \frac{1}{n_b}\sum_{b=1}^{n_b}\left(\langle\mathcal{A}\rangle_b - \langle\mathcal{A}\rangle\right)^2 \tag{6.36}$$

It can be shown that this error estimator should be inversely proportional to n_b if τ_b is large enough that the blocks become uncorrelated. As such, we can estimate the error in our results through:

$$\sigma^2\left(\langle\mathcal{A}\rangle\right) = \frac{\sigma^2\left(\langle\mathcal{A}\rangle_b\right)}{n_b} \tag{6.37}$$

This quantity should be calculated for a range of n_b with the actual error estimate being taken from a region where it appears to be approaching a constant.

Single Histogram Extrapolation

Histogram extrapolation is a powerful tool which allows us to extend the results from a simulation at a single state point to give information on the surrounding region of phase space. Whilst the ideas behind it are old, they were popularised through the work of Ferrenberg and Swendsen [87].

To demonstrate the concept, let us consider the probability of observing a system in the canonical ensemble with configurational energy E at state point $\beta = 1/T$, $p(E;\beta)$. We can write this in terms of the density of states, $\Omega(E)$:

$$p(E;\beta) = \frac{\Omega(E)e^{-\beta E}}{Z(\beta)} \tag{6.38}$$

with $Z(\beta)$ the partition function, given in terms of the density of states by:

$$Z(\beta) = \sum_{E'}\Omega(E')e^{-\beta E'} \tag{6.39}$$

We will now rearrange this to get a form for the density of states:

$$\Omega(E) = Z(\beta)p(E;\beta)e^{\beta E} \tag{6.40}$$

Now consider the probability distribution at another state point $\beta' = 1/T'$:

$$p(E;\beta') = \frac{\Omega(E)e^{-\beta' E}}{Z(\beta')} \tag{6.41}$$

and substitute in equation 6.40:

$$p(E;\beta') = \frac{p(E;\beta)e^{-(\beta'-\beta)E}}{\sum_{E'} p(E';\beta)e^{-(\beta'-\beta)E}} \tag{6.42}$$

The partition functions here have cancelled. This shows that, given *only* the function $p(E)$ at a single state point β, we can calculate the same function at *any* other state point; this process is known as *reweighting*. The argument is easy to generalise to other ensembles; for instance, in the NPT ensemble, the probability distribution becomes $p(E,V;\beta,P)$ and the density of states $\Omega(E,V)$ to give the result:

$$p(E,V;\beta',P) = \frac{p(E,V;\beta,P)e^{-(\beta'-\beta)(E+(P'-P)V)}}{\sum_{E',V'} p(E',V';\beta,P)e^{-(\beta'-\beta)(E+(P'-P)V)}} \tag{6.43}$$

and equivalently for the μVT ensemble in N and E.

We do not have access to the full functions $p(E...)$, but we can bin the results from our simulations into histograms, $h(E...)$. These histograms provide estimates proportional to $p(E...)$, and can be reweighted just as above. These can be used in the same way to give us estimates of the distributions for the variables at other state points, giving us access to their ensemble averages and fluctuations. The errors in the reweighted histograms are measured using block averaging in the same way as the straight up simulation results, remembering to weight each data point's contribution appropriately.

Since our measured histograms are not the full probability distribution, however, we cannot extend the results of one simulation across all phase space. This manifests in several ways.

First, our simulation results suffer from statistical errors. Histogram reweighting preserves the fractional error in a histogram, rather than the absolute error. Our simulation results may have uniformly small absolute error in $h(E;T)$, but the fractional error will be small at the peak of the distribution, and very large in the tails. If we reweight to a state point where the peak of the new distribution is at an energy in the tail of the old distribution, then that peak will suffer from very large fractional and absolute error.

Secondly, our simulations only sample a range of each observable. Consider an NVT simulation which has not visited points with $E < E_L$. In this case, the estimated histogram is zero for $E < E_L$ ($h(E < E_L; T) = 0$), whilst the actual distribution, $p(E < E_L; T)$, will be very small but still non-zero. Now consider reweighting the histogram to a state point T' where $p(E < E_L; T')$ is significant; we can see from equation 6.42 that $h(E < E_L; T')$ will be zero.

Finally, we discretise the density of states for our system by using histogram bins. We must ensure that the width of these bins is not so much that we miss fine detail which may be present in the function $p(E...)$. This problem is not as crippling as the previous two; it can be solved by performing the reweighting again with smaller bin sizes, whilst the previous two problems are due to an inherent problem, incomplete sampling by the Monte Carlo algorithm.

The first two drawbacks limit single histogram extrapolation to a limited region of phase space surrounding the original state point. Even so, it is a useful tool. As an example, for our problem at hand, we could find a point of compressibility maximum on an isotherm by performing a large number of simulations to an ever-greater number of decimal places in T according to some extrema-seeking algorithm until we achieved the desired accuracy. It would be far quicker, however, to perform a single simulation near to the estimated maximum, then use repeated histogram reweighting to find the maximum.

Another common use for histogram extrapolation is to locate coexistence points to arbitrary precision in a similar way. We will return to this in the next section.

Multiple Histogram Extrapolation

This extension to histogram extrapolation [88, 89] allows us to combine simulation data gathered at several state points. This can help us with problems due to poor sampling; we can combine simulations which individually do not sample the full variable range of interest, but taken together do.

When combining histograms in this manner, the normalisation of the histograms will be different for each simulation. Each histogram is normalised by a quantity proportional to the full partition function, but this constant of proportionality is unknown and different for each simulation. Thus the derivation for the multiple histogram extrapolation method is much more complicated than the single histogram method given above, using an iterative method to establish the ratios of these constants of proportionality - that is, the logarithm of the free energy differences between the state points - before combining them. For a full discussion of this method, see reference [89].

6.3 Dealing with Coexistence

Consider the order parameter distribution function for a system near two-phase coexistence, $p_{coex}(\mathcal{A})$. This will have a double-peaked structure, with the peaks reflecting the order parameter distributions for the two phases. Exactly at coexistence, the free energies of the phases will be equal, therefore the probabilities of observing each phase will be equal, and hence the weight under each peak will be equal.

Now, consider performing a Monte Carlo simulation at such a point. To sample both phases, the simulation must pass through states with order parameter values in the trough between the peaks. These states are mixtures of the two phases, and will therefore contain interfaces. If the transition is suitably weak (for instance, near a critical point), the two phases will be very similar, and the free energy cost of the structural mismatch at these interfaces will be low. As such, there will still be a reasonable probability of observing such interfacial states, and a Monte Carlo simulation run should be able to pass back and forth through such states with relative ease. This will result in good sampling of the relative weights of the phases, and histogram reweighting can be used to find the exact coexistence point according to the equal weight criterion.

Unfortunately, in general the two phases are more likely to be structurally very different, and the free energy of the interfacial states will be very high. This creates a high free energy barrier between the phases, resulting in a deep probability trough between peaks. At best, the simulation will cross this barrier only rarely, and poorly sample the relative weights of each phase. At worst, the simulation will not pass across the barrier over any reasonable run time, and become "stuck" in one phase or the other.

To effectively simulate coexistence, we must overcome this difficulty. One method is that of "extended sampling". In this, rather than sampling from the Boltzmann distribution, we use a distribution where there is much less trouble crossing the interfacial states. We must then use some method to find what our results would have been if we had used the Boltzmann distribution. Extended sampling comes in many flavours and goes under many names; the particular formalism we will explain and use here is that of "multicanonical sampling" [91, 92].

The second method is to construct our simulation so as to avoid the problematic interfacial configurations altogether. Direct simulation methods of this type include Gibbs Ensemble Monte Carlo (a clever method for simulating coexisting fluid phases - see reference [90]), and the recently-proposed Lattice Switch Monte Carlo [96, 97, 98], which is developed explicitly for coexisting crystalline phases, and which we shall describe here.

Finally, we can completely avoid two-phase simulation, pursuing instead single-phase simulations of the phases of interest. The methods of thermodynamic integration can be used to calculate the free energy difference of a simulated system with respect to another system of known free energy (for instance, an ideal gas or Einstein crystal) through numeric integration of free energy derivatives. By performing this for two phases, it is technically possible to find coexistence directly by equating pressure, chemical potential and Gibbs free energy. Such methods have met with some success; however, if the overall free energies (or their associated errors) are large compared to the characteristic free energy difference between the phases, it will be difficult to estimate coexistence points to any precision. If we are given one or more pre-determined point on the coexistence line, however, we can use the method of Gibbs-Duhem integration [102], which uses single-phase simulations to numerically integrate the Clausius-Clapeyron equation, giving us a path of constant free energy difference through the phase diagram.

A good review of methods for simulating coexistence between fluid phases can be found in reference [94].

6.3.1 Multicanonical Reweighting

The idea of multicanonical reweighting is to alter our sampling to an arbitrary distribution of our choice, usually to pass through regions of high free energy (such as in the above example of phase coexistence), or to better sample those hard-to-reach yet important values of some order parameter (see the section on Lattice Switch Monte Carlo below).

We will denote this (as yet arbitrary) multicanonical sampling distribution $p_{MC}(\mathcal{A})$. Without loss of generality, we can write this function in terms of the appropriate ensemble distribution, $p(\mathcal{A})$:

$$p_{MC}(\mathcal{A}) \propto e^{\eta(\mathcal{A})} p(\mathcal{A}) \tag{6.44}$$

Here, $\eta(\mathcal{A})$ is a "weight function", which can be seen as biasing the normal Boltzmann sampling to the required distribution.

We now move to considering this for a general ensemble to the NVT ensemble; generalisation back is a simple matter. In this ensemble, we have:

$$p_{MC}(E) \propto \frac{e^{-\beta E} e^{\eta(E)}}{Z(\beta)} \tag{6.45}$$

Extension of Monte Carlo move acceptance probabilities to sample this distribution is simple; in NVT work, equation 6.15 becomes:

$$p_{mn} = \min\left(1, e^{-\beta\Delta U_{nm}+(\eta_n-\eta_m)}\right) \tag{6.46}$$

Similarly, calculation of the histograms and averages which would have been sampled under the Boltzmann distribution is easy to implement, with contributions from a given simulation data point being weighted by $e^{-\eta(U)}$ in the appropriate calculations.

We must now decide on the sampling distribution p_{MC} that we want. The usual choice is to sample the region of interest uniformly; from equation 6.45, we can see that for this we must set our weights such that:

$$e^{-\eta(E)} \propto p(E) \tag{6.47}$$

Of course, the problem here is that $p(E)$ is the quantity we wish to find in the first place. All is not lost; we do not require strictly uniform sampling, merely approximately uniform sampling. As such, we can plug an approximation to $p(E)$ into equation 6.47, which should at make our sampling more uniform.

Use of multicanonical simulation is usually an iterative process. An initial run at the state point is performed. The histogram $h_0(E)$ for this state point is used as an estimator for $p(E)$, and used to find a multicanonical weight function through equation 6.47. A second run is then performed using this weight function; this should improve the sampling. The new histogram $h_1(E)$ is then used to produce a more refined weight function, and the process repeated until a simulation samples the required region of phase space with the required uniformity. This simple method is known as the "visited states" method. Fixes to this and alternative methods exist

[92]. It should be appreciated that the method used to estimate the weight functions is not important, as long it produces the desired uniformity of sampling. How to gain a good weight function is to a degree "voodoo", in that one must rely heavily on physical intuition rather than using a set, systematic strategy.

Multicanonical sampling has achieved great success in simulation of coexistence, especially between fluid phases and around critical points [93, 94, 95]. Liquid-gas coexistence in particular is well-suited to this method - by starting near the critical point, where the free energy barrier is neither particularly wide nor deep, a good weight function can be found with relative ease. Histogram reweighting can then be used to find the appropriate weight functions at steps further back along the coexistence line, where the depth and width of the free energy barrier would make a fresh weight function prohibitively computationally expensive to evaluate.

6.3.2 Lattice Switch Monte Carlo

Coexistence between phases with different symmetries can give even extended sampling methods troubles. A good example is coexistence between solid phases with different lattices, where the free energy barrier between phases will be far too high to estimate as a weight function in reasonable time. Further, this will be the case along the whole length of the transition line; for such transitions, there can be no critical point near which the transition is weak enough to evaluate a weight function which can then be reweighted. A very recent solution to this problem is the method of Lattice Switch Monte Carlo [96, 97, 98], which avoids simulating two-phase configurations altogether.

This method assumes that, over the length of the simulations to be performed, there is negligible chance of one phase transforming into the other. This allows us to separate the phase space into two regions, which we denote through the discrete variable $\alpha = \{0, 1\}$, separated by an effectively infinite free energy barrier. Single-phase simulations can give us the configurational integrals associated with each of these regions, Z_α, up to a multiplicative constant; the problem is to couple simulations of each phase so as to equate these constants, which will allow calculation of the free energy difference.

For lattice phases, we use the phase label α as the order parameter for the transition. We add to our Monte Carlo algorithm to allow moves in this parameter - that is, moves which take us between configurations characteristic of both phases. We decompose particle positions in a similar way to that used in the harmonic approximation (see chapter 4). In the simplest form of lattice switch, particle positions are now given by:

$$\mathbf{r}_i = \mathbf{R}_i^{\alpha} + \mathbf{u}_i \tag{6.48}$$

There are now two sets of lattice vectors $\mathbf{R}_i^{\alpha}$, one for each lattice phase. These represent the ground-state positions of particles in lattice phase α. The displacement vectors $\mathbf{u}_i$ are as in the harmonic approximation, and are independent of α. Unlike the harmonic approximation, it does now matter which lattice position we index to which particle. We should choose indices in each phase such that, on switching the label α, we maintain as many particle neighbours as possible.

We can now add a "lattice switch move" to the NVT ensemble Monte Carlo algorithm. Part of our description of the current configuration m is the phase label $\alpha = \alpha_m$; we generate a trial configuration n by $\alpha_n = \mathrm{NOT}(\alpha_m)$. The probability of accepting this trial configuration is as equation 6.15.

This is unfortunately not enough to make a working lattice switch algorithm. In general, displacement vectors typical in one phase will not be typical in another, and so performing this switch will usually change a perfectly acceptable configuration in one phase into a configuration with considerable overlap of particle cores in the other phase. This means that the quantity ΔU_{nm} from equation 6.15 will normally be large and positive, and lattice switch moves between such configurations will be accepted only rarely. There will only be a small subset of configurations for which ΔU_{nm} is small or negative; these "gateway configurations" will in general be those where all particles lie close to their lattice positions.

We must, therefore, enhance the probability of the simulation visiting these gateway configurations. We have already discussed a good tool for this - multicanonical reweighting. We must gather estimators for the probability distribution function, $p(\Delta U)$ (where ΔU is the change in energy which would result from a hypothetical lattice switch move) for both phases, and use them as weight functions to ensure that our simulations sample in ΔU reasonably uniformly. This will allow regular sampling of gateway configurations, and hence allow our simulation to perform regular successful lattice switch moves, sampling both phases well without ever passing through two-phase configurations.

This method can be extended to isothermal-isobaric Monte Carlo. First, we must move to scaled coordinates, such that:

$$\mathbf{r}_i = L\mathbf{B}^{\alpha}\left(\mathbf{R}_i^{\alpha} + \mathbf{s}_i\right) \tag{6.49}$$

Here, we have introduced the $d \times d$ matrices $\mathbf{B}^{\alpha}$. These are chosen according to two criteria. First, since our two phases may have different volumes, these matrices are chosen such that:

$$\frac{|\mathbf{B}^0|}{|\mathbf{B}^1|} = \frac{\langle V^0 \rangle}{\langle V^1 \rangle} \tag{6.50}$$

with $\langle V^{\alpha} \rangle$ as the ensemble average volume for phase α, evaluated using a brief single-phase simulation.

Secondly, the two phases may not both be commensurate with the same shape simulation boxes. The matrix $\mathbf{B}^{\alpha}$ defines the shape of the simulation box to be used for phase α. Given a two dimensional $\mathbf{B}$ matrix:

$$\mathbf{B} = \begin{pmatrix} B_{xx} & B_{xy} \\ B_{yx} & B_{yy} \end{pmatrix} \tag{6.51}$$

the simulation box will be a parallelogram with sides formed by vectors (LB_{xx}, LB_{yx}) and (LB_{xy}, LB_{yy}). If, for simplicity, we use $\mathbf{B}$ matrices which are diagonal, giving a rectangular simulation box:

$$\mathbf{B} = \begin{pmatrix} B_{xx} & 0 \\ 0 & B_{yy} \end{pmatrix} \tag{6.52}$$

then the aspect ratio for the simulation box for phase α will be $B_{xx}^{\alpha}/B_{yy}^{\alpha}$.

The $\mathbf{R}_i$'s are chosen such that $\mathbf{B}^{\alpha}\mathbf{R}_i^{\alpha}$ describes the unscaled lattice for phase α. Finally, the standard NPT definition of L no longer holds, and is replaced by:

$$L^d\,|\mathbf{B}^{\alpha}| = V \tag{6.53}$$

Lattice switch moves are made by switching the value of α as in NVT lattice switch. It can be shown that the acceptance criterion for a lattice switch move in this representation is the same as that given in equation 6.26. Once again, typical configurations in one phase are unlikely to translate well into the other, and we should use multicanonical weighting, this time in the parameter ΔH, as described in equation 6.25.

There is a lot of freedom to choose mappings between lattices in the LSMC technique, and very little experience on how to do this. Whilst any mapping will "work", the best mappings will be those which have as many gateway configurations as possible. It has already been mentioned that mappings should preserve neighbours; if possible, they should also map between characteristic deformations of each phase. One approach to this which shows promise involves describing the particle displacement vectors as superpositions of phonons characteristic to one lattice, found using the harmonic approximation (see chapter 4), and mapping these onto superpositions of phonons characteristic to the other lattice. This has been found to be very effective [101], but becomes less so outside of the region of validity of the harmonic approximation.

It has been suggested that the concept of lattice-switch Monte Carlo can be extended to "phase-switch" Monte Carlo, for interface-free simulation of coexistence between non-lattice phases. This has been used to simulate the melting transition for hard spheres [99, 100].

6.3.3 Error Estimation in Two-Phase Simulation

We have already discussed how to use block averaging to measure the uncertainty in the results from our simulations. This method for measurement of uncertainty in observables is not sufficient to measure uncertainty in the position of coexistence points. To do this, we must consider what we are measuring when we find a coexistence point.

Let us consider a single simulation of two-phase coexistence in the NPT ensemble; generalisation to other ensembles is easy. At coexistence, the extensive Gibbs free energies for the two phases, G_1 and G_2 are equal, that is the difference in Gibbs free energy between phases ΔG is zero. We can rephrase this in terms of the configurational integrals:

$$\begin{aligned} \Delta G &= -\tfrac{1}{\beta}\left(\ln Z_1 - \ln Z_2\right) \\ &= -\tfrac{1}{\beta}\ln\tfrac{Z_1}{Z_2} \end{aligned} \tag{6.54}$$

We do not know the full configurational integrals for the phases, but we can estimate the ratio of these integrals as the ratio of the times the simulation spent in each phase, R, and therefore estimate the free energy difference:

$$\Delta G \approx -\frac{1}{\beta}\ln R \tag{6.55}$$

At our estimated coexistence point, R should equal unity, equivalent to the "equal weights" criteria mentioned at the start of this section. We can estimate the error σ_R in this ratio through block averaging.

To estimate error in our coexistence temperature, we consider ourselves as measuring the free energy difference ΔG (specifically, $\Delta G \approx 0$) at that temperature. From a standard statistical result, we know that the error in temperature will be given by:

$$\sigma_T^2 = \sigma_{\Delta G}^2 \left(\left.\frac{\partial \Delta G}{\partial T}\right|_P \right)^{-2} \tag{6.56}$$

Through standard results and some simple manipulation, this reduces to:

$$\sigma_T^2 = \frac{kT^2}{(\Delta H)^2}\sigma_R^2 \tag{6.57}$$

where ΔH is the difference in average enthalpy between the two phases, and we have used the fact that at coexistence, $R = 1$ and $T\Delta S = -\Delta H$. Estimating error in a different thermodynamic field would involve taking the differential in equation 6.56 with respect to that field.

6.3.4 Gibbs-Duhem Integration

The relatively recent, and extremely elegant, method of Gibbs-Duhem integration [102] allows calculation of a coexistence line using only single-phase, uncoupled simulations, using numerical integration of the Clausius-Clapeyron equation. This equation gives the slope of a coexistence curve in the temperature-pressure plane, and can be written:

$$\left.\frac{dP}{dT}\right|_{coex} = \frac{\Delta H}{T\Delta V} \tag{6.58}$$

Here, ΔH is the difference in enthalpy between the coexisting phases, and ΔV is the difference in volume between the coexisting phases. Both quantities on the right hand side can be sampled through two single-phase simulation runs at a coexistence point. Knowing these, we know the slope of the coexistence point, and should be able to extrapolate to another coexistence point a short interval along the coexistence line.

The method of extrapolation - that is, the method used to numerically integrate the ordinary differential equation 6.58 - is usually of the predictor-corrector ("PC") type. This type of algorithm requires only one evaluation of the integrand at each step, whilst in general other algorithms require many [73]; since evaluation of the integrand requires two full simulation runs, and is therefore generally the most computationally expensive part of the calculation, predictor-corrector algorithms become the method of choice.

In the predictor-corrector formalism, we are to solve an ordinary differential equation of the form:

$$\frac{dx}{dy} = I(x, y(x)) \tag{6.59}$$

To do this, we approximate the true function $y(x)$ by an nth order polynomial around a given point. This polynomial is constructed from n points on the curve (usually equally spaced in x), denoted $(x_i, y(x_i))$ (where i runs between 1 and n), and the values of $I(x_i, y(x_i))$ at those points. Using this polynomial, we extrapolate a new point along the curve, $\left(x_{i+1}^{(0)}, y\left(x_{i+1}^{(0)}\right)\right)$. This *predicted* point is then fed back to produce a better estimate for the polynomial (called an *estimator* step), to give a *corrected* point $\left(x_{i+1}^{(1)}, y\left(x_{i+1}^{(1)}\right)\right)$. This process can then, if desired, be iterated to convergence (as is done in reference [102]), or stopped there [73], before proceeding to the next integration point .

As can be seen, we will need n known points on the coexistence curve to start off a PC algorithm, though it is possible to "kick-start" a high order PC scheme by using lower order schemes to multiply an initially small number of known points. Since increasingly high order PC schemes lose stability at decreasing integration step sizes, it may often be best to avoid this altogether, and use a less accurate but more stable low order scheme.

It can also be seen that progressively greater error is introduced into the estimates with every integration step. We start off with only the errors in the original known points; with every step, we introduce stochastic error in the estimation of I from the simulations, and systematic error by approximating the coexistence curve to a polynomial. As such, where possible points regularly spaced along a Gibbs-Duhem integration should be checked using some other means.

Chapter 7

Simulation Results

In this chapter, we will present results gleaned from the methods we discussed in the previous chapter, applied to systems of particles interacting via equation 2.15. We will start by extending our solid state approximation results from chapter 4 using Lattice Switch Monte Carlo and Gibbs-Duhem integration in the NPT ensemble; we describe our implementation of these methods, and the results which we gain from them. Then, using grand canonical simulation, we will turn to the liquid state, as studied by Sadr-Lahijany et al [1]; after presenting our results, we will note the unusual finite size of the system. Finally, we will use grand canonical simulation to investigate the three dimensional version of our chosen system. Discussion of the meaning and implications of our results will be saved for the next chapter.

7.1 Two Dimensions

7.1.1 Solid State Simulation

Simulation Procedure

Our simulations of coexistence in the solid phase use two different algorithms, Lattice Switch Monte Carlo and Gibbs-Duhem integration. At the core of these two different methods lies a common implementation of the basic NPT Monte Carlo algorithm.

We implement this common base to the methods in the C programming language. We use relatively small system sizes with $N = 256$ particles, implementing a potential cutoff at

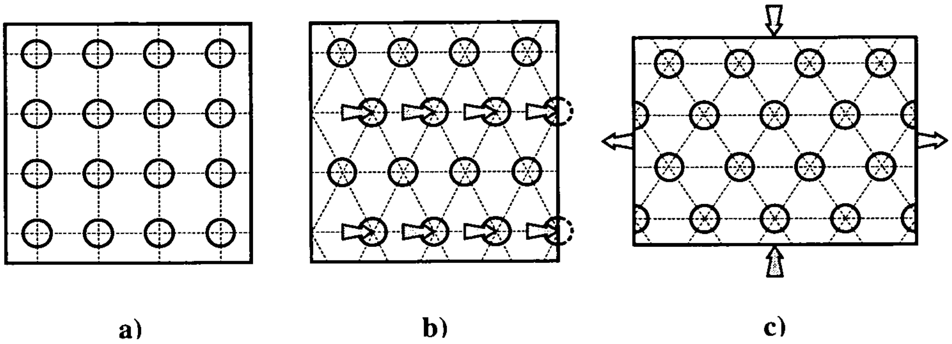

Figure 7.1: a) Particles on lattice given by $\mathbf{R}_i^{square}$, with $\mathbf{B}^{square}$ (the identity matrix) applied. This is a square lattice.
b) Particles on lattice given by $\mathbf{R}_i^{tri}$; arrows show displacement with respect to $\mathbf{R}_i^{square}$ positions.
c) Particles on lattice given by $\mathbf{R}_i^{tri}$, with matrix $\mathbf{B}^{tri}$ applied; this gives a triangular lattice. Circles mark lattice sites; dashed lines mark lattice vectors.

$r_c^* = 2.5$. Simulations of the square lattice phase are implemented using a square simulation box; simulations of the triangular lattice are implemented using a box with aspect ratio $\frac{\sqrt{3}}{2}$, allowing the lattice to be commensurate with the simulation box. Simulation code outputs total system configurational energy and system volume. It can also output structural data in the form of the radial distribution function $g(r)$ and snapshot configurations - whilst such snapshots are not as rigorous a measure of structure as the function $g(r)$, they are often valuable in visualising systems.

Our implementation of the Lattice Switch scheme follows from the generalised scheme given in chapter 6. Our set of lattice vectors $\mathbf{R}_i^{square}$ are given by a square lattice oriented with the box, as seen in figure 7.1 a. The $\mathbf{B}^{square}$ matrix is given by the identity matrix:

$$\mathbf{B}^{square} = \begin{pmatrix} 1 & 0 \\ 0 & 1 \end{pmatrix} \tag{7.1}$$

The lattice vector set $\mathbf{R}_i^{tri}$ is as the square lattice set, but with every other lattice plane shifted a half lattice spacing horizontally (see figure 7.1 b). To this, we apply the $\mathbf{B}^{tri}$ matrix, given by:

$$\mathbf{B}^{tri} = \frac{\langle V^{tri} \rangle}{\langle V^{sq} \rangle} \begin{pmatrix} \sqrt{2/\sqrt{3}} & 0 \\ 0 & \sqrt{\sqrt{3}/2} \end{pmatrix} \tag{7.2}$$

This takes us to a triangular lattice, as seen in figure 7.1 c. The scaling constant $\frac{\langle V^{tri} \rangle}{\langle V^{sq} \rangle}$ is evaluated before the Lattice Switch runs at a given state point by two quick single-phase NPT simulations.

Attempts to make lattice switch moves are made as often as volume change moves, with the acceptance probability given by

$$p_{nm} = \min\left(1, e^{-\beta \Delta H_{nm}}\right) \tag{7.3}$$

The "overlap parameter" ΔH_{nm} is calculated as per normal (see chapter 6).

In addition to configurational energy and system volume, our LSMC simulations also output values for ΔH and for which lattice the system is in. As is standard in LSMC simulations, we use multicanonical sampling in ΔH to facilitate lattice switch moves [96, 97, 98]. The data output from the simulation is used to build ΔH histograms for each phase according to the "visited states" scheme, which are then fed back into the simulation as multicanonical weights; this process is iterated to convergence with acceptably small statistical error, calculated as outlined in section 6.3.3 . Histogram reweighting is then used to find the pressure at which the two histogram weights are equal and the phases are in coexistence.

Our Gibbs-Duhem scheme is as outlined in chapter 6. To recap, we are solving a simple ordinary differential equation given by the Clausius-Clapeyron equation:

$$\left.\frac{dT}{dP}\right|_{coex} = kT\frac{\Delta v}{\Delta h} \tag{7.4}$$

with the subscript indicating coexistence, Δv as the difference in average volume per particle between the phases at coexistence, and Δh as the difference in average enthalpy per particle between the phases at coexistence. We denote the right hand side of this equation $I(P,T)$. In our implementation, we solve this equation using a simple trapezoid predictor-corrector algorithm. We perform runs in each phase at a coexistence state point, then evaluate $I(P,T)$ at that point. We use this "predictor" step to estimate a new coexistence point as being at:

$$\begin{aligned} P_p &= P + \Delta P \\ T_p &= T + \Delta P I(P,T) \end{aligned} \tag{7.5}$$

where ΔP is a chosen pressure step size. We then perform runs for each phase at this estimated coexistence point, and evaluate $I\left(P_p, T_p\right)$. This "corrector" step is used to correct the estimate of coexistence; the corrected coexistence state point is given by:

$$\begin{aligned} P_c &= P_P \\ T_c &= T + \tfrac{\Delta P}{2}\left(I(P,T) + I\left(P_p, T_p\right)\right) \end{aligned} \tag{7.6}$$

The process is then be continued, treating the corrected coexistence point as a new actual coexistence point. Step size ΔP should be small enough that features of the curve are properly resolved, whilst large enough to move along the coexistence curve at a reasonable speed.

The formulae for error estimation with this method can be found in reference [103].

Simulation Results

We have used our LSMC implementation to study the transition lines found with the harmonic approximation in chapter 4. We "kick-start" our LSMC simulations by giving them initial configurations of particles lying at points on the appropriate lattices, at the volumes predicted by the harmonic approximation.

The HDSS – HDTS transition occurs at pressures well above those at which the behaviours we are interested in occur; as such, we have performed only two LSMC simulations (at $T^* = 0.1$ and $T^* = 0.2$) to verify its existence. Here, our simulation results agree with the harmonic approximation (see figure 4.4).

We have attempted to use LSMC to study metastable LDTS–HDTS coexistence. Whilst our simulations at low temperature ($T^* = 0.05$ and $T^* = 0.1$) do show triangular lattice phases of the predicted densities, these have a very short lifespan in our simulation runs before transforming into the HDSS phase. This lifespan is not sufficient to allow simulation of coexistence using LSMC simulation; it is also too short to allow good statistics for the Gibbs-Duhem method.

This leaves us with the LDTS – HDSS transition. We have successfully used LSMC to find coexistence points up to $T^* = 0.4$. These are shown in figure 7.2. We can see that they agree well with the harmonic approximation up to a temperature of $T^* = 0.2$; above this temperature, the simulated coexistence points lie at significantly higher pressures than those from the harmonic approximation. This is to be expected; at the very low density of the LDTS phase, the local energy landscape surrounding the lattice positions is unlikely to be well characterised as parabolic on the scale of typical particle deviations from their lattice positions.

Above $T^* = 0.2$, the LSMC method was found to become increasingly less efficient. At

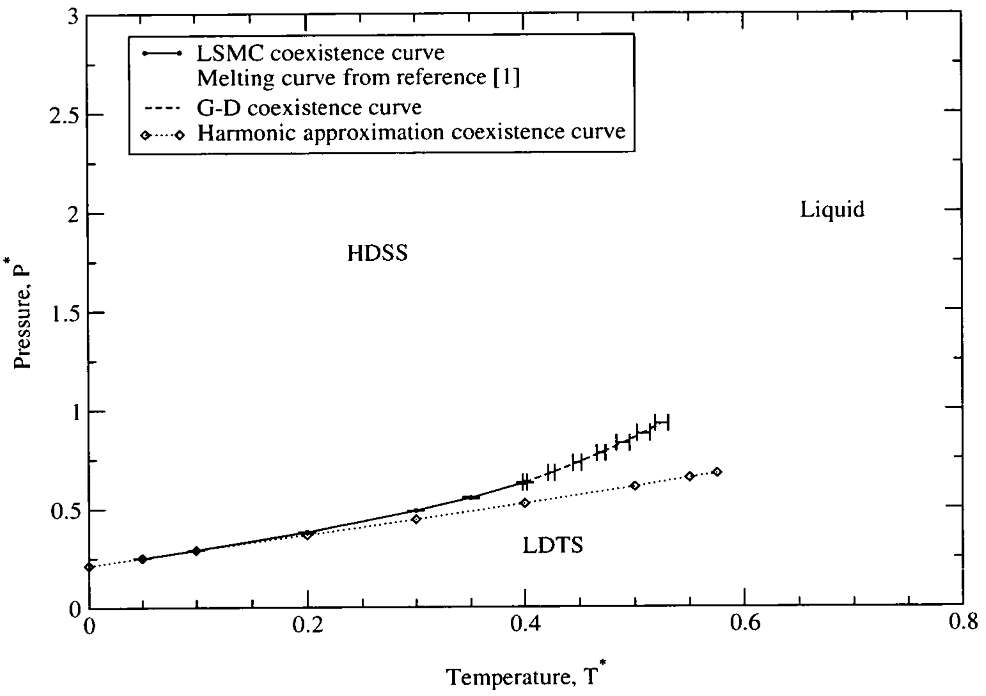

Figure 7.2: Phase diagram showing the HDSS-LDTS transition line calculated within the harmonic approximation (dotted line, see chapter 4), from LSMC simulations (full line), and from Gibbs-Duhem integration (dashed line). Simulation data is from NPT simulations with N = 256. Error bars for LSMC results are calculated as outlined in section 6.3.3; error bars for Gibbs-Duhem results are calculated according to the prescription given in reference [103]. Also shown is the melting curve taken from reference [1] (thick grey line).

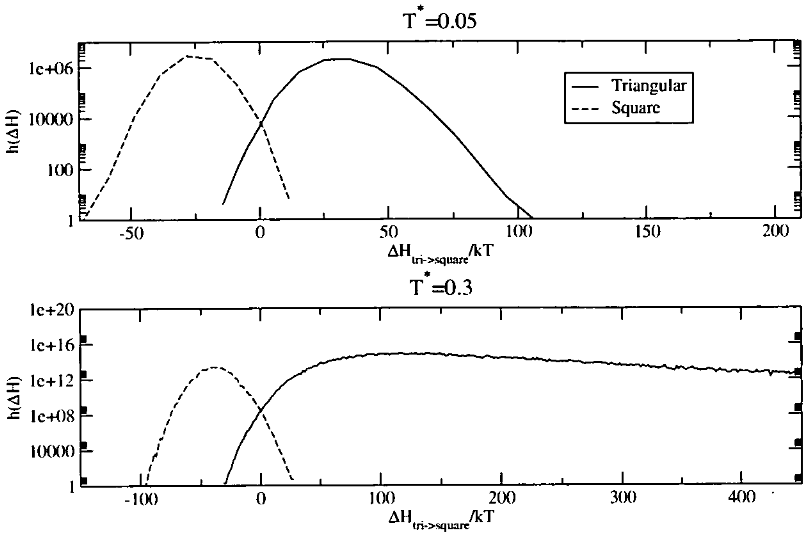

T*=0.05

T*=0.3

Figure 7.3: $\Delta H_{tri \rightarrow square}$ histograms for LDTS – HDSS LSMC simulations at $T^* = 0.05$ and $T^* = 0.3$, system size N = 256. At $T^* = 0.05$, the histograms have Gaussian character, and are approximately symmetric. At $T^* = 0.3$, the ΔH histogram for the HDSS-LDTS move has this "normal" character, whilst the LDTS-HDSS histogram has a pronounced asymmetry, with a significant high-ΔH tail.

low temperatures, the collected ΔH histograms are as would normally be expected - that is, approximately Gaussian for both phases. With increasing temperature, however, the ΔH histograms for the LDTS phase change to a distribution more log-normal in character, that is, asymmetric with a pronounced high-ΔH tail. This is shown in figure 7.3. We believe that this behaviour reflects an increase in the defect density on approach to melting. This long tail makes good sampling of ΔH much slower; beyond $T^* = 0.4$, this becomes so severe that use of LSMC is no longer feasible.

The remainder of the coexistence line has been evaluated using Gibbs-Duhem integration. The results are shown in figure 7.2, and can be seen to smoothly extend the transition line up to $T^* = 0.525 \pm 0.006, P^* = 0.929$, above which the LDTS phase was observed to melt in simulation. Whilst this is a poor estimate to the LDTS melting curve, due to the possibility of hysteresis, it is within error in temperature of the melting curve reported by Sadr-Lahijany et al [1], though at a significantly lower pressure than their estimate for the LDTS – HDTS-liquid triple point.

7.1.2 Liquid State Simulation

Simulation Procedure

Our Monte Carlo simulations of the liquid state have been performed in the grand canonical (constant μVT) ensemble. We have performed a large number of small systems size simulations, with square simulation boxes of size $L^* = 10$, using a potential cutoff at $r_c^* = 2.5$. The simulation code outputs total system configurational energy and particle number. Isothermal compressibility is calculated from fluctuations in particle number according to the standard prescription for this ensemble from reference [71], that is:

$$K_T = \frac{\beta V \left\langle \partial N^2 \right\rangle_{\mu VT}}{\langle N \rangle_{\mu VT}} \tag{7.7}$$

To find extrema in compressibility and density, we first perform a set of Monte Carlo runs at points along a line of constant chemical potential. The simulation data were then combined self consistently according to the multihistogram framework. Actual positions of extrema are estimated by using a golden section search [73] along the line of constant chemical potential, evaluating the appropriate observable by using histogram reweighting on our combined data set.

Where we have observed two-phase coexistence (either directly or by observing hysteresis along a line of constant chemical potential in our simulation results), where necessary we have used multicanonical sampling in number density to estimate the position of the coexistence line to within acceptable statistical error, as estimated in section 6.3.3. This has been done using the standard visited states iterative approach - in summary, we feed an observed bimodal number density histogram back into the simulation as a set of multicanonical weights, until the histogram coming out of the simulation converges with the histogram used as a weight function with acceptably small statistical error. The point of coexistence is then estimated by using histogram reweighting to find the state point at which the weight under each peak in the number density histogram is equal.

During the course of a simulation run, we also collect structural data in the form of the radial distribution function $g(r)$ [71]. Our simulation code can also output "snapshot" particle configurations from the system.

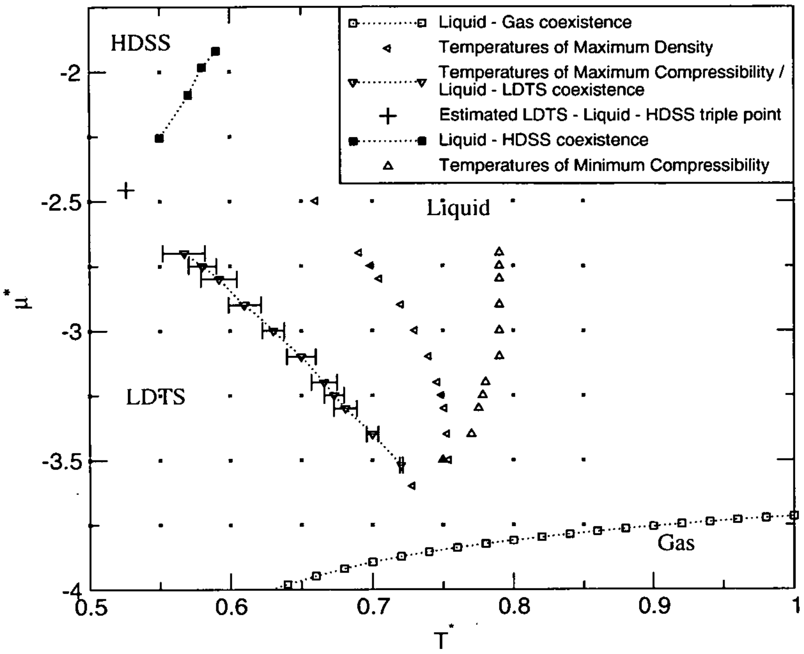

Figure 7.4: Phase diagram from μVT simulations, $V^* = 100$, showing the positions of liquid state anomalies and coexistence curves, as denoted in the legend. The + denotes the estimated LDTS - liquid- HDSS triple point. Simulations were performed at points marked with × symbols.
Note that the liquid state anomalies and LDTS-liquid coexistence line suffer from strong finite size effects (see text), and the "true" large system size anomaly lines will be at significantly lower temperature. HDSS-liquid coexistence is only estimated, due to difficulty in simulating this transition (see text).

Simulation Results

A $\mu - T$ phase diagram showing the results from our simulations of the liquid phase is shown in figure 7.4; also shown is the liquid-gas coexistence curve calculated by Wilding [3]. We confirm the presence of liquid state anomalies in the system; we observe both a TMD line and a locus of points of extremal compressibility. We demonstrate these anomalies with a typical plot of the temperature behaviour of compressibility and density at $\mu^* = -3.0$ in figure 7.5.

The lines of minimum compressibility and of maximum density appear as anticipated. However, near the line of maximum compressibility, the number density histograms from simulations are bimodal - that is, they have two peaks, indicating two-phase coexistence. An example is shown in figure 7.6 a. Further, if we examine the time evolution of number density from simulations at these points (figure 7.6 b), we find that the simulation passes back and forth between these phases with relative ease, even without multicanonical weighting. If we use histogram

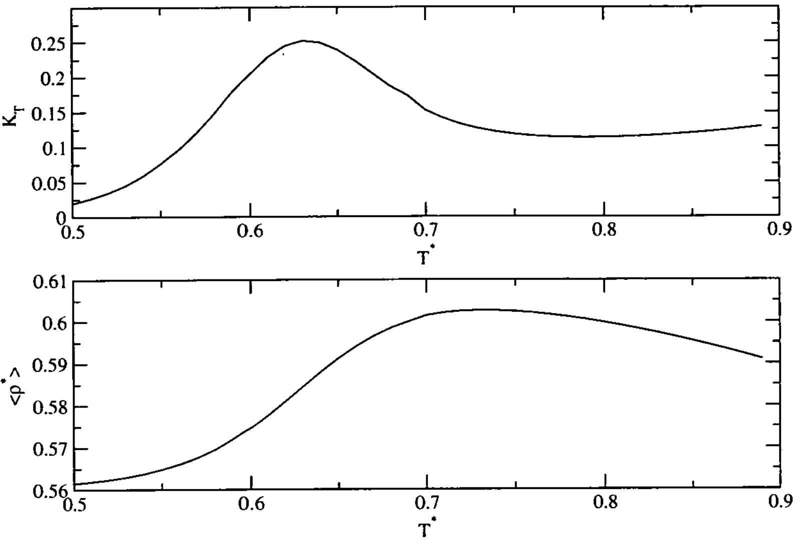

Figure 7.5: Compressibility and density against temperature for $\mu^* = -3.0$, showing the presence of compressibility extrema and a density maximum.

reweighting techniques to find the exact coexistence line, that is, where these points have equal weight, we find that it traces out the line of maximum compressibility.

We attempt to illuminate this by considering the results collected from simulations on either side of this line. Figure 7.7 a shows the number density distribution, figure 7.7 b snapshot configuration, and figure 7.7 c the $g(r)$ histograms from simulations performed at $T^* = 0.6$. In the left hand column of figure 7.7, we see the results from a simulation performed below the coexistence line, at $\mu^* = -3.5$. Here, we have a very narrow number density histogram ($\langle\rho^*\rangle = 0.56$)and a $g(r)$ function characteristic of a solid phase. This is borne out by the snapshot configuration, which shows particles occupying a triangular lattice. These data are consistent with our simulation results for the LDTS phase. The central column of figure 7.7 shows the results from a simulation performed at $\mu^* = -2.5$. This shows a wide, Gaussian-like number density histogram ($\langle\rho^*\rangle = 0.63$ - we note that the liquid is more dense than the LDTS solid phase), and a $g(r)$ function tending to 1 with increasing r. The snapshot configuration is without order. This is what we expect from a liquid phase. Our data are consistent with the line of maximum compressibility tracing out the LDTS-liquid coexistence curve. This transition line has negative slope in the P – T plane, as the LDTS phase has greater volume than the liquid phase.

It should be noted that simulations in the LDTS phase have low (order 1%) acceptance rates

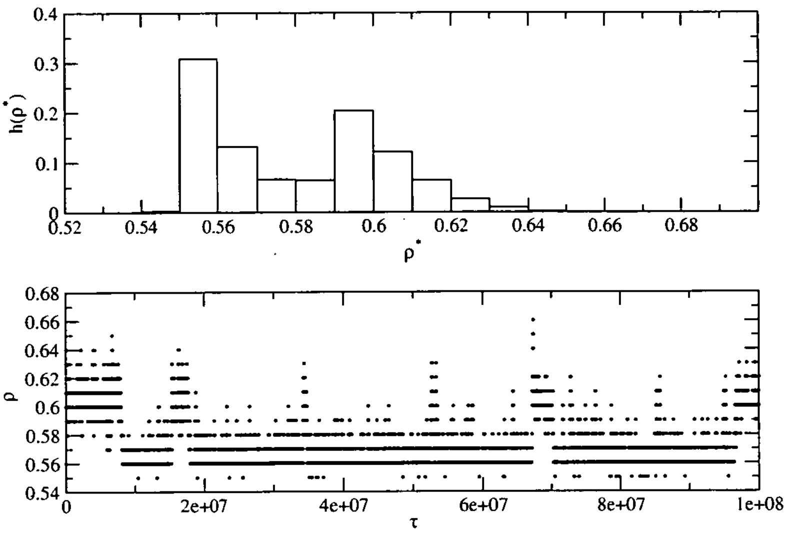

Figure 7.6: a) Particle number histogram collected from a μVT simulation at $V^* = 100, T^* = 0.6, \mu^* = -3.0$, close to a point of compressibility maximum. This distribution is clearly bimodal.
b) Raw simulation data (system density ρ^* against Monte Carlo move number τ) collected without using multicanonical reweighting at $V^* = 100, T^* = 0.6, \mu^* = -3.0$. The simulation can clearly be seen to regularly pass back and forth between phases (though not often enough to give good statistical information).

for particle insertion and deletion moves. Though acceptance rates this low are very unusual for at the densities observed for this phase, they are consistent with our interpretation of the LDTS phase as a solid phase.

Above $\mu^* \gtrsim -2.5$, upon cooling, freezing into the LDTS phase is preempted by a transition to a high-density phase. We once again attribute this phase by considering number density distribution, $g(r)$ and a snapshot configuration, as shown in the right hand column of figure 7.7. We note a narrow, high density number density histogram ($\langle \rho \rangle = 0.82$), a solid phase $g(r)$, and a snapshot configuration with particles occupying a square lattice. This is consistent with our simulation results for the HDSS phase. Evaluating the melting curve here has proven more difficult than with the LDTS phase, even using multicanonical sampling. First, transition back and forth between liquid and HDSS is not observed over the lifetime of an unweighted simulation. Secondly, the free energy barrier between the HDSS and the liquid phase is both deep and, in terms of density as an order parameter, wide. Finally, as has previously been remarked, the grand canonical Monte Carlo algorithm is unsuited to working in high-density phases, especially lattice solids. Whilst four HDSS-liquid coexistence points are marked in figure

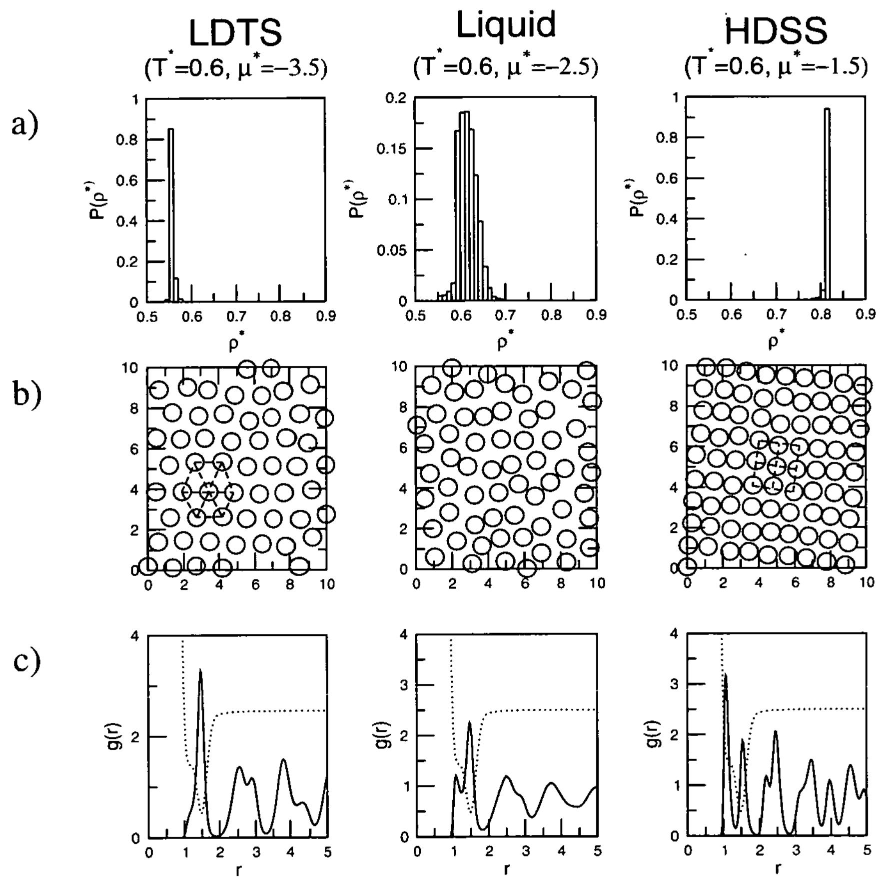

Figure 7.7: a) Density distributions for (left) the LDTS phase at $T^* = 0.6, \mu^* = -3.5$, for the liquid phase (centre) at $T^* = 0.6, \mu^* = -2.5$ and for the HDSS phase (right) at $T^* = 0.6, \mu^* = -2.5$.

b) Snapshot configurations for the LDTS phase (left), the liquid phase (centre) and the HDSS phase (right). Dashed lines join nearest neighbour particles in the lattice phases.

c) The full line shows the radial distribution function $g(r)$ for the HDSS phase (left), the liquid phase (centre) and the LDTS phase (right). The interparticle potential is shown schematically as a dotted line for comparison.

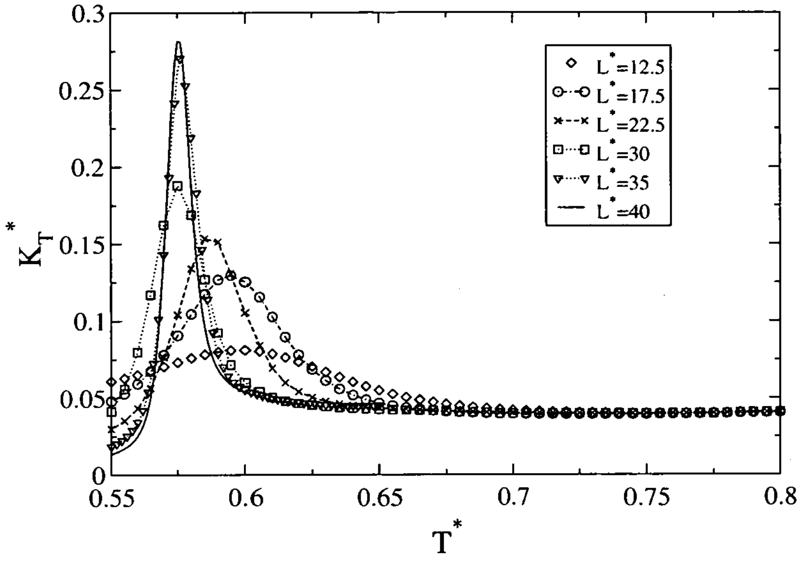

Figure 7.8: Temperature dependence of isothermal compressibility at $\mu^* = -3.0$ for various system sizes.

7.4, acceptance rates for particle insertion and deletion were of order < 0.01%, the statistical error (not shown) is large, and this coexistence line should be taken as a guide only. It may well be possible to gain more precise results using phase-switch Monte Carlo in the NPT ensemble [99, 100].

Due to the difficulty in estimating the HDSS melting curve, it is difficult to find the position of the HDSS-LDTS-liquid triple point to any precision. By fitting data from both melting curves using linear regression (a rather naive technique), we estimate the triple point at $T^* \approx 0.526, \mu^* \approx -2.5$ (as shown in figure 7.4). In the same way, we estimate this triple point pressure as $P^* \approx 0.9$. This is close to our estimate of the triple point from our solid-state simulations. It is within error in temperature (though significantly lower in pressure) to the estimate by Sadr-Lahijany, et al. These three triple point estimates are all vulnerable to hysteresis, of course, and are all performed in different ensembles at different system sizes.

Finite Size Effects

As part of this work, the finite size effects in the liquid state have been studied by Wilding [3]. In particular, the finite size effects for the liquid state anomalies (and hence the liquid-LDTS transition) have been assessed; it has not proven possible to study these effects for the liquid-HDSS transition (see remarks above).

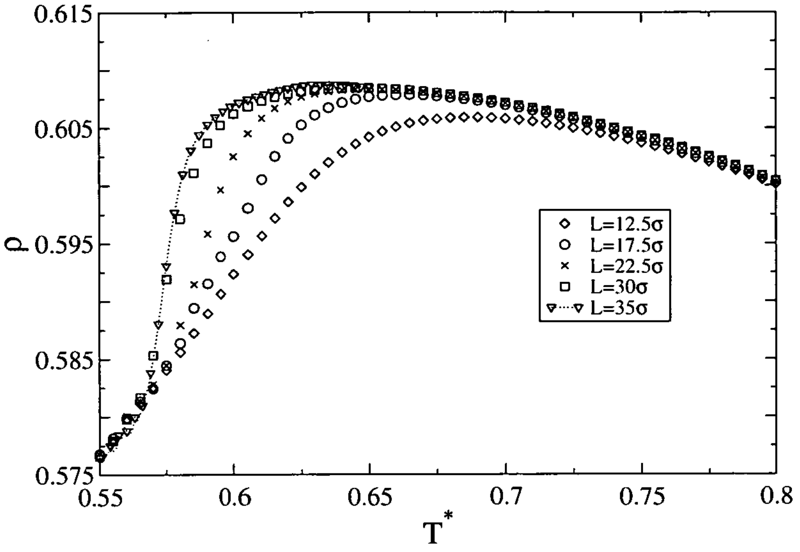

Figure 7.9: Temperature dependence of number density at $\mu^* = -3.0$ for various system sizes.

The behaviour of compressibility and density along a typical line of constant chemical potential ($\mu^* = -3.0$) with system size is shown in figures 7.8 and 7.9. We first consider the behaviour of the compressibility. We can see in figure 7.8 that, with increasing system size, the maximum in compressibility moves to lower temperature, and becomes both higher and sharper. At all system sizes, this peak coincides with liquid-LDTS coexistence. Wilding's results for the liquid-LDTS coexistence line (at system size $L^* = 40$) are shown compared to our results ($L^* = 10$) in figure 7.10.

We now move on to the system size behaviour of the density. Wilding's results are shown in figure 7.9. We again see the temperature of maximum density move to lower temperature with increasing size, though we note that by $L^* = 35$ the density curves appear to reach convergence. This final estimate for the TMD curve is at a higher temperature than the compressibility maxima at the largest system size studied; Wilding has observed that, upon cooling below the TMD curve, the number density histograms for the large system simulations gain a "subsidiary peak" at the LDTS density [3]. We interpret this as infrequent fluctuations into the LDTS phase *before* coexistence is reached. We will discuss this matter further in chapter 8.

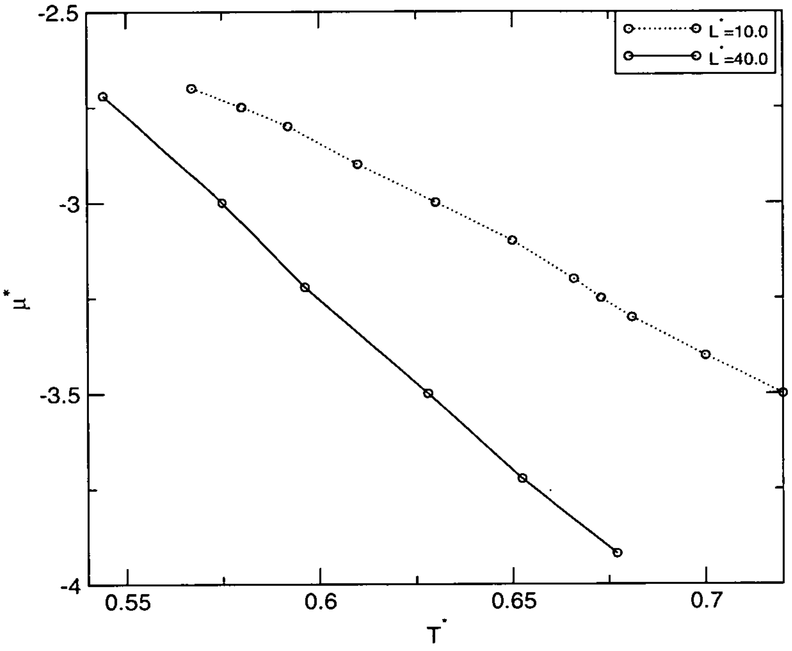

Figure 7.10: LDTS-liquid melting curves for system size $L^* = 10$ (dotted line) and $L^* = 40$ (full line). Symbols show coexistence points found using histogram extrapolation; lines are guides to the eye.

7.2 Three Dimensions

7.2.1 Simulation Procedure

Our simulations of the liquid state of the system in three dimensions are once again performed in the grand canonical ensemble. We use a standard μVT algorithm at a system size of $L^* = 10$, with a potential cutoff at $r_c^* = 2.5$, with a cell approximation (cells have length r_c). Simulation of liquid-gas coexistence has been performed using multicanonical sampling in number density with the visited states algorithm. Simulations output total system configurational energy and number density, as well as structural data in the form of $g(r)$ and snapshot configurations.

7.2.2 Simulation Results

We have used grand canonical Monte Carlo simulations to study the liquid state of the three dimensional system. In three dimensions, the grand canonical algorithm only functions with any efficiency up to a number density $\rho^* \approx 0.65$ [71]. We have performed simulations in a range with the liquid-gas coexistence curve as a low chemical potential limit, the liquid-gas critical

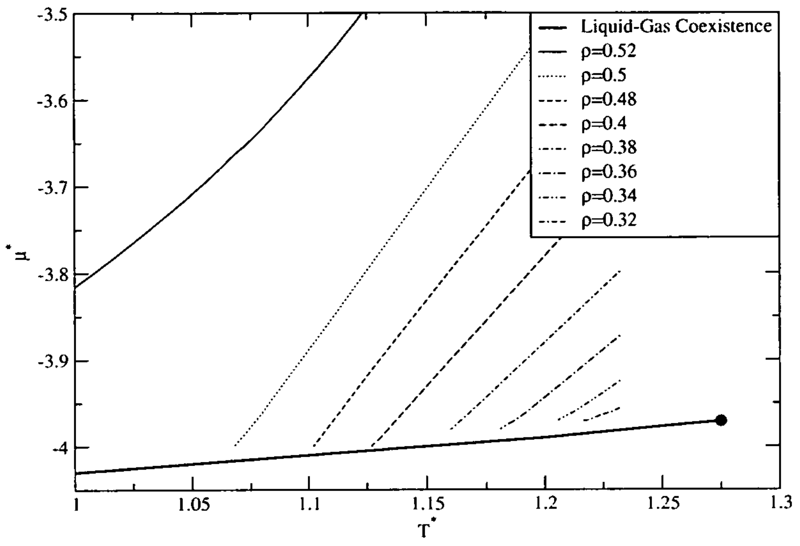

Figure 7.11: Phase diagram for the three-dimensional system, showing liquid-gas coexistence (thick line), the estimated liquid-gas critical point (filled circle), and a number of lines of constant density (as key).

point temperature as a high temperature limit, and $\rho^* \approx 0.6$ as a low temperature and high chemical potential limit.

We have found it helpful to locate the liquid-gas coexistence line and critical point for this system, so that the effects of approach to the critical point or transition line are not mistaken for liquid-state anomalies. Since the liquid-gas critical behaviour of this system is not of direct interest to us, we have not attempted to place the critical point to any great accuracy.

Our results show neither density nor compressibility anomalies across the range we have studied ($T^* \approx 0.95 \ldots 1.3, \mu^* \approx -4 \ldots -3.5$). In the interests of completeness, we show the liquid-gas coexistence line and several lines of constant density in figure 7.11.

Chapter 8

Discussion and Conclusions

We start this chapter by discussing our results, and drawing conclusions concerning the nature of the liquid state anomalies we have observed for our system. We will then discuss various aspects of some of the methods we have used in the course of this work. Finally, we offer our thoughts on the behaviour of core-softened potentials in general.

8.1 Discussion - Results

We have studied the phase behaviour of two dimensional systems interacting via a particular instance of core-softened potential (equation 2.15). We have studied both liquid and solid state behaviour. Solid state results start from harmonic approximation calculations; these suggest that at low pressures, there is a transition from a low density triangular lattice to a high density square lattice phase. At very high pressures, the triangular lattice becomes stable once more, this time at a high density. Metastable with respect to the square lattice, we find evidence for an isostructural LDTS-HDTS transition with possible associated critical point.

This picture has been confirmed using Monte Carlo simulations, with the coexistence line between LDTS and HDSS phases mapped using a combination of Lattice Switch Monte Carlo and Gibbs-Duhem integration. We note that, on approach to the LDTS-HDSS-liquid triple point, particles in the LDTS phase make large excursions from their lattice sites.

We have also performed extensive simulations of the liquid phase for this system. These confirm the presence of liquid state anomalies in this system - that is, density maxima and compressibility extrema along lines of constant chemical potential. The positions of the compressibility maxima in the phase diagram appear to be associated with freezing to the LDTS phase. Density probability distribution functions at the compressibility maxima have a double-peaked structure, showing phase coexistence. Recorded particle configurations and radial distribution data recorded on either side of the line of maxima indicate that the coexisting phases have LDTS structure (on the low temperature side) and liquid structure (on the high temperature side). Simulations by Wilding [3] have also revealed pronounced finite-size effects on the position of the anomalies (and therefore the position of the LDTS melting curve).

We believe that the anomalies are due to structural competition between the liquid structure and clusters of lower density, lower entropy LDTS crystalline structure, rather than between two types of liquid structure, as suggested by Sadr-Lahijany et al [1]. The presence of these LDTS-like clusters lowers the average density of the system, and increases the compressibility; their size and persistence increase upon cooling towards the freezing transition, giving the anomalous behaviour. These solid clusters may appear above the melting curve because of the nature of melting in two dimensions. Our results point to a quasi-continuous freezing transition; at the system sizes we have studied, the free energy barrier between phases is very small, allowing such clusters to forms far above melting.

This interpretation is consistent with our simulation results for the equivalent three dimensional system, in which we find no anomalous liquid state behaviour; in three dimensions, freezing must be strongly first order, and we will see no precursor effects.

In summary, then, our results for the Sadr-Lahijany system point to an LDTS-liquid melting transition that is defect moderated and only weakly first order. Compressibility anomalies in the system are due to the fluctuations associated with this transition, and density anomalies are due to fact that the LDTS phase is less dense than the liquid. With respect to the possibility of liquid-liquid phase separation for this system, if this melting transition were truly continuous, the concept of a liquid phase metastable with respect to the LDTS phase would become difficult to support. In this case, the possible metastable LDTS-HDTS transition and critical point would be equivalent to the metastable liquid-liquid transition proposed by Sadr-Lahijany et al [1], but too far removed from the observed anomalies to be realistically effecting the behaviour. With the melting transition as weakly first order, our results do not discount the possibility of a metastable liquid-liquid transition. However, it is difficult to see how it could produce such strong anomalies over so wide a region of phase space.

Continuous melting is an interesting behaviour which remains a matter of research and debate; as such, any system which may exhibit such behaviour is deserving of further study. However, unequivocal confirmation of hexatic phase behaviour requires very large system size simulations, calculating computationally expensive orientational distribution functions, and is outside the scope of this work.

8.2 Discussion - Methods

We have used a variety of methods over the course of this work; two seem particularly deserving of comment. The first is Lennard-Jones Devonshire cell theory, for a long time the main method for approximating liquid state behaviour. Our results call for a major reappraisal of this method. The second is Lattice Switch Monte Carlo, a very recently proposed method for simulating coexistence between lattice phases, and by extension, for simulating coexisting phases of different symmetries separated by large free energy barriers. We appraise how useful this novel method has been in this context.

8.2.1 Lennard-Jones Devonshire Cell Theory

The major success of Lennard-Jones Devonshire cell theory has been regarded as its apparently accurate prediction (to one part in a hundred) for the critical temperature of the 12-6 Lennard-Jones fluid. We have shown that this critical point in the cell model actually terminates a line of coexistence between solid-like and liquid-like phase. This critical point is an artifact of the cell structure of the model, which imposes crystalline order on the liquid state, where no such order exists in reality. Further, we have found that the cell theory model shows a second line of first order transition, which we believe to be a better candidate for the liquid-gas transition. This line terminates in a critical point at a temperature very much lower than the true critical temperature, as one would expect from a mean-field theory.

In our cell theory study of the Sadr-Lahijany system, we use two different cell theory implementations. One gives a system with a gas-liquid transition and critical point and a solid-liquid transition with artifact critical point; the second gives a system with two solid-liquid transitions with artifact critical points. Neither implementation gives a phase diagram showing more than a passing qualitative resemblance to our simulation results, and neither exhibit any evidence of a liquid-liquid transition.

Based upon our findings, we believe cell theory to be a poor approximation to both liquid and lattice states.

8.2.2 Lattice Switch Monte Carlo

Our use of the LSMC technique here has demonstrated both its generality and its limitations. We have successfully generalised the technique to two dimensions, where we have used it to study LDTS-HDSS coexistence in the NPT ensemble. The technique has worked reliably and efficiently at low temperature. At higher temperatures, problems emerged due to the increasing defect density of the LDTS phase on approach to melting. For LSMC to work, average particle positions must be identifiable with a true lattice structure; however, on approach to melting in two dimensions, the lattice can become extremely distorted due to propagation of dislocation defects. Even developments such as harmonic LSMC cannot help if this occurs, as the assumption of a true lattice is broken. It is possible that "phase switch" LSMC could be adapted to study this system.

Similarly, the extension of the ideas in LSMC to "phase switch" Monte Carlo would not be useful for finding the LDTS-liquid coexistence curve, since a true lattice would still be assumed for the LDTS phase at melting. Phase switch Monte Carlo could well be used to establish the HDSS-liquid coexistence curve, however; our results suggest that this transition is strongly first order.

None of this is a weakness with LSMC *per se*, of course; LSMC was designed with three dimensional lattice systems in mind, which always retain long range translational order, and always melt through first order transitions. That the algorithm remained usable to as high a temperature as it did should be seen as a success. It would be interesting to see if the ideas of LSMC can be usefully extended to structures with order intermediate between lattices and fluids.

8.3 Discussion - Core-Softened Potentials

Some work concerning core-softened potentials [1, 51] has studied two dimensional systems, apparently without regard for the possibility of continuous melting. Where these works have searched for evidence of second critical points, the lack of consideration of the possibility of another form of second-order transition in the system is problematic. If the possibility of continuous melting is taken into account, however, in light of our results, core-softened potentials in two dimensions become worthy of study as a possible test bed for theories on hexatic melting.

There is still a good deal of research to be done on the phase behaviour of these potentials, with the goal of finding what features of these potentials are responsible for the presence, stability and position of possible liquid-liquid phase transitions and liquid state anomalies. We feel that such research should not concentrate solely upon the liquid state; the presence, stability and position of possible solid-solid isostructural transitions may well be linked to the possibility of liquid-liquid phase transitions [54, 55]. Core-softened potentials can also offer rich and interesting solid state phase behaviour [51, 57, 58, 59]; a good motivation for further research into this could be the discovery of very large unit cell structures in Cesium.

Appendix A

Statistical Mechanics

This appendix contains brief summaries, without proofs, of three matters from the text: use of statistical mechanics in continuum systems, statistical mechanics in open ensembles, and the Clausius-Clapeyron equation for the slope of coexistence curves.

Continuum Systems

We consider a continuum system of N particles in d dimensions, in the canonical ensemble. This system has a $2N^d$ dimensional phase space; N^d dimensions describing the possible particle positions, and N^d dimensions describing particle momenta. As such the partition function becomes:

$$Z = \frac{1}{N!}\frac{1}{h^{dN}}\int e^{-\beta E(\mathbf{r},\mathbf{p})}d\mathbf{r}d\mathbf{p} \tag{A.1}$$

Here, we have separated the general phase space coordinate $\mathbf{\Gamma}$ into $\mathbf{r}$, describing all particle positions, and $\mathbf{p}$, describing all particle momenta. The prefactor is a necessary quantum mechanical contribution; the $1/N!$ accounts for particle indistinguishability, whilst the term involving Planck's constant h accounts for the zero of entropy for the ideal gas.

We can separate the energy into a sum of kinetic (momenta dependent) and potential (position dependent) terms; this allows us to factorise the partition function into kinetic and potential parts:

$$Z = \frac{1}{N!}\frac{1}{h^{dN}}\int e^{-\beta E(\mathbf{p})}d\mathbf{p}\int e^{-\beta E(\mathbf{r})}d\mathbf{r} \tag{A.2}$$

The first, kinetic part of this is easily evaluable; it is the partition function for the ideal gas, denoted Z^{id}, and given by:

$$Z^{id} = \frac{V^N}{N!\Lambda^{dN}} \tag{A.3}$$

where Λ is the thermal de Broglie wavelength, given by $\Lambda = (h^2/2\pi mkT)^{1/2}$ in three dimensions. The remaining potential term of the partition function is known as the *excess* part, Z^{ex}:

$$Z^{ex} = V^{-N}\int e^{-\beta E(\mathbf{r})}d\mathbf{r} \tag{A.4}$$

In analytic and Monte Carlo studies, we often use just the *configurational integral* part of this:

$$Z^{config} = \int e^{-\beta E(\mathbf{r})}d\mathbf{r} \tag{A.5}$$

The full partition function is then given by:

$$Z = Z^{id}V^{-N}Z^{config} \tag{A.6}$$

As all thermodynamic properties are derived from the log of the partition function, they can all be expressed as sums of configurational and ideal (other) terms from equation A.6; it is common in analytic and Monte Carlo studies to disregard the trivial ideal terms, unless connection must be made to experiment.

Open Ensembles

With fixed NPT (the isothermal-isobaric ensemble), the probability distribution function becomes:

$$p_{NPT}(\mathbf{\Gamma}, V) = \frac{1}{Z_{NPT}}e^{-\beta(E(\mathbf{\Gamma})+PV)} \tag{A.7}$$

with P as the pressure. The partition function for this ensemble is given by:

$$Z_{NPT} = \sum_{V} \sum_{\mathbf{\Gamma}} e^{-\beta E(\mathbf{\Gamma})} e^{-\beta PV} \tag{A.8}$$

The appropriate free energy is the Gibbs free energy; this is given by:

$$\begin{aligned} G &= -\tfrac{1}{\beta} \ln Z_{NPT} \\ &= E - TS + PV \end{aligned} \tag{A.9}$$

In the grand canonical ensemble (fixed μVT), the probability distribution function is given by:

$$p_{\mu VT}(\mathbf{\Gamma}, N) = \frac{1}{Z_{\mu VT}} e^{-\beta(E(\mathbf{\Gamma}) - \mu N)} \tag{A.10}$$

with μ as the chemical potential. The partition function for this ensemble is given by:

$$Z_{\mu VT} = \sum_{N} \sum_{\mathbf{\Gamma}} e^{-\beta E(\mathbf{\Gamma})} e^{\beta \mu N} \tag{A.11}$$

The logarithm of the configurational integral gives βPV:

$$-\ln Z_{\mu VT} = -\beta PV \tag{A.12}$$

The Clausius-Clapeyron Equation

The slopes of coexistence curves in the temperature-pressure plnae are determined by the Clausius-Clapeyron equation. This remarkably elegant equation relates the slope of the coexistence curve to the differences in entropy, ΔS, and volume, ΔV between each phase, thus:

$$\frac{dP}{dT} = \frac{\Delta S}{\Delta V} \tag{A.13}$$

Since entropies are usually unevaluable, this equation is often written in the form:

$$\frac{dP}{dT} = \frac{\Delta H}{T \Delta V} \tag{A.14}$$

where ΔH is the difference in enthalpies between the phases.

Appendix B

Data Production and Analysis

This appendix expands upon the simulation methods used to collect the data presented in chapter 7, illustrating the steps taken in data production and analysis.

Solid State Simulation

LDTS-HDSS Coexistence (Lattice Switch Procedure)

Lattice Switch Monte Carlo simulations need to be performed at points close to coexistence, such that there is a high probability of crossing back and forth between phases within a simulation of reasonable length. At the very least, both phases must be local free energy minima at the simulation point. For our low temperature ($T^* < 0.2$) LDTS-HDSS coexistence simulations, we used our harmonic approximation results (see chapter 4) as initial estimates for coexistence. At higher temperatures, the harmonic approximation results began to deviate significantly from our simulation results, and no longer supplied effective estimates for coexistence. Histogram extrapolation from low temperature results was tried, but this method would only work over impractically small temperature increments due to the relatively rapid change with temperature of the equilibrium properties of the LDTS phase at coexistence. Instead, estimates for higher-temperature coexistence points were made by fitting the established coexistence line to a polynomial. In retrospect, use of Gibbs-Duhem integration combined with the LSMC approach (as described in reference [103]) should have been used.

Once an estimate to a coexistence point is made, the LSMC method requires measurement of

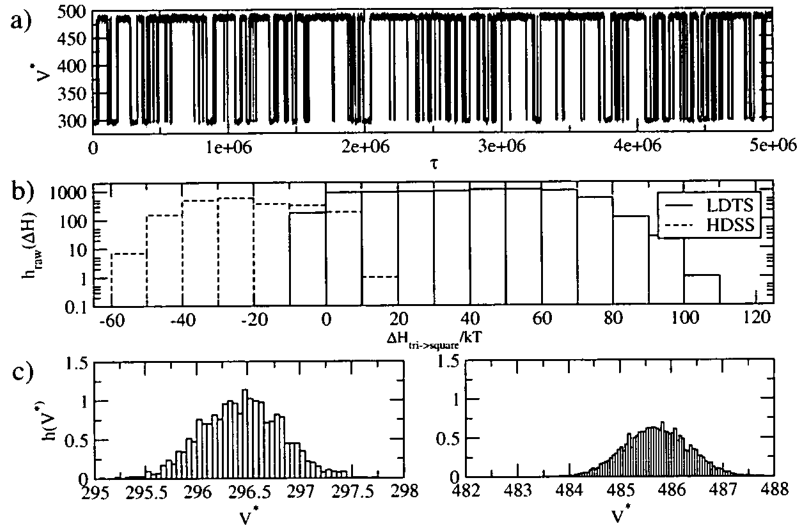

Figure B.1: Data collected for LDTS-HDSS coexistence at $T^* = 0.05$, $P^* = 0.25$, $N = 256$.
a) Raw weighted simulation data (V^* against Monte Carlo move number τ). The simulation can be seen to be regularly passing back and forth between two separate phases widely separated in volume. The simulation spends $\approx$ 21% of its time in the low volume (HDSS) phase and $\approx$ 79% of its time in the high volume (LDTS) phase. Histogram reweighting of this data gives coexistence (equal probability of observing each phase) at $T^* = 0.2507 \pm 0.00001$, showing the narrow temperature range over which appreciable coexistence can be measured.
b) Weighted histograms of overlap parameter collected from the simulation shown in figure B.1a. The unweighted ("true") histograms from this run can be seen in the top graph of figure 7.3. Comparison of these shows that multicanonical sampling has allowed relatively even sampling of both gateway states (ΔH around zero) and the configurations contributing significantly to the configurational integral.
c) (left) Unweighted ("true") volume histogram for the LDTS phase from the data presented in figure B.1a.
c) (right) Unweighted ("true") volume histogram for the HDSS phase from the data presented in figure B.1a.

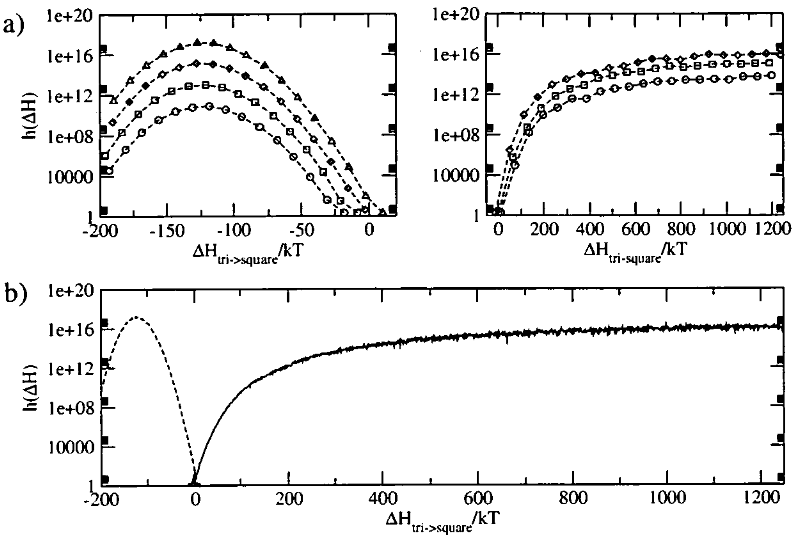

Figure B.2: Overlap parameter histograms collected for LDTS-HDSS coexistence at $T^* = 0.4$,$P^* = 0.63$,$N = 256$.
a) Illustration of iterative collection of multicanonical weights. The earliest estimate of weights is shown with open circles, followed by squares, then diamonds, then triangles. Note that not all iterations from the process are shown. The left-hand graph shows histograms for the overlap parameter from the HDSS phase; symbols are shown every tenth histogram bin. The right-hand graph shows histograms for the overlap parameter from the LDTS phase; symbols are shown every fiftieth histogram bin.
b) Combined estimated weights for $T^* = 0.4$; the histograms are normalised to ensure the values at $\Delta H = 0$ are equal.

"overlap parameter" histograms, used as multicanonical weights to increase the sampling rate of low probability "gateway" configurations [96, 97, 98, 103], from which lattice switch moves have appreciable acceptance probabilities. For our NPT simulations, this overlap parameter is ΔH as defined in equation 6.25. At very low temperature ($T^* < 0.1$), Boltzmann sampling of gateway (low ΔH) states was frequent enough that these histograms could be collected from a single LSMC-type run of $1E8$ Monte Carlo move attempts. However, at higher temperatures, it was found to be more effective to collect the histograms for each phase separately, through a series of iterative single-phase multicanonical simulations in each phase. The gathered histograms were then normalised with respect to each other by setting the values at $\Delta H = 0$ to be equal (which they must be by construction), then fed into an LSMC simulation as weights. The "true" coexistence temperature was then be estimated by performing histogram extrapolation to equal peak weight on the results from the LSMC simulation.

At high temperatures ($T^* > 0.3$), the ΔH histograms for the LDTS phase began to exhibit very long high overlap parameter tails. The full extent of these tails do not contribute significantly to the probability of observing the LDTS phase, but are observed with very much higher probability than the gateway states. Using "standard" multicanonical sampling, where the aim would be to observe ΔH values with equal probability, our simulations would have spent most of their time sampling these tails, producing data which would be of little value to us. As such, we imposed high-ΔH cutoffs, such that above these cutoffs ΔH values were sampled according their unweighted Boltzmann probabilities.

We illustrate the methods we have described in figures B.1 and B.2.

LDTS-HDSS Coexistence (Gibbs-Duhem Integration Procedure)

Once Lattice Switch Monte Carlo had become impractical (due to low sampling probabilities for gateway states and significant high-ΔH tails), we switched to the method of Gibbs-Duhem integration. This is a very simple and remarkably elegant procedure, as outlined in chapters 7 and 6. Our Gibbs-Duhem simulation results are tabulated in table B.1.

Liquid State Simulation (Two Dimensions)

Liquid State Anomalies

Simulations were carried out at points across the liquid state, as marked in figure 7.4 in chapter 7. Histogram extrapolation was then used to extrapolate the density and compressibility behaviour from the collected data along lines of constant chemical potential. These temperature dependences are shown in figures B.3 and B.4.

LDTS-Liquid Coexistence

Number density histograms from simulations performed at the compressibility maxima noted above show the clear bimodal signature of two-phase coexistence (see chapter 7). Simulations performed at these maxima are capable of crossing back and forth between the coexisting phases unaided, but to minimise error and avoid any possibility of hysteresis multicanonical reweighting has been performed. It has been found that a single simulation run of $1E8$ Monte Carlo move attempts has been enough to give weights allowing even sampling across both coexisting phases.

P	0.629	T	0.4	P	0.679	T_P	0.429
	<h>		<v>		<h>		<v>
HDSS	-4.82		1.174	HDSS	-4.73		1.176
LDTS	-4.36		1.82	LDTS	-5.42		1.80
Δh	0.45	Δv	0.65	Δh	0.69	Δv	0.63
P	0.679	T	0.424	P	0.729	T_P	0.449
	<h>		<v>		<h>		<v>
HDSS	-4.73		1.176	HDSS	-4.64		1.177
LDTS	-4.20		1.80	LDTS	-4.04		1.78
Δh	0.53	Δv	0.63	Δh	0.60	Δv	0.61
P	0.729	T	0.448	P	0.779	T_P	0.471
	<h>		<v>		<h>		<v>
HDSS	-4.64		1.177	HDSS	-4.55		1.179
LDTS	-4.05		1.79	LDTS	-3.88		1.76
Δh	0.60	Δv	0.61	Δh	0.67	Δv	0.58
P	0.779	T	0.469	P	0.829	T_P	0.490
	<h>		<v>		<h>		<v>
HDSS	-4.56		1.178	HDSS	-4.47		1.179
LDTS	-3.89		1.77	LDTS	-3.75		1.75
Δh	0.66	Δv	0.59	Δh	0.73	Δv	0.57
P	0.829	T	0.489	P	0.879	T_P	0.509
	<h>		<v>		<h>		<v>
HDSS	-4.47		1.180	HDSS	-4.38		1.181
LDTS	-3.75		1.75	LDTS	-3.61		1.73
Δh	0.72	Δv	0.57	Δh	0.79	Δv	0.54
P	0.879	T	0.508	P	0.929	T_P	0.525
	<h>		<v>		<h>		<v>
HDSS	-4.39		1.181	HDSS	-4.30		1.182
LDTS	-3.60		1.72	LDTS	-3.47		1.71
Δh	0.79	Δv	0.54	Δh	0.83	Δv	0.53
P	0.929	T	0.525	P	0.979	T_P	0.542
	<h>		<v>		<h>		<v>
HDSS	-4.31		1.182	HDSS	-4.22		1.183
LDTS	-3.48		1.71	LDTS	Melting Observed		
Δh	0.83	Δv	0.53				

Table B.1: Tabulated Gibbs-Duhem results. The left-hand column gives predictor-step results, the right hand column gives corrector-step results. Temperatures, pressures, volumes and enthalpies are all quoted in the appropriate reduced units.

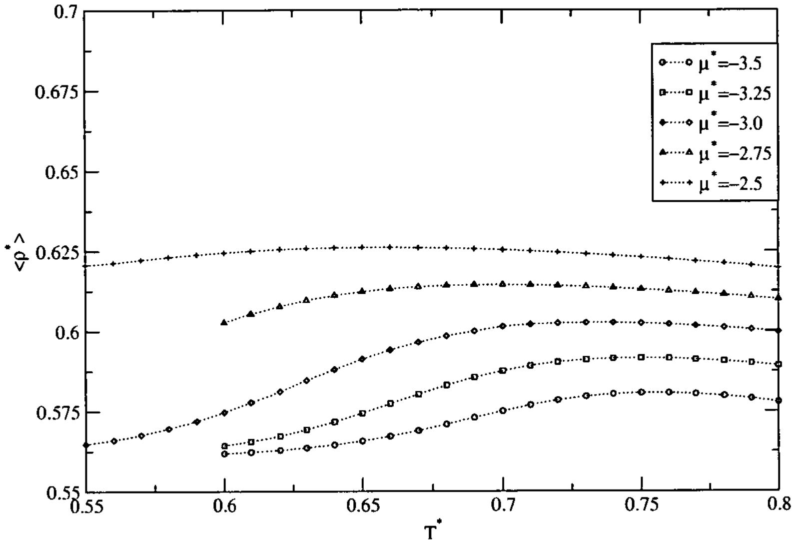

Figure B.3: Temperature dependence of density upon temperature at several chemical potentials, with $V^* = 100$. All curves show density maxima. The curves were obtained using histogram extrapolation, as described in the text.

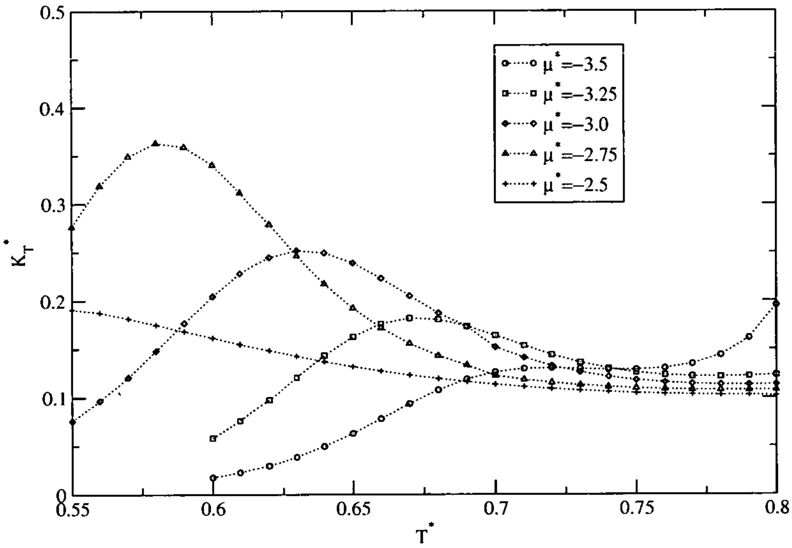

Figure B.4: Temperature dependence of compressibility upon temperature at several chemical potentials, with $V^* = 100$. All curves show both compressibility maxima and minima apart from the curve for $\mu^* = -2.5$, where the compressibility maximum is preempted by freezing to the HDSS phase.

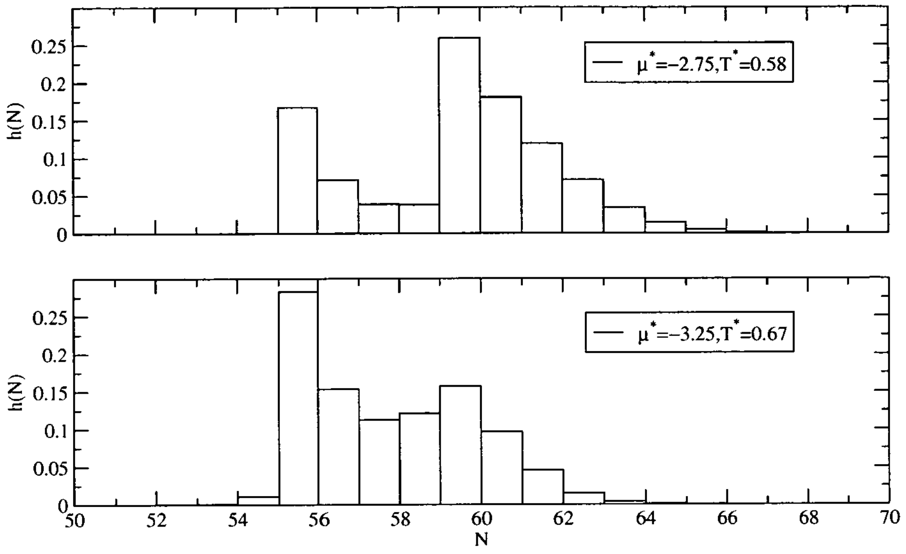

Figure B.5: Particle number histograms from simulations performed near LDTS-liquid coexistence (both with $V^* = 100$). At $\mu^* = -2.75$, the histogram is clearly bimodal, and the distributions for the two phases can be seen to be distinct. By $\mu^* = -3.25$, though the histogram remains bimodal, the density distributions for the two phases have considerable overlap, making estimation of coexistence problematic.

Establishing the exact coexistence line from the number density histograms has proven difficult, as the density distributions for the two phases have considerable overlap (see figure B.5); the LDTS-liquid coexistence line shown in figure 7.4 from chapter 7 is estimated from the position of the locus of compressibility maxima, as this gives lower error.

Bibliography

[1] Sadr-Lahijany, M.R., Scala, A., Buldyrev, S.V., Stanley, H.E., Phys. Rev. Lett. 81, 4895 (1998).

[2] Magee, J.E., Wilding, N.B., Mol. Phys. 100, 1641 (2002).

[3] Wilding, N.B., Magee, J.E., arXiv:cond-mat/020611 (submitted to Phys. Rev. E).

[4] Mandl, F., Statistical Physics (Wiley, Chichester, 1988).

[5] Yeomans, J.M., Statistical Mechanics of Phase Transitions (Clarendon, Oxford, 1992).

[6] Landau, L.D., Lifshitz, E.M., Statistical Physics, (Pergamon Press, Oxford 1980).

[7] Debenedetti, P.G., Metastable Liquids (Princeton University Press, Princeton 1996).

[8] Chaikin, P.M., Lubensky, T.C., Principles of Condensed Matter Physics (Cambridge University Press, Cambridge 1995).

[9] Ashcroft, N.W., Mermin, N.D., Solid State Physics (Saunders College Publishing, 1976).

[10] Peierls, R.E., Helv. Phys. Acta 7, 81 (1923).

[11] Mermin, N.D., Phys. Rev. 176, 250 (1968).

[12] Kosterlitz, J.M., Thouless, D.J., J. Phys. C: Solid State Phys., 6, 1181 (1973).

[13] Nelson, D.R., Halperin, B.I., Phys. Rev. B 19, 2457 (1979).

[14] Weber, H., Marx, D., Binder, K., Phys. Rev. E 51, 14636 (1995); Sengupta, S., Nielaba, P., Binder, K., Phys. Rev. E 61 6294 (2000); Jaster, A., Phys. Rev. E 59, 2594 (1999).

[15] Angell, C.A., in Water: A comprehensive treatise, Vol. 7, edited by F. Franks (Plenum Press, New York, 1972).

[16] Mishima, O., Stanley, H.E., Nature 396, 329 (1998).

[17] Rao, C.N.R., in Water: A comprehensive treatise, Vol. 1, edited by F. Franks (Plenum Press, New York, 1972).

[18] Stanley, H.E., Buldyrev, S.V., Canpolat, M., Meyer, M., Mishima, O., Sadr-Lahijany, M.R., Scale, A., Starr, F.W., Physica A. 257, 213 (1998).

[19] Speedy, R.J., J. Phys. Chem. 86, 982 (1982).

[20] Poole, P.H., Sciortino, F., Essman, U., Stanley, H.E., Nature 360, 324 (1992).

[21] Sastry, S., Debenedetti, P., Sciortino, F., Stanley, H.E., Phys. Rev. E 53, 6144 (1996).

[22] Stillinger, F.H., Rahman, A., J. Chem. Phys., 57, 1281, (1972).

[23] Smith, R.S, Kay, B.D., Nature 398, 788 (1999).

[24] Velikov, V., Borick, S., Angell, C.A., Science 294, 2335 (2001).

[25] Burton, E.F., Oliver, W.F., Proc. R. Soc. Lond. A. 153, 166 (1936).

[26] Johari, G.P., Hallbruker, A., Nature 330, 552 (1987).

[27] Mishima, O., J. Chem. Phys. 100, 5910 (1994).

[28] Johari, G.P., leissner, G., Hallbrukker, A., Mayer, E., J. Phys. Chem. 98, 4719 (1994).

[29] Bellisent-Funel, M.C., Bosio, L., J. Chem. Phys. 102, 3727 (1995).

[30] Pusztai, L., Phys. Rev. B. 61, 28 (2000).

[31] Johari, G.P., Phys. Chem. Chem. Phys., 2, 1567 (2000).

[32] Tonkov, E. Yu., High Pressure Phase Transformations - A Handbook, Vol. 1 (Gordon and Breach, Amsterdam 1992).

[33] Corbridge, D.E.C., Phosphorus: An Outline of its Chemistry, Biochemistry and Technology (Elsevier, New York, 1978).

[34] Hohl, D., Jones, R.O., Phys. Rev. B 50, 17 047 (1994).

[35] Katayama, Y., Mizutani, T., Utsumi, W., Shimomura, O., Yamakata, M., Funakoshi, K., Nature 403, 17-0 (2000).

[36] Togaya, M., Phys. Rev. Lett 79, 2472 (1997).

[37] Glosli, J.N., Ree, F.H., Phys. Rev. Lett. 82, 4659 (1999).

[38] Eliashberg, G., Capellmann, H., JetP Lett. 67, 125 (1998).

[39] van der Eb, J.W., Kuz'menko, A.B., van der Marel, D., Phys. Rev. Lett. 86, 3407 (2001).

[40] Nikolaev A.V., Michel K.H., Eur. Phys. J. B. 9 619 (1999).

[41] McMahon, M.I., Nelmes,R.J., Rekhi, S., Phys. Rev. Lett. 87, 25502 (2001).

[42] Christensen, N.E., Boers, D.J., van Velsen, J.L., Nokikov, D.L., Phys. Rev. B. 61, R3764 (2000).

[43] Hemmer, P.C., Stell, G., Phys. Rev. Lett. 24, 1284 (1970).

[44] Widom, B., Rowlinson, J.S., J. Chem. Phys. 52, 1670 (1970)

[45] Stell, G., Hemmer, P.C., J. Chem. Phys. 56, 4274 (1972).

[46] Takahashi, H., Proc. Phys. Math. Soc. Jpn. 24, 60 (1942) in *Mathematical Physics in One Dimension,* edited by Lieb, E.H., Mattis, D.C. (Academic, New York, 1966).

[47] Lebowitz, J.L., Penrose, O., J. Math. Phys. 43, 3098 (1965).

[48] Kincaid, J.M., Stell, G., Hall, C.K. J. Chem. Phys. 65, 2161 (1976).

[49] Kincaid, J.M., Stell, G., Goldmark, E., J. Chem. Phys. 65, 2172 (1976).

[50] Young, D.A., J. Chem. Phys. 58, 1647 (1973).

[51] Jagla, E.A., Phys. Rev. E. 58, 1478 (1998).

[52] Bladon, P., Frenkel, D., Phys. Rev. Lett. 74, 2519 (1995).

[53] Chou, T., Nelson, D.R., Phys. Rev. E. 53, 2560 (1996).

[54] Bolhuis, P., Frenkel, D., Phys. Rev. Lett. 72, 2211 (1994).

[55] Bolhuis, P., Hagen, M., Frenkel, D., Phys. Rev. E 50, 4880 (1994).

[56] Bolhuis, P., Frenkel, D., J. Phys.: Condens. Matter 9, 381 (1997).

[57] Rascon, C., Velasco, E., Mederos, L., Navascues, G, J. Chem. Phys. 106, 6689 (1997).

[58] Jagla, E.A., J. Chem. Phys. 110, 451 (1999).

[59] Velasco, E., Mederos, L., Navascues, G., Hemmer, P.C., Stell, G., Phys. Rev. Lett. 85, 122 (2000).

[60] Ackland, G.J., Reed, S.K., arXiv:cond-mat/0218189, submitted to Phys. Rev. B.

[61] Scala A., Sadr-Lahijany, M.R., Giovambattista, N., Buldyrev, S.V., Stanley, H.E., J. Stat. Phys. 100, 97 (1999).

[62] Scala A., Sadr-Lahijany, M.R., Giovambattista, N., Buldyrev, S.V., Stanley, H.E., Phys. Rev. E 63, 041202 (2001).

[63] Malescio, G., Pellicane, G., Phys. Rev. E. 63, 020501 (2001).

[64] Franzese, G., Malescio, G., Skibinsky, A., Buldyrev, S.V., Stanley, H.E., Nature 409, 692 (2001).

[65] Franzese, G., Malescio, G., Skibinsky, A., Buldyrev, S.V., Stanley, H.E., J. Phys.: Cond. Matt. 14, 2193 (2002).

[66] Jagla, E.A., Phys. Rev. E 63, 061501 (2001).

[67] Gursey, F., Proc. Cambridge Phil. Soc. 46, 182 (1950).

[68] Tonks, L., Physics Review 50, 955 (1936).

[69] Lieb, E.H., Mattis, D.C., Mathematical Physics in One Dimension (Academic, New York, 1966).

[70] Horton, G.K., Maradudin, A.A., Dynamical Properties of Solids Volume 1 (North-Holland Publishing Company, Amsterdam, 1974).

[71] Allen, M.P., Tildesley, D.J., Computer Simulation of Liquids (Clarendon Press, Oxford 1987).

[72] Hoover, W.G., J. Chem. Phys. 49, 1981-1982 (1968); Polson, J.M., Trizac, E., Pronk, S., Frenkel, D., J. Chem. Phys. 112, 5339-5342 (2000).

[73] Press, W.H., Teukolsky, S.A., Vetterling, W.T., Flannery, B.P., Numerical Recipes in C, Second Edition (Cambridge University Press, Cambridge 1992).

[74] Lennard-Jones, J.E., Devonshire, A.F., Proc. Roy. Soc. London A 163, 53 (1937); ibid 165, 1 (1938).

[75] Hill, T.L., Statistical Mechanics - Principles and Selected Applications (McGraw-Hill, New York 1956), Chap. 8.

[76] Kirkwood, J.G., J. Chem. Phys. 18, 380 (1950).

[77] Barker, J.A., Lattice Theories of the Liquid State, Pergamon Press (1963).

[78] Burshtein, A.I, Introduction to Thermodynamics and Kinetic Theory of Matter, (Wiley, New York 1966).

[79] Modarress, H., Ahmadnia, E., Mansoori, G.A., J. Chem. Phys. 111, 10236 (1999); Pourgheysar, P., Mansoori, G.A., Mansoori, H., Ahmadnia, E., J. Chem. Phys. 105, 9580 (1996).

[80] Potoff, J.J., Panagiotopoulos, A.Z., J. Chem. Phys. 109 10914 (1998), and references therein.

[81] Lennard-Jones, J.E., Devonshire, A.F., Proc. Roy. Soc. London A169, 317 (1939).

[82] Wentorf, W.H., Buehler, R.H., Hirschfelder, J.O., Curtiss, C.F.; J. Chem. Phys. 18, 1484 (1950).

[83] Buehler, R.J., Wentorf, R.H., Hirschfelder, J.O., Curtiss, C.F., J. Chem. Phys 19, 61 (1951).

[84] Frenkel, D., Smit, B., Understanding molecular simulation, (Academic Press, London, 1996).

[85] Kaminsky, R.D., J. Chem. Phys. 101, 4986 (1994).

[86] Gubbins, K.E., Shing, K.S., Streett, W.B., J. Phys. Chem. 87, 4573 (1983).

[87] Ferrenberg, A.M., Swendsen, R.H., Phys. Rev. Lett. 61, 2635 (1998).

[88] Ferrenberg, A.M., Swendsen, R.H., Phys. Rev. Lett. 63, 1195 (1989).

[89] Deutsch, H.P., J. Stat. Phys. 67, 1039 (1992).

[90] Panagiotopoulos, A.Z., Mol. Phys. 61, 813 (1987).

[91] Berg, B.A., Neuhaus, T., Phys. Rev. Lett. 68, 9 (1992).

[92] Smith, G.R., Bruce, A.D., J. Phys. A 28, 6623 (1995).

[93] Wilding, N.B., Phys. Rev. E 52, 602 (1995).

[94] Panagiotopoulos, A.A., J. Phys. Cond. Matt. 12, R25 (2000).

[95] Wilding, N.B., Am. J. Phys. 69, 1147 (2001).

[96] Bruce, A.D., Wilding, N.B., Ackland, G.J., Phys. Rev. Lett. 79, 3002 (1997).

[97] Bruce, A.D., Jackson, A.N., Ackland, G.J., Wilding, N.B., Phys. Rev. E 61, 906 (2000).

[98] Jackson, A.N., Bruce, A.D., Ackland, G.J., Phys. Rev. E. 65, 036710 (2002).

[99] Wilding, N.B., Bruce, A.D., Phys. Rev. Lett. 85, 5138 (2000).

[100] Wilding, N.B., Comp. Phys. Comm. 146, 99 (2002).

[101] Acharya, A., Bruce, A.D., Ackland, G.A., unpublished.

[102] Kofke, D.A., Mol. Phys. 78, 1331 (1993).

[103] Andrew N. Jackson, Ph.D. Thesis, Edinburgh University, 2001.